FLORIDA INTERNATIONAL UNIVERSITY

Miami, Florida

WIND-INDUCED DYNAMIC BEHAVIOR OF BUILDING ENVELOPES: A NUMERICAL STUDY ON GLASS CURTAINWALLS AND OPERABLE WINDOW SYSTEMS

A dissertation submitted in partial fulfillment of

the requirements for the degree of

DOCTOR OF PHILOSOPHY

in

CIVIL ENGINEERING

by

Ali Bakhtiari

2023

To: Dean John L. Volakis
College of Engineering and Computing

This dissertation, written by Ali Bakhtiari, and entitled Wind-induced Dynamic Behavior of Building Envelopes: A Numerical Study on Glass Curtainwalls and Operable Window Systems, having been approved in respect to style and intellectual content, is referred to you for judgment.

We have read this dissertation and recommend that it be approved.

_____
Arindam Gan Chowdhury

_____
Amal Elawady

_____
Ioannis Zisis

_____
Nipesh Pradhananga

_____
Seung Jae Lee, Major Professor

Date of Defense: June 28, 2023

The dissertation of Ali Bakhtiari is approved.

_____
Dean John L. Volakis
College of Engineering and Computing

_____
Andrés G. Gil
Vice President for Research and Economic Development
and Dean of the University Graduate School

Florida International University, 2023

DEDICATION

This dissertation manuscript is dedicated to my dear parents for their immense love and support. To my brother, my grandma, and my aunt, who were always there for me. To my beloved uncle Hassan who passed away during my Ph.D. journey. To my love, Mina, my entire family, and all my friends in Iran and USA thank you for always being there for me. And finally, to the brave women and men of my country who fight for their freedom.

ACKNOWLEDGMENTS

I would like to extend my heartfelt appreciation to Dr. Seung Jae Lee, my major professor, for his unwavering support, encouragement, and guidance throughout my doctoral studies.

I would also like to thank my committee members Dr. Arindam Gan Chowdhury, Dr. Amal Elawady, Dr. Ioannis Zisis, and Dr. Nipesh Pradhananga for their support and valuable input in this dissertation work.

I would like to express my special thanks to Dr. Guido Lori for his invaluable support and contribution to this research. This research could not find its way without Dr. Lori's deep knowledge of building envelopes, his guidance, and his incredible vision. I am grateful to my colleagues during this research, Dr. Krishna Sai Vutukuru, and Kehinde Alawode. I would also like to thank Dr. Armin Mehrabi, the graduate program director of the Department of Civil and Environmental Engineering at FIU.

I am thankful to the University Graduate School at FIU for granting me the Doctoral Evidence Acquisition Fellowship, and the Dissertation Year Fellowship, which has provided invaluable support during the writing phase of my dissertation. I am also thankful to the funding agencies of this research, the National Science Foundation under Grant No. IIP 1841503 and the I/UCRC Wind Hazard and Infrastructure Performance (WHIP) #2019-04 and #2020-04, and Florida Sea Grant, Project #: R/C-D-24. During my Ph.D. program, I was also financially supported by Accelerated Bridge Construction – University Transportation Center under project #: ABC-UTC-2013-C3-FIU05, and NSF CMMI under project #1635378, which is greatly appreciated. The experiments in this project were conducted at the NHERI Wall of Wind Experimental Facility (National Science

Foundation Award No. 1520853 and No. 2037899). I also would like to thank the WHIP Industrial Advisory Board members for their comments and feedback. I would like to thank the Permasteelisa group for providing the curtainwall sample and installation work. I am also grateful to MIDAS IT Co., Ltd. for providing the academic license of MIDAS Gen finite element analysis software.

ABSTRACT OF THE DISSERTATION

WIND-INDUCED DYNAMIC BEHAVIOR OF BUILDING ENVELOPES: A NUMERICAL STUDY ON GLASS CURTAINWALLS AND OPERABLE WINDOW SYSTEMS

by

Ali Bakhtiari

Florida International University, 2023

Miami, Florida

Professor Seung Jae Lee, Major Professor

The inadequate performance of building envelopes contributes significantly to financial losses in coastal regions of the United States caused by hurricanes. Glass curtainwalls, commonly used as building envelopes, are highly vulnerable to extreme wind loads and susceptible to failures due to excessive vibrations during windstorms. These failures are primarily attributed to wind-induced vibrations resulting from strong gusts, leading to damage. Such curtainwall failures can compromise the water tightness of building envelope systems, allowing water infiltration during storms and rendering the building unusable, even if the main wind-resisting system remains structurally intact. The ASCE 7 standard requires dynamic analysis to assess the impact of wind on structures but does not mandate the analysis of structures with natural frequencies exceeding 1 Hz for wind-induced dynamic effects.

This study aims to address knowledge gaps related to the effects of wind-induced vibrations on the dynamic behavior of single-skin façade, double-skin façade curtainwalls, and operable window systems. Comprehensive finite element analyses are conducted to simulate the dynamic response of the curtainwall systems. Experimental data from full-scale wind tunnel tests on single-skin and double-skin façade curtainwall specimens at the NHERI Wall of Wind Experimental Facility are used to validate the results.

The findings highlight the significant influence of the supporting structure on the wind-induced dynamic behavior of the façade, emphasizing the importance of considering the interaction between the building structure and the façade. Prominent responses are observed at frequencies above 4 Hz, indicating that curtainwall window systems, currently exempt from vibration analysis as per the ASCE 7 Standard, may be prone to damage or failure due to wind-induced vibrations. Vertical protrusions attached to the façade are found to amplify wind-induced vibrations in the curtainwall's glazing unit, posing additional risks. The study reveals that operable window systems and their connections are vulnerable to potential failure due to wind-induced vibrations, particularly in open condition.

Moreover, defects causing increased cavity permeability in double-skin façade curtainwalls result in higher vibration levels, with greater impact observed in the internal glazing. These consequences are exacerbated in higher wind speeds, increasing the likelihood of water infiltration in vented-cavity double-skin facade systems compared to closed-cavity configurations.

TABLE OF CONTENTS

LIST OF TABLES

TABLE PAGE

LIST OF FIGURES

FIGURE PAGE

CHAPTER 1 . INTRODUCTION

The building envelope refers to the physical boundary or shell of a building that separates the interior environment from the exterior environment. It is comprised of various components that work together to provide thermal insulation, weather resistance, structural support, and other essential functions for the building. The building envelope acts as a barrier against the elements, controlling the transfer of heat, air, and moisture between the interior and exterior spaces, and plays a crucial role in energy efficiency, occupant comfort, and overall building performance. Effective management of energy consumption and reduction of environmental impact in buildings, especially in tall and expansive structures such as skyscrapers that have higher overall energy demands, primarily rely on the performance of the building envelope (Oh, 2020). Glass curtainwalls are widely used as the primary building envelope in modern construction, representing the predominant choice for enclosing buildings in the contemporary built environment (Behr, 1998; Caterino et al., 2017; Lu et al., 2018; Pariafsai, 2016; Qu et al., 2014). Glazed curtainwalls offer a combination of aesthetic, functional, and sustainable benefits, making them an important component of modern architecture. Installed onto the building's structure, these elements serve as protective layers that safeguard against diverse environmental elements such as wind forces, water infiltration, solar radiation, and external noise pollution. Simultaneously, they enhance the visual appeal and aesthetics of the building.

The United States has experienced several devastating hurricanes in recent decades, with the total cost of damage from these storms reaching hundreds of billions of dollars. In the year 2017 alone, losses surpassed 306 billion dollars while the estimated cost of Hurricane

Harvey alone amounted to 125 billion dollars. Hurricane Katrina (2005) was the costliest hurricane in US history, with total losses of $233 billion (NOAA, 2021). According to FEMA (2006), the majority of wind damage occurred due to the failure of building envelopes and rooftop equipment. Damage to building envelopes was observed over a wide area, extending from the New Orleans area in the west to Dauphin Island, Alabama in the east, covering a distance of approximately 140 miles from east to west. While many buildings suffered minimal or no structural damage, their overall loss is significant due to water infiltration caused by the failure of the building envelopes. A substantial portion of this damage occurred in locations where wind speeds were below the current design levels for buildings. There was a notable lack of glazing protection measures, leading to substantial damage to building glazing. Another important aspect of poor building envelope performance is the secondary damage that can occur as a result of envelope failures. Even small breaches in the envelopes, if left open for several weeks, can allow a significant amount of water to seep into buildings, causing damage to their contents and promoting the growth of mold (FEMA, 2006).

Despite recent advancements in the main wind force resisting systems (MWFRS), the building envelopes continue to be the most susceptible component during extreme wind events, and inadequate performance of building envelopes has largely contributed to the billions of dollars in hurricane-related annual losses in the coastal areas of the United States (National Science Board, 2007; NCEI, 2022). Glass curtainwalls are highly susceptible to frequent damage during extreme wind events. Therefore, it is crucial to prioritize resilient and safe design and installation of these curtainwalls, particularly in coastal regions of the United States where hurricanes are a prevalent concern. The damage can be exacerbated

by the resonance effect, where the small eddies produced by shear in the atmospheric boundary layer (ABL) amplify the vibratory movements of the building envelope when the excitation frequencies align with the natural frequencies of the envelope (Abdelaziz et al., 2021a; Momtaz et al., 2017; Vutukuru, 2021). Any progressive failure of the building envelope can cause internal pressurization which can potentially lead to structural failure in extreme wind-loading scenarios (Pan et al., 2013). The failure of the envelope is also a prominent source of wind-borne debris, which is a serious threat to the building envelope of the surrounding buildings and infrastructure (Grayson et al., 2012; Jain, 2015; Michael Grayson et al., 2013; Minor, 1994).

The failure of curtainwall systems is assumedly attributed to wind-induced vibrations (WIVs) caused by extreme wind gusts, leading to consequential damage to their structural integrity and components. Wind-induced vibrations (WIV) result in various failures in curtainwalls, including pull-out, cracking, gasket dislodging, etc. (Sanders & Hargrove, 2012). These failures, related to WIV, can have a detrimental effect on the water tightness of envelope systems, enabling water infiltration during storm events (FEMA 488, 2005). In addition, the majority of high-rise building projects incorporate operable windows within unitized curtainwall panels. As openings within the facade envelope, they serve as the weakest points and are highly prone to wind-induced vibrations during normal service conditions. As a result, operable windows often experience failures due to damage to their frames and connections.

Although ASCE 7 (2016) mandates dynamic analysis to assess the impact of wind on structures, it does not require structures with natural frequencies exceeding 1 Hz to be

analyzed for wind-induced dynamic effects. However, recent wind-tunnel studies have evidenced that building envelopes (with a natural frequency higher than 1 Hz) are subjected to a significant resonant vibration. For example, wind tunnel tests conducted on roof-mounted photovoltaic systems showed major resonant responses at around 14 Hz (Estephan et al., 2022; Moravej et al., 2015). Habte et al. (2015) and Azzi et al. (2020) also showed major wind-induced resonant vibrations of standing seam metal roofs in a range of frequencies between 8 Hz and 14 Hz. Hence, the ASCE 7 criterion can be misleading as it was primarily developed to address vibrations of the entire building and may not be applicable to building envelope components with higher frequencies than 1 Hz. Consequently, there is a misconception that curtainwall window systems and operable window systems are not susceptible to wind-induced dynamic effects, leaving the overall building envelope still vulnerable to wind actions.

Furthermore, the current procedures outlined in established standards like ASTM E330/E330M (2014) and ASTM E1886 (2013) for assessing wind-induced stresses are restricted to static uniform or cyclic pressure conditions. It was also observed that the uniform pressure static tests such as ASTM E1592 (2017) are limited in capturing the wind-induced vibrations of the roofs observed in the dynamic tests. However, these simplified methods used in many of the previous experimental studies fail to account for the dynamic effects caused by random wind loading, as well as the spatial and temporal variations resulting from turbulence. As a result, they are unable to realistically capture wind-induced vibrations in curtainwall windows and operable components. In addition, there is a limited availability of numerical studies focusing on the wind-induced behavior of curtainwall systems. Previous research has predominantly concentrated on the seismic and blast-

induced behavior of facades, rather than specifically addressing wind-related effects. The motivation behind this study stems from the absence of comprehensive integrated investigations, combining full-scale experimental and numerical analyses, to gain a fundamental understanding of the impact of wind-induced vibrations (WIV) on the dynamic behavior of curtainwall systems. The objective of this study is to develop highly accurate finite element (FE) models of single-skin and double-skin façade curtainwall systems. The finite element (FE) modeling approach also encompasses the integration of an operable window system within the single-skin façade curtainwall system. The numerical models undergo calibration and validation through a comparison with experimental data gathered from full-scale wind tunnel tests. The Wall of Wind Experimental Facility (WOW EF) located at Florida International University is utilized to generate full-scale wind tunnel test data. Following this, the developed finite element (FE) models will be utilized to assess the dynamic response of the façade when subjected to diverse wind loadings, including varying wind speeds and directions. Furthermore, the investigation includes modeling the entire structure, encompassing both the curtainwall system and its supporting structure. By employing suitable system identification methods, the study aims to examine the impact of façade-structure interaction on the dynamic performance of the façade.

The subsequent chapters of this dissertation are structured as follows:

Chapter 2 is dedicated to studying the wind-induced vibratory response of a single-skin façade curtainwall system. A high-fidelity FE model of the single-skin curtainwall is calibrated and validated by comparing it with experimental data acquired from full-scale

wind tunnel tests for different dynamic wind loading scenarios. Two distinct approaches are employed in finite element (FE) modeling to investigate the influence of façade-structure interaction on the dynamic behavior of the façade. The first approach involves modeling the entire test structure, including both the curtainwall and the supporting steel structure to which it is attached. The second approach focuses on modeling the curtainwall as an independent system, excluding the supporting structure. A system identification method is utilized to support the analysis. Additionally, the impact of vertical protrusions on the dynamic response of the façade curtainwall is examined.

Chapter 3 delves into the influence of wind-induced vibrations on the dynamic response of the operable window system. A meticulously calibrated and validated finite element modeling and analysis approach is then employed to evaluate the dynamic behavior of the operable window system in response to wind-induced vibrations, considering both closed and open service conditions of the window.

Chapter 4 entails an investigation into the wind-induced dynamic behavior of a closed-cavity double-skin curtainwall system. A finite element model is created and subsequently calibrated and validated using wind-tunnel test data obtained from a full-scale closed-cavity double-skin curtainwall.

Chapter 5 provides a summary of the key findings and contributions of this study, along with a description of its limitations. Additionally, it suggests potential avenues for future research.

The wind-tunnel tests described in this dissertation were performed by Kehinde Alawode and Krishna Sai Vutukuru, whose valuable contributions to this research are highly

acknowledged. The relevant publications associated with their work are referenced throughout this manuscript.

CHAPTER 2 . NUMERICAL STUDY ON WIND-INDUCED DYNAMIC RESPONSE OF SINGLE-SKIN FAÇADE CURTAINWALL SYSTEM

2.1 Introduction

Most numerical and experimental studies on the dynamic behavior of single-skin façade curtainwall systems have focused on seismic and blast performance. Studies conducted by Gorenc and Beg (2016), Bedon and Amadio (2018), Galli (2012), Casagrande et al. (2017), Aiello et al. (2018), and Memari et al. (2021) have applied finite element modeling and analysis to investigate the vibration of the curtainwall façade systems subjected to seismic loading. On the other hand, a limited number of studies were conducted to understand the WIV effects on the dynamic response of the curtainwall systems. Rizzo et al. (2021) investigated the structural response of a curtainwall system (5.45 x 7.06 m) through two sets of full-scale wind tunnel tests. In the first set of wind tunnel tests, the whole curtainwall was subjected to a uniformly distributed pressure generated by air jets. The second set of experimental tests was performed on the insulated glass panel without frame to assess the mechanical performance of the glass panel. A finite element (FE) model was developed and calibrated using experimental data. The calibrated FE model was then used to predict the deformation of the façade in various scenarios estimated from the wind tunnel test data of buildings with different geometries. They concluded that the uniformly distributed pressure tests have limitations in accurately estimating the façade performance subjected to wind load, suggesting the necessity of a full-scale wind tunnel test. Nakagami (2003) conducted a FE analysis to investigate the vibration of the glass façade under wind load with a peak wind velocity of 30 m/s. The effect of boundary conditions was studied for

which two boundary types were considered including linear supports along the 4 edges, and point supports at the 4 corners. Resonant responses beyond 10 Hz were observed for the glass façade with linear supports along the 4 edges, while the point supports at the corners led to resonant responses lower than 10 Hz. It was shown that the response was affected by the boundary condition, and glass plate dimensions. However, only the glass panes were modeled in this study without the framing profiles, which is a major limitation. Mazzucchelli et al. (2017) showcased a FE modeling approach for analyzing the dynamic behavior of the façade subjected to wind and seismic loads to evaluate structural aspects and dynamic response of the cladding based on a combination of numerical modeling and laboratory tests to validate the FE model. Only the FE model of the curtainwall was developed, while the authors mentioned the importance of the inevitable interaction effects of the load-bearing structure on the mechanical behavior of the façade. Utilizing equivalent springs with relevant stiffness values was recommended by the authors to model the structure-curtainwall connections.

This chapter of the study is motivated by the lack of integrated numerical and full-scale experimental studies to fundamentally understand the effects of wind-induced vibrations (WIV) on the dynamic behavior of single-skin curtainwall systems. This study aims to develop a high-fidelity FE single-skin façade curtainwall model and calibrate and validate it in comparison with the experimental data obtained from full-scale wind tunnel tests. The developed FE model will be then used to predict the dynamic response of the façade subjected to various wind loadings, i.e., different wind speeds and directions. The Wall of Wind Experimental Facility (WOW EF) at Florida International University (FIU) is used to create the full-scale wind tunnel test data. Two different approaches are made for the FE

modeling to study the effect of façade-structure interaction on the façade's dynamic behavior by (1) modeling the whole test structure including the curtainwall as well as the supporting steel structure to which the curtainwall is mounted, and (2) modeling the curtainwall as an isolated system without the supporting structure. A system identification method is used to underpin the observation. The effect of vertical protrusions on the dynamic response of the façade curtainwall is also studied.

2.2 Wind tunnel test

2.2.1 Specimen Configuration

The full-scale wind tunnel tests are conducted at the Wall of Wind (WOW) Experimental Facility (EF), Florida International University (FIU). This is one of eight Natural Hazards Engineering Research Infrastructure (NHERI) EFs supported by the US National Science Foundation (NSF). The WOW EF is full-scale wind tunnel testing comprised of 2×6 arrays of 12 fans that can replicate Category 5 hurricane winds and has a full-scale wind tunnel testing capability (Chowdhury et al., 2017). A turntable is located in front of the flow management box and enables to test of all wind directions on a test specimen (Figure 2.1). Below summarizes the wind tunnel tests, and further details are discussed in Alawode et al (2023).

Figure 2.2a shows the configuration of the single-skin façade curtainwall specimen, which comprises 3 panels. The center panel includes an operable window. The single-skin façade curtainwall is mounted to a supporting steel structure that is bolted to the turntable underneath. The specimen includes a roof on top, with an overhang of 0.41 m, and the adjoining sides are closed with wooden sidewalls as shown in Figure 2.2b. Instrumentation

of pressure taps requires drilling into glass panels which are infeasible, and therefore, the polycarbonate panels with the same dimensions as the façade panels, are mounted to capture the pressure data on the other side of the specimen. A wooden frame is mounted on the supporting steel structure, and three polycarbonate panels are installed on the wooden frame (Figure 2.2b).

The effect of vertical protrusions (also known as fins) on the dynamic behavior of the single-skin façade curtainwall is also investigated in the test. Two V-shape aluminum fins are installed on the mullions between the panels (Figure 2.3a). Likewise, two analog wooden fins are designed and mounted to the polycarbonate side (Figure 2.3b).

Figure 2.4a and b show the overall configuration of the specimen schematically. The overall dimensions of the single-skin façade curtainwall mounted on the front side of the specimen are 3.05 m in height × 3.65 m in width (10 ft × 12 ft). The operable window in the center panel is 1.87 m in height × 0.6 m in width (6.13 ft × 1.96 ft). The supporting steel structure (to which the curtainwall is mounted) has rectangular dimensions of 3.05 m in height × 2.76 m in width × 1.8 m in depth (10 ft × 9 ft × 5.90 ft). The curtainwall includes 5 vertical joints as shown in Figure 2.4a and b. An enlarged image of Joint 2's cross-section is shown in Figure 2.4c to show the anatomy of the connection, where a mullion (vertical framing element of a curtainwall system) is attached to the glass unit using structural silicone.

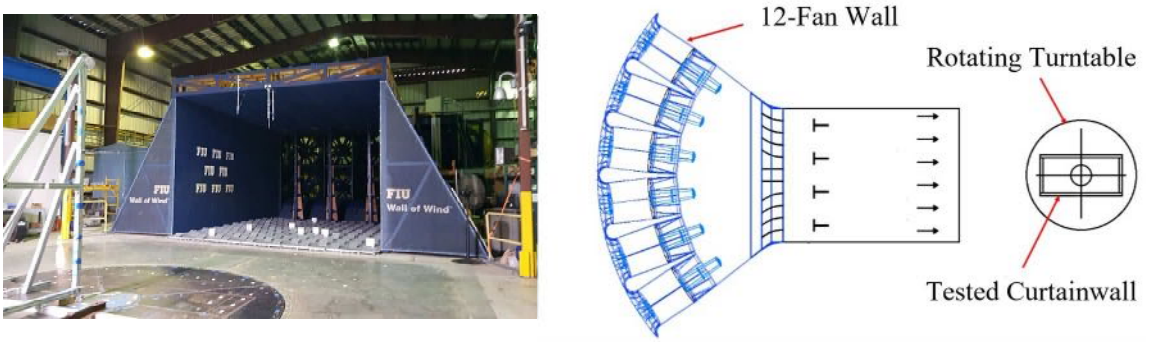

(a) (b)

Figure 2.1. FIU Wall of Wind (WOW) Experimental Facility (EF): (a) Interior of the WOW EF; (b) Plan view of the WOW EF

(a) (b)

Figure 2.2. Tested single-skin façade curtainwall with two different sides: (a) Curtainwall panels; (b) Polycarbonate panels mounted on the wooden frame.

Figure 2.3. Single-skin curtainwall with vertical protrusions: (a) Curtainwall panels; (b) Polycarbonate panels

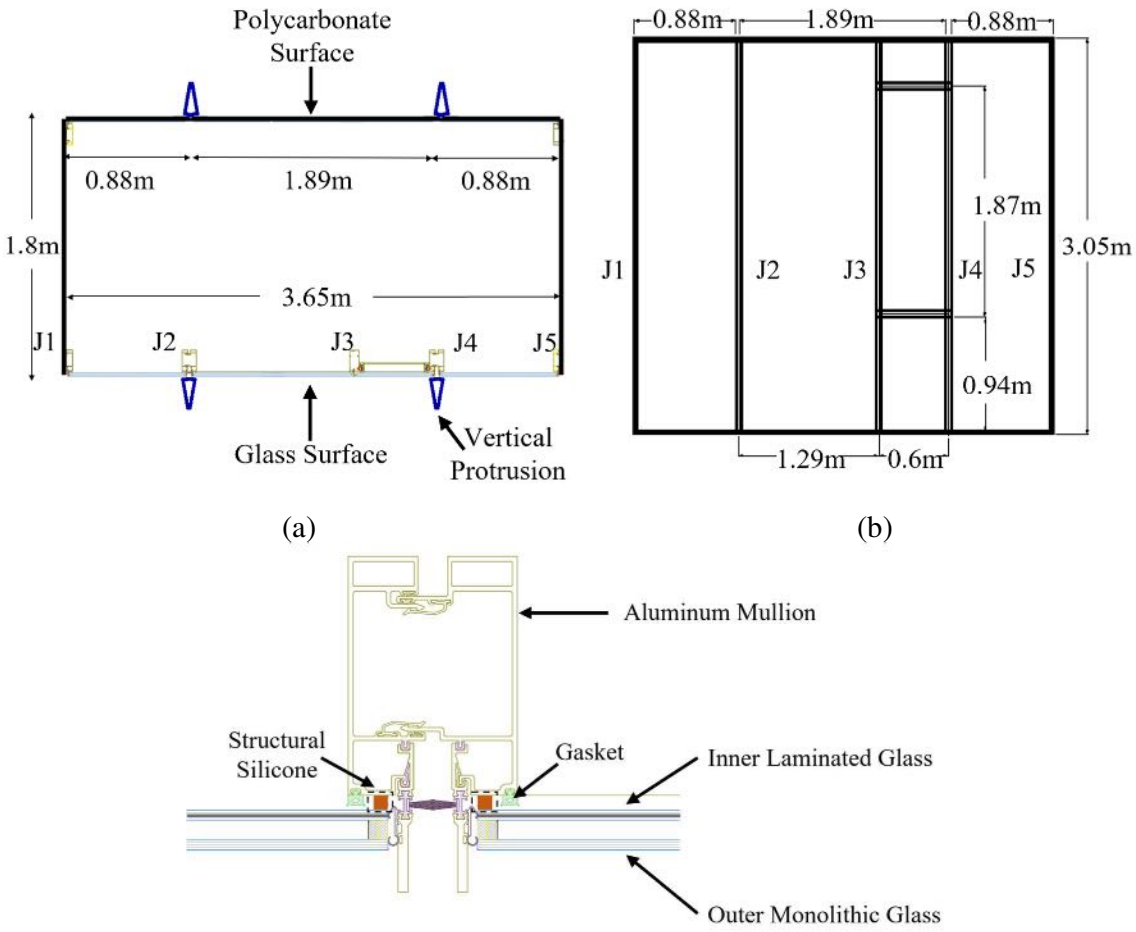

Figure 2.4. The overall dimension of the tested single skin curtainwall, where J# refers to a vertical joint number: (a) Plan view (shown with vertical protrusions); (b) Elevation view; (c) Cross-section of Joint

2.2.2 Sensor instrumentation and test protocol

A total number of 110 pressure taps are instrumented on the polycarbonate panels as shown in Figure 2.5. Additional 16 taps are instrumented on the vertical protrusions. A total of 12 strain gauges are instrumented behind the mullions, while 5 accelerometers are placed on the glass as shown in Figure 2.6. Pressure data is obtained from the polycarbonate panels, while acceleration and strain data are obtained from the actual curtainwall glazing panels. Table 2.1 summarizes the testing protocol and test duration of all wind tunnel tests.

The sampling frequency for pressure measurements is 512 Hz. Pressure data is obtained at the wind speed of 22.35 m/s and wind direction is varied from 0° (normal direction to the panels) to 180° by rotating the turntable in 15° increments (Figure 2.7). The collected pressure data is post-processed by applying a tubing transfer function to correct the data for the distortion caused by tubing length (Irwin et al., 1979). The acceleration and strain data are obtained at wind speeds of 22.35 m/s, 31.30 m/s, and 40.23 m/s with a sampling frequency of 500 Hz. Wind directions vary from 0° to 315° in 45° increments. The test duration is 10 minutes for 22.35 m/s, and 5 minutes for 31.30 m/s and 40.23 m/s, respectively. The shorter test duration (5 min.) is considered for the higher wind speeds because it would be difficult to test the curtainwall specimen further if it undergoes permanent deformation.

The mean wind speed at the reference height, i.e., the roof height (3.2 m) is considered as 21.97 m/s (for 22.35 m/s wind), while a roughness length z_0 of 0.08 m is used to simulate an open terrain atmospheric boundary layer for the full-scale wind tunnel tests. The wind speed and turbulence characteristics are measured at the center of the turntable using Cobra probes instruments.

The data acquisition in the experiment is not performed simultaneously with a 180° difference. For example, pressure data at the normal wind direction (i.e., 0°) is obtained at the polycarbonate panels. On the other hand, the acceleration and strain data for the same normal direction is obtained at 180° from the actual curtainwall glazing panels (Figure 2.7). In numerical modeling to be discussed in the following sections, the normal wind direction will be simply referred to as 0°.

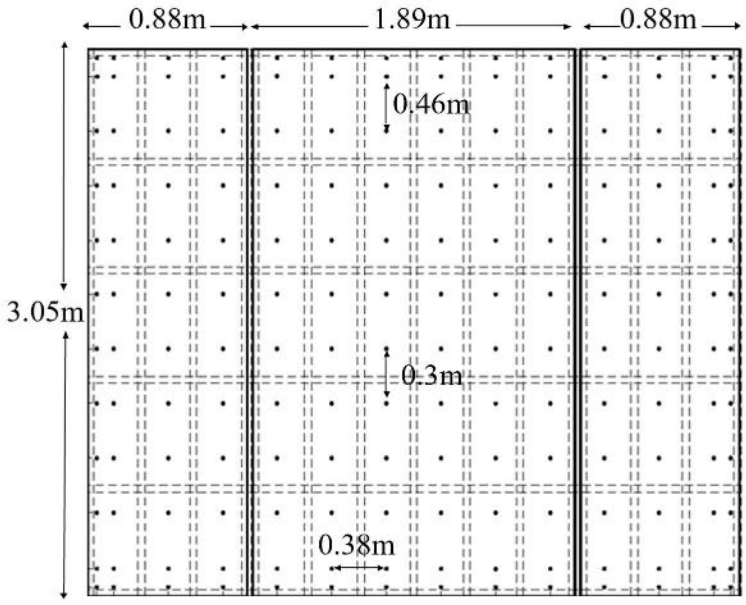

Figure 2.5. Pressure tap locations on the polycarbonate panels

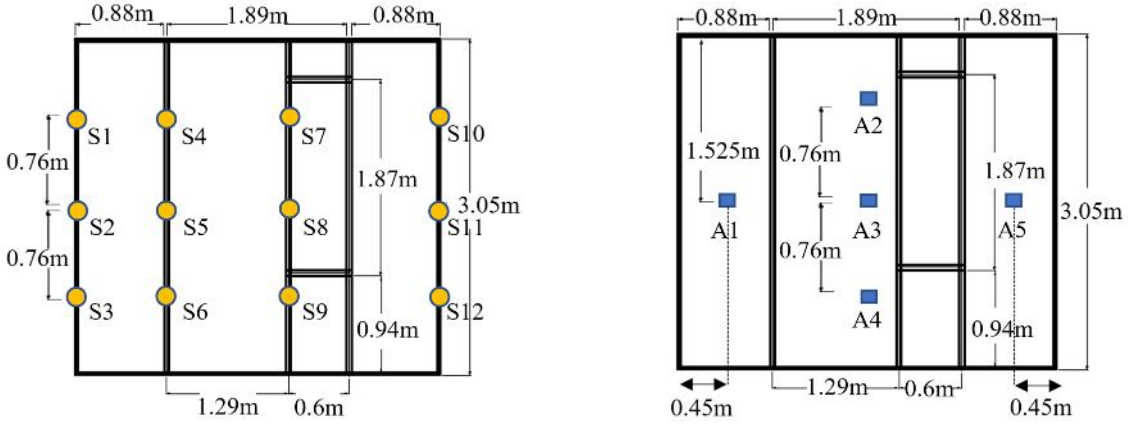

(a) (b)

Figure 2.6. Sensor locations on the actual curtainwall side: (a) strain gauges and (b) accelerometers

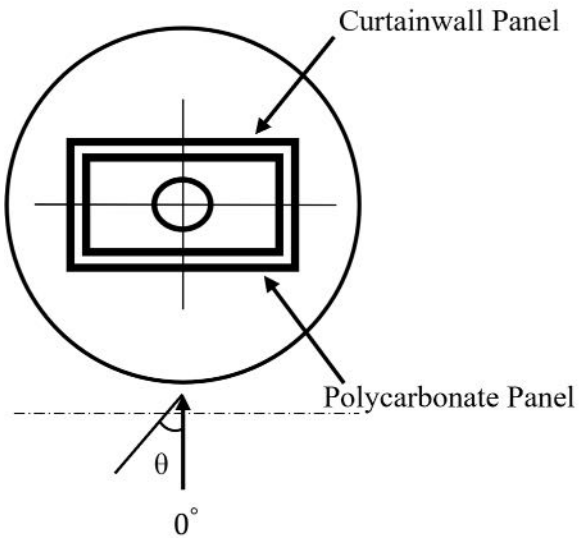

Figure 2.7. Wind direction (plan view)

Table 2.1. Testing protocol

Data obtained	Wind speed (m/s)	Wind direction θ (degree)	Test duration (mins)
Pressure	22.35 (50 mph)	0 to 180 (in 15-degree increments)	1
Acceleration and strain	22.35 (50 mph)	0 to 315 (in 45-degree increments)	10
	31.30 (70 mph)	0 to 315 (in 45-degree increments)	5
	40.23 (90 mph)	0 to 315 (in 45-degree increments)	5

2.3 Numerical modeling

2.3.1 Methodology

2.3.1.1 Single-skin curtainwall model

A finite element (FE) model of the single-skin façade curtainwall system is developed to reproduce the characteristics of wind-induced vibrations observed in the full-scale tests at the WOW EF and to subsequently assess the curtainwall's dynamic performance under various wind loadings. Midas Gen finite element analysis (FEA) software is used for FE modeling (MIDAS Information Technology Co., 2021). Figure 2.8 shows the developed

FE curtainwall model. The curtainwall model is composed of frames and glass, which are assembled by mechanical fixings (dry gasket system) or structural silicone (wet glazing).

Modeling frames: Beam elements with 6 degrees of freedom (DOFs) per node (12 DOFs in total) are used for modeling (i) the main frame (mullions and transoms) and (ii) the sash frame for the operable part as shown in Figure 2.9. The main frame includes mullions and transoms which are vertical and horizontal framing elements, respectively. The operable part is mounted to the main frame in the designated location shown in Figure 2.9. Nine different framing profiles are considered in Figure 2.10. The cross-sectional properties of each profile including area and second moments of area (I_{XX}, I_{YY}, and I_{XY}) are shown in Table 2.2, which are computed using CAD software. In calculating the second moment of area of profiles #1 and #2, the composite action of the two separate parts is also considered. The geometric properties are used to model the FE beam elements that represent the frames.

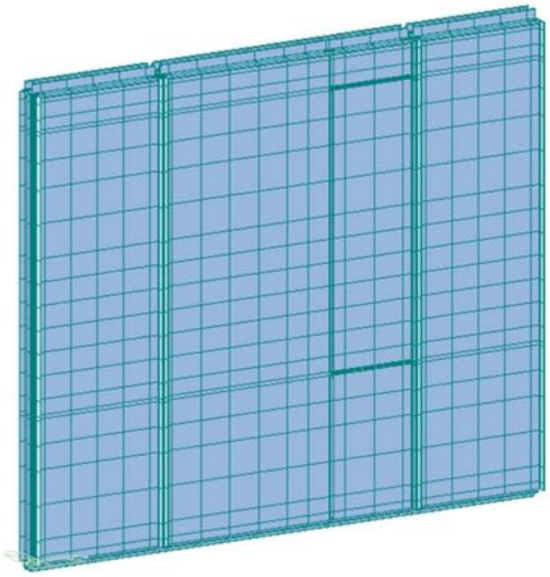

Figure 2.8. Developed FE model of the single-skin curtainwall.

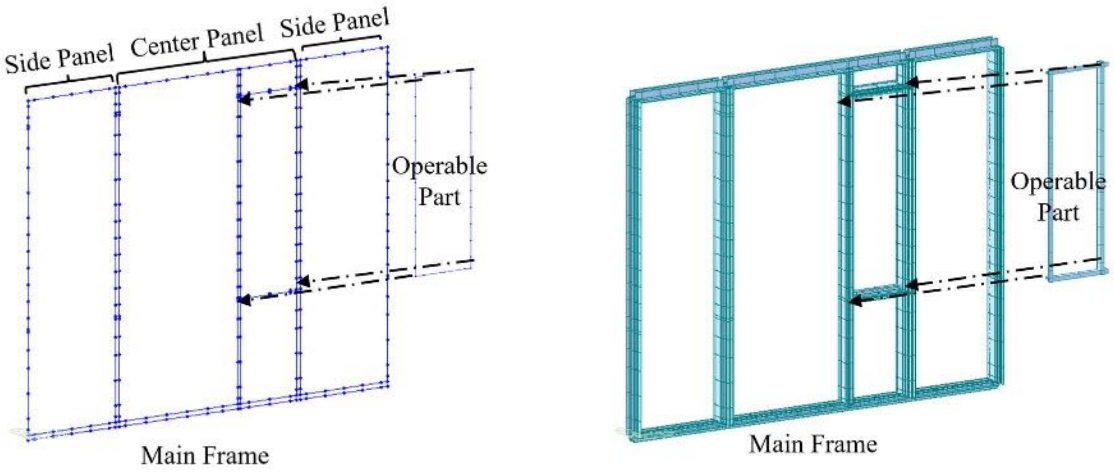

(a) (b)

Figure 2.9. The modeled main frame (mullions and transoms) and sash frame for the operable part: (a) The frames are modeled using beam elements; (b) 3D Rendering with framing profiles.

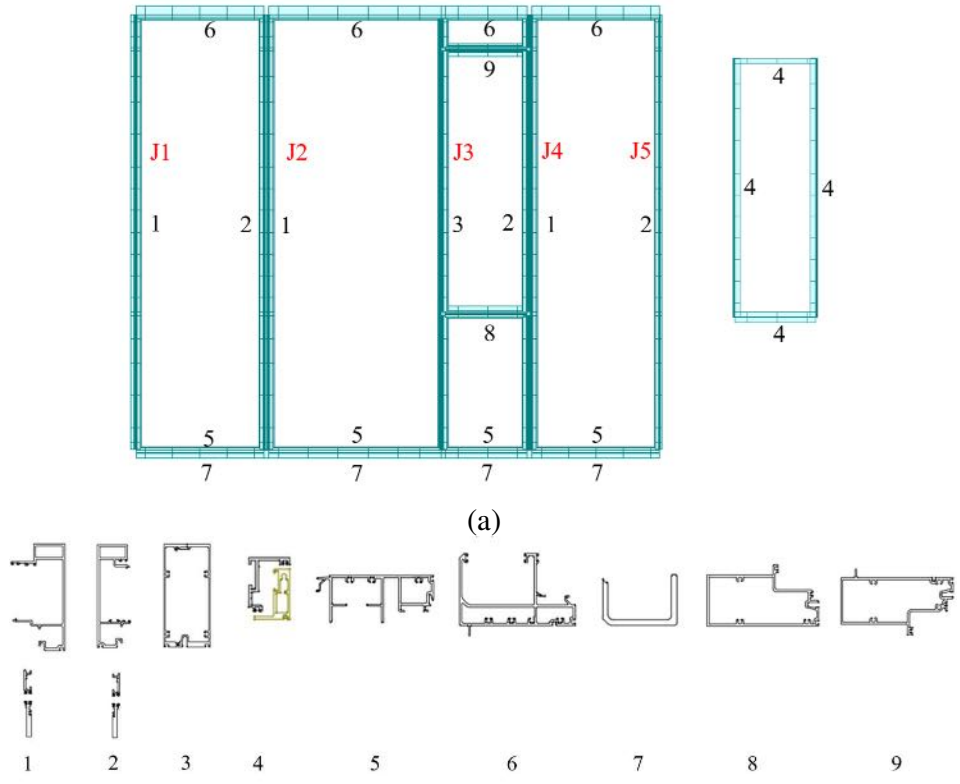

(a)

(b)

Figure 2.10. Framing profiles: (a) Location of the modeled profiles, and (b) cross sections of the nine framing profiles

Table 2.2. Cross-sectional properties of the framing profiles

	Framing Profile	Area (mm^2)	I_{XX} (mm^4)	I_{YY} (mm^4)	I_{XY} (mm^4)
1	Left Mullion	1652	3.77e6	5.53e5	1.93e5
2	Right Mullion	1587	3.64e6	2.84e5	1.74e5
3	Intermediate Mullion	1619	5.39e6	2.59e5	2.36e5
4	Operable	445	1.42e5	3.04e4	2.78e4
5	Bottom Transom	1329	2.76e6	4.00e5	4.49e4
6	Top Transom	1729	3.77e6	1.21e6	3.10e5
7	C-shape Beam	1187	1.40e6	3.66e5	5.54e4
8	Intermediate Bottom Transom	1355	3.53e6	1.05e6	2.56e5
9	Intermediate Top Transom	1355	3.54e6	8.95e5	1.91e5

Modeling connections between the frames: The mullion and transom in each panel are joined by a shared node (e.g., framing profiles #1 and #6 at the upper left corner in Figure 2.10). The connections of two neighboring mullion frames (e.g., framing profiles #2 and #1) are modeled using a set of elastic links to reproduce the mechanical coupling between the frames. Each elastic link has 6 degrees of freedom (DOFs) with translational and rotational stiffnesses to all local *x*-, *y*-, and *z*-directions. For example, Figure 2.11 demonstrates how two mullion frames between the side and the middle panels are assembled by using the 6-DOF elastic links. The same approach is used to model the intermediate mullion (profile #3) which is composed of two parts. The interaction between the main and sash frames is also modeled using the 6-DOF elastic links to mount the operable part to the main frame.

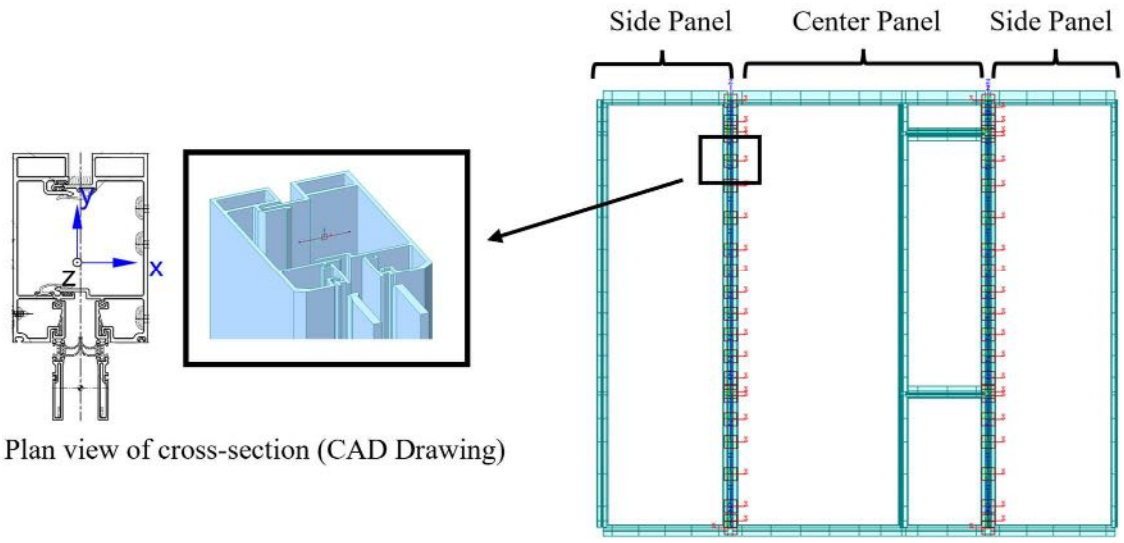

Figure 2.11. Modeling connection between the neighboring panels using 6-DOF elastic links.

Modeling glass: Glass modeling is of great importance because the glass covers most of the building façade and significantly affects the overall dynamic response of the system. Therefore, the glass properties including mass and stiffness need to be properly modeled to realistically reproduce the dynamic behavior. However, glass modeling is not often straightforward if multiple layers are used with insulated laminated glass, which is the case with the tested curtainwall system in this study. The glass used in the curtainwall system is a double-glazing unit (DGU), and its schematic drawing is shown in Figure 2.12. The DGU is composed of inner and outer glass layers with a gap that is maintained by a thermal spacer. The outer glass is a monolithic glass while the inner glass is a laminated glass where a polyvinyl butyral (PVB) interlayer is between the two layers of monolithic glass. Therefore, to numerically model it with a plate element, an equivalent glass thickness needs to be estimated to represent the properties of DGU. Table 2.3 summarizes the estimated equivalent properties for the 5 different types of glass used in the curtainwall. The hatching

code indicates the location of each glass. The effective thickness of the (inner) laminated glass is first estimated using the method by Galuppi and Royer-Carfagni (2012) which is shown in the 5th column of the table. The approach discussed in Annex C of Eurocode prEN 16612 (2015) is then adopted to back-calculate the overall effective stiffness of DGU and then its equivalent thickness. The thickness ratio *R* compares the equivalent DGU thickness to the sum of inner and outer layer thicknesses. The estimated equivalent DGU is overall thinner than the sum of the inner and outer layers. Therefore, the unit weight of the glass is increased to make it the same mass as the original DGU. This approach realistically models the stiffness and mass properties of DGU to reproduce the dynamic façade behavior.

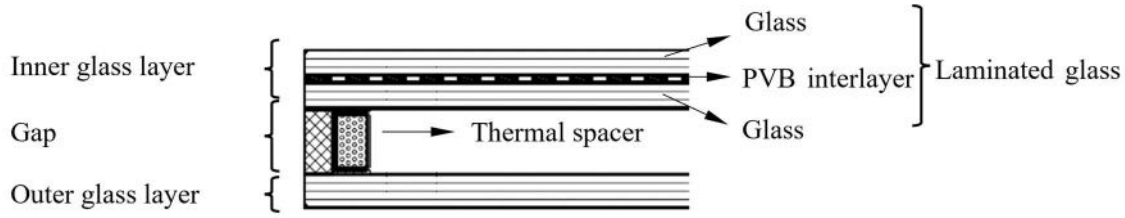

Figure 2.12. Schematic drawing of the double-glazing unit (DGU)

Table 2.3. Computed equivalent DGU thicknesses.

	Outer glass layer (mm)	Gap (mm)	Inner glass layer (with PVB) (mm)	Equivalent inner layer thickness (mm)	Equivalent DGU thickness (mm)	Thickness ratio (*R*)	Scaled unit weight (kg/m^3)
	6.35	12.70	10.29	9.75	**10.40**	0.65	3430
	4.76	15.88	4.76	4.76	**5.73**	0.60	3678
	6.35	12.70	10.29	9.27	**9.53**	0.61	3628
	6.35	12.70	10.29	9.07	**8.87**	0.58	3845
	10.00	12.00	6.00	6.00	**10.72**	0.67	3322

Assembling the modeled frames and glass: The glass and the frames in the tested curtainwall system are joined by structural silicone. In this study, the 6-DOF elastic links are used to numerically represent the silicone between the glass and the frames. Figure 2.13 shows the modeled curtain wall where the elastic links are used to assemble the glass and the frames.

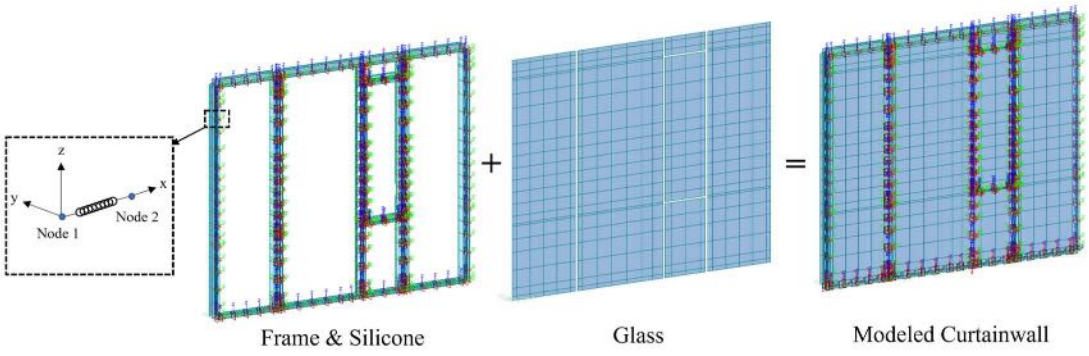

Figure 2.13. Modeled curtainwall with glass and frames assembled using elastic links (shown with the local axes).

2.3.1.2 Whole structure model

The full-scale curtainwall system tested at the WOW EF is composed of the supporting steel structure, polycarbonate panels, side walls, and roof as well as the actual single-skin curtainwall panels. Therefore, the development of the whole structure model would enable a fair comparison between the experimental data and the FE analysis results. Figure 2.14 shows the developed FE supporting steel structure model including the main steel structure connected to perimeter beams at the bottom. The perimeter beams are bolted to the turntable in the experiment, which are numerically modeled with hinge supports in the FE model as shown in the figure. The supporting steel structure has the same width and height as the single-skin curtainwall. The 12-DOF beam elements are also utilized to model the

beams and columns of the supporting steel structure. Figure 2.14 shows the framing profile details of the steel structure and Table 2.4 shows the cross-sectional properties of the framing profiles. The developed curtainwall model (Figure 2.8) is then mounted to the front side of the supporting structure as shown in Figure 2.15. The developed wooden frame and polycarbonate panel models are also attached to the rear side of the supporting structure. The wooden side walls are 3.05 m high and 1.80 m wide and have a thickness of 15 cm. The 4.00 m × 2.62 m wooden roof has a thickness of 8 cm.

The material properties used in modeling the whole structure are presented in

Table 2.5. The developed whole structure model is shown in Figure 2.16.

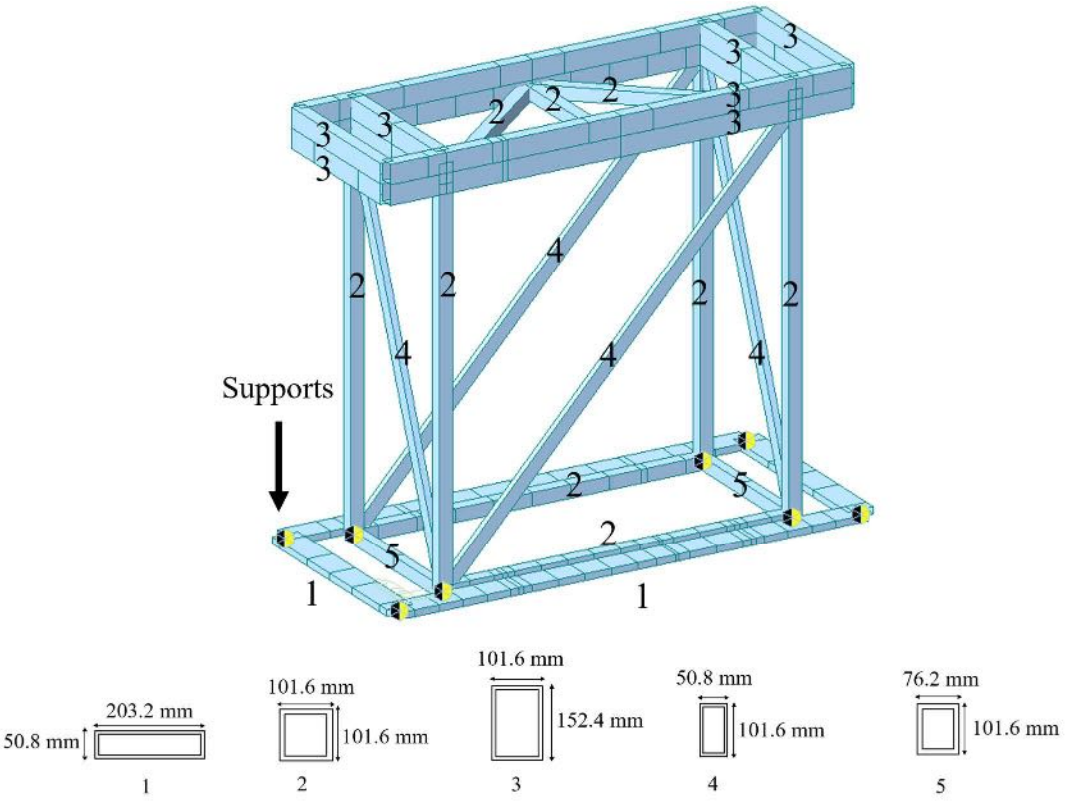

Figure 2.14. FE model of the supporting steel structure with its bolted connections to the turntable, framing layout, and the cross sections of the five framing profiles.

Table 2.4. Cross-sectional properties of the framing profiles of the supporting steel structure

Framing Profile	Area (mm^2)	I_{XX} (mm^4)	I_{YY} (mm^4)	I_{XY} (mm^4)
1	4470	1.72e6	1.89e7	5.17e6
2	3503	5.00e6	5.00e6	7.43e6
3	4470	1.36e7	7.06e6	1.40e7
4	2542	2.95e6	8.89e5	2.06e6
5	3026	3.98e6	2.45e6	4.52e6

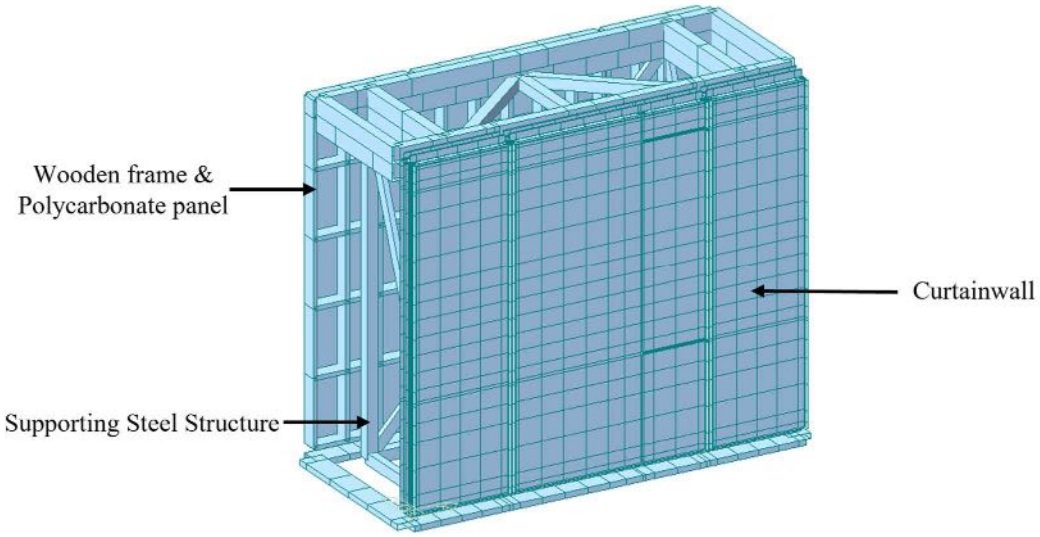

Figure 2.15. The curtainwall panel (front) and polycarbonate panel (rear) attached to the supporting steel structure.

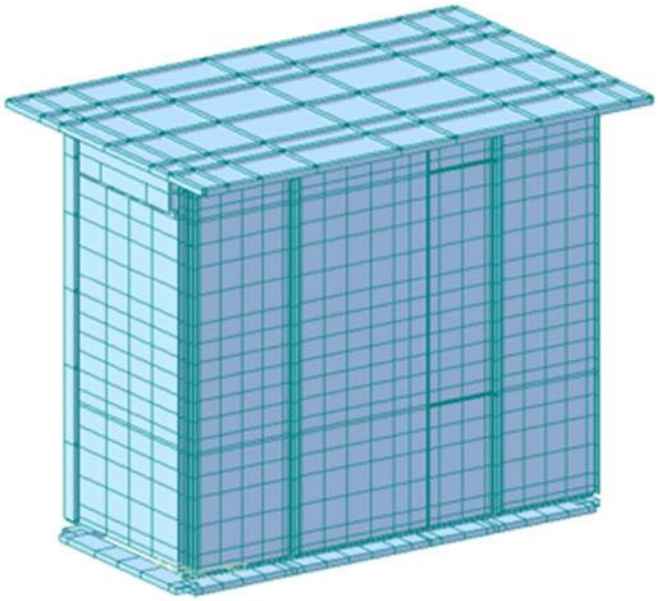

Figure 2.16. FE model of the whole structure including the supporting steel structure, curtainwall panels, polycarbonate panels, walls, and roof

Table 2.5. Material properties used in the FE model.

Material	Modulus, E (MPa)	Poisson ratio, ν	Density, ρ (kg/m^3)
Aluminum	70940	0.33	2768
Steel	200000	0.30	7861
Wood	4000	0.31	830
Polycarbonate	1793	0.31	1190

2.3.2 Calibration

The 110-pressure time history (TH) data obtained in terms of C_p (pressure coefficient) are used to calibrate the model parameters. Midas Gen FEA software requires nodal load time history input for dynamic analysis. Therefore, the C_p time histories are converted to pressure time histories using Equation (2.1) and to nodal load time histories using Equation (2.2) by considering the tributary area of each node. The pressure tap locations in the

experiment do not exactly coincide with the node locations, for which the time history data are interpolated.

$$p(t) = \frac{1}{2}\rho_{air} C_p {V_{ref}}^2 \tag{2.1}$$

where $p(t)$ is the pressure's time history, ρ_{air} is the air density, C_p is the pressure coefficient, and V_{ref} is the reference wind speed measured at the roof level of the tested specimen.

$$F_i(t) = p_i(t)\, A_i \tag{2.2}$$

where $F_i(t)$ is the wind load time history for node i, $p_i(t)$ the interpolated pressure's time history of the adjacent nodes, and A_i is the tributary area of the node i.

The calibration is conducted iteratively by tuning the model parameters until the numerical model reproduces a dynamic response comparable to the experiment data. The FE model is considered 'calibrated' if the root mean squares (RMS) of all acceleration (RMS_{ACC}) and strain (RMS_{STR}) responses are within 10 percent compared to the experimental data. The calibration flowchart is shown in Figure 2.17.

Table 2.6 summarizes the calibrated parameters and Figure 2.18 indicates the corresponding locations in the whole structure FE model.

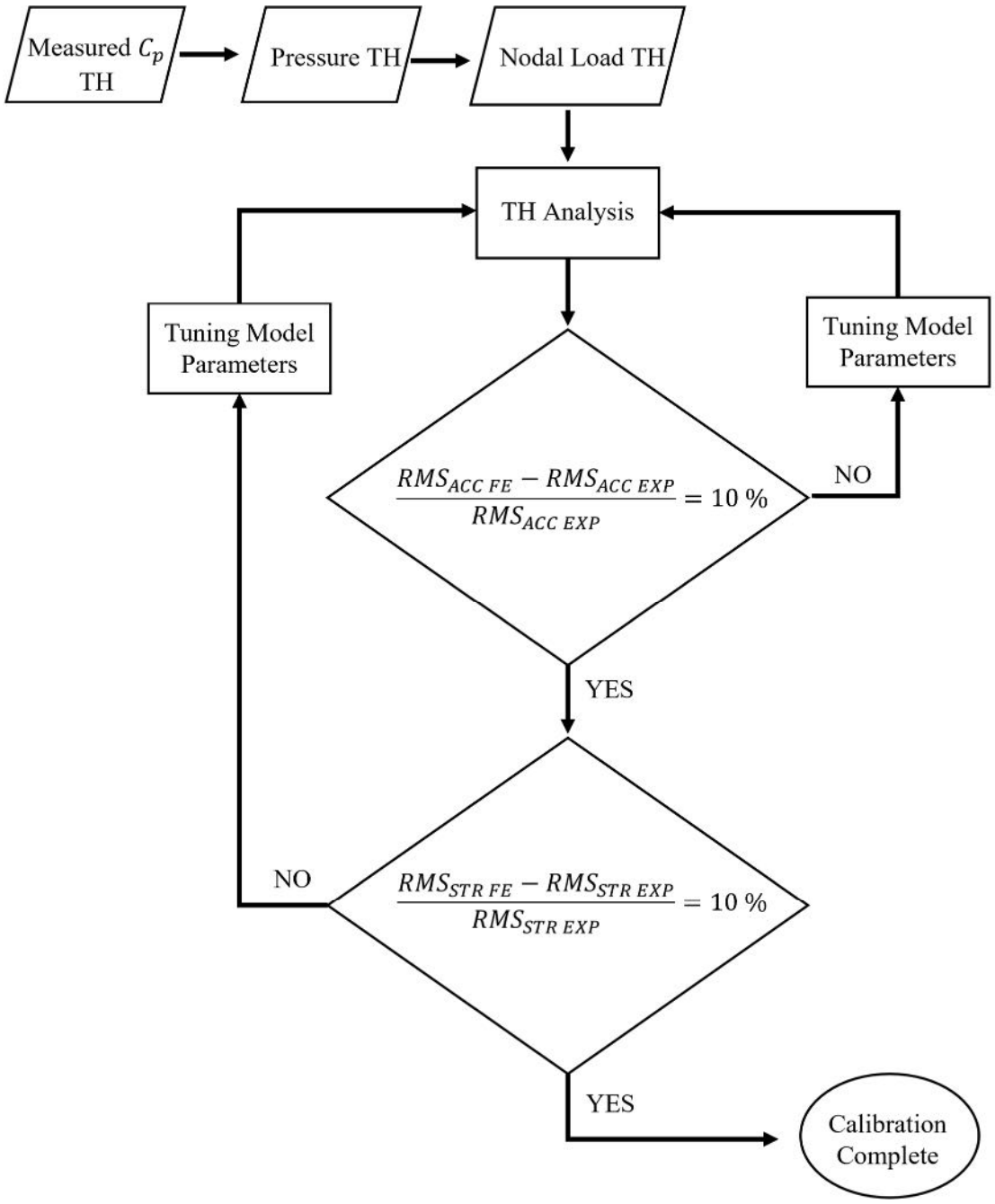

Figure 2.17. The summarized calibration process of the curtainwall FE model

Table 2.6. Critical internal parameters and their tuned values

# in Figure 2.18	Model parameters	Axial stiffness (kN/m)	Shear stiffness (kN/m)	Rotational stiffness (kN·m/rad)
1	Curtainwall's top connection to the steel structure	17513	17513	11.29
2	Curtainwall's bottom connection to the steel structure	5254	5254	3.38
3	The steel structure supports modeled with point springs	7005	7005	4.52
4	Inter-mullion connection	700	700	0.45
5	Center panel's silicone	175	175	0.11
6	Side panel's silicone	166	166	0.10

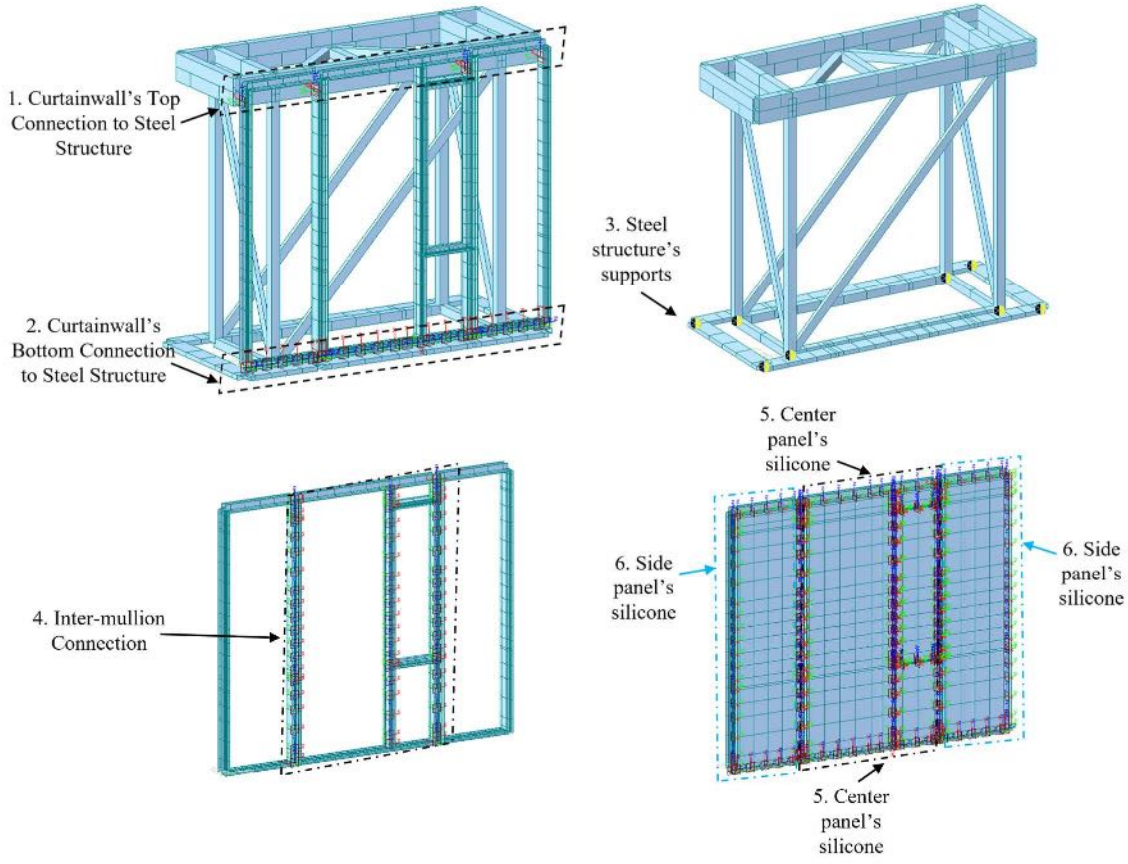

Figure 2.18. Location of the tuned internal parameters

The whole-structure FE model is calibrated for 22.35 m/s wind speed and normal wind direction (0°) to the surface of the façade. Figure 2.19 presents the acceleration response

of the calibrated whole-structure FE model compared to the experimental data. The results show a comparable root mean square (RMS) of acceleration time history response, with a difference of less than 10 percent, between the FE and the experimental results, meeting the calibration criterion. Figure 2.20 shows the comparison of the acceleration response in the frequency domain, where the power spectral density (PSD) of the acceleration response of the whole-structure FE model is plotted against the experimental response. A major frequency is observed at 4.2 Hz, which is reflected in all 5 accelerometers' PSDs. It is observed that the numerical results succeed in precisely capturing the presence of higher dominant frequencies of 16 H and 24 Hz, observed in the experimental response. The area under the power spectral density (PSD) of the response represents the total power contained within the frequency range of interest. The FE model reproduces the experimental acceleration spectra at all five locations, with the disparity in the integral of the PSD spectra being below 6 percent for accelerometer 1, below 17 percent for accelerometers 2, 4, and 5, and below 28 percent for accelerometer 3. The increased relative deviation in the integral of the PSD spectra observed for accelerometer 3 can be attributed to its geometric positioning at the center point of the glazing's center panel. The vibration mode related to the 2nd major frequency is most significantly pronounced at this specific location, thereby effectively contributing to the observed discrepancy.

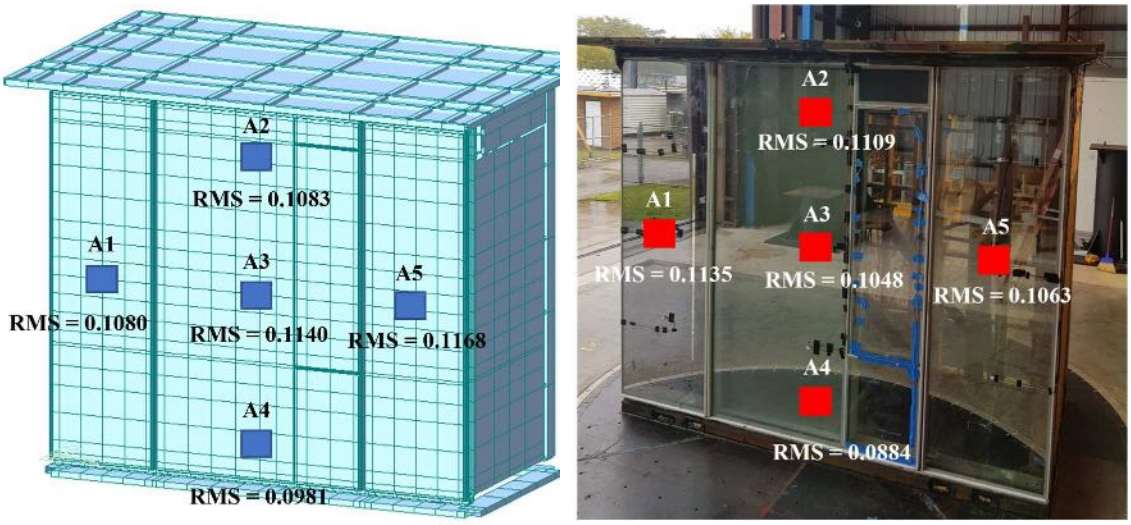

(a) (b)

Figure 2.19. RMS of acceleration (m/s^2) time history: (a) Calibrated whole structure FE model, and (b) Experimental results for 22.35 m/s, and 0° wind.

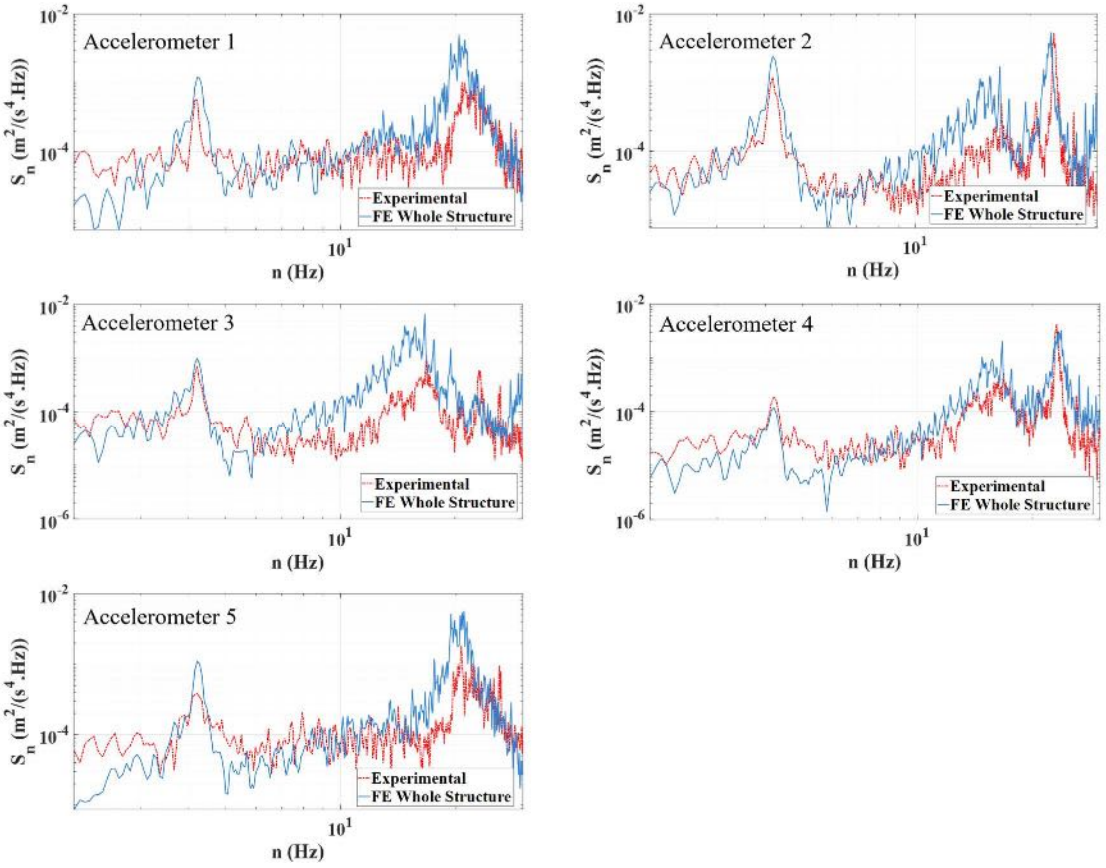

Figure 2.20. Acceleration PSDs of the whole structure FE model compared to the experimental response for 22.35 m/s and 0° wind.

Figure 2.21 shows the RMS of the strain time history response obtained from the numerical model compared to the experimental data. No data is available for strain gauge 4 because the gauge was found faulty later. Overall, the calibration criterion of securing less than 10 percent difference between the numerical and the experimental result is achieved except where strain gauges 5, 6, 8, and 9 are located, where more than 10 percent of differences are present. However, this is considered acceptable, and no further calibration is conducted because the strain gauges in the experiment are located on the extreme fiber of the mullion's cross-section while the FE model employs a beam model that has limitations in presenting the behavior far from the cross-section's neutral axis. Nevertheless, the strain responses in the frequency domain are comparable. For example, the strain PSDs at the center (i.e., gauges 2, 5, 8, and 11) that deform the most in bending are in good agreement as shown in Figure 2.22, as the discrepancy in the integral of the strain PSD spectra is found to be less than 10 percent for strain gauges 2, 5, 8, and 11.

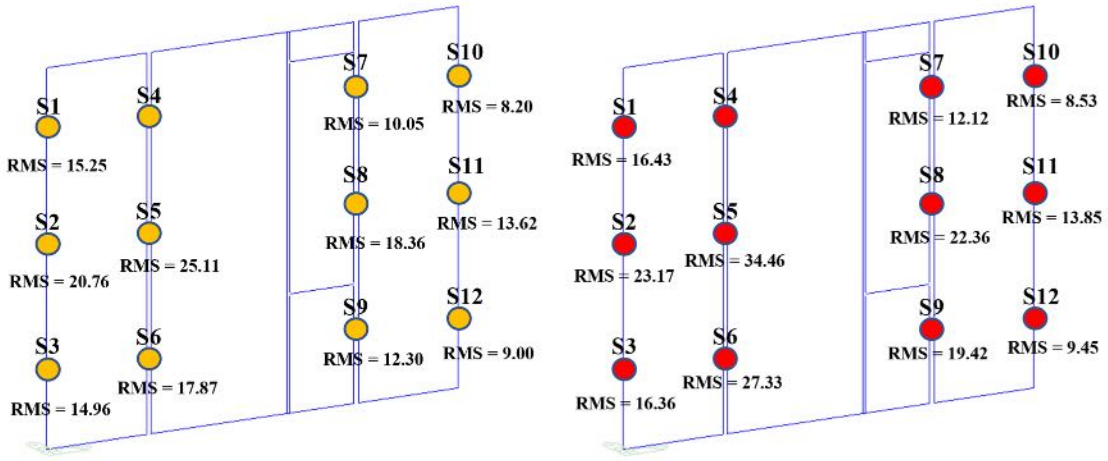

(a) (b)

Figure 2.21. RMS of strain (micro-strain) time history of the (a) calibrated whole structure FE model, compared to (b) experimental results for 22.35 m/s, and 0° wind.

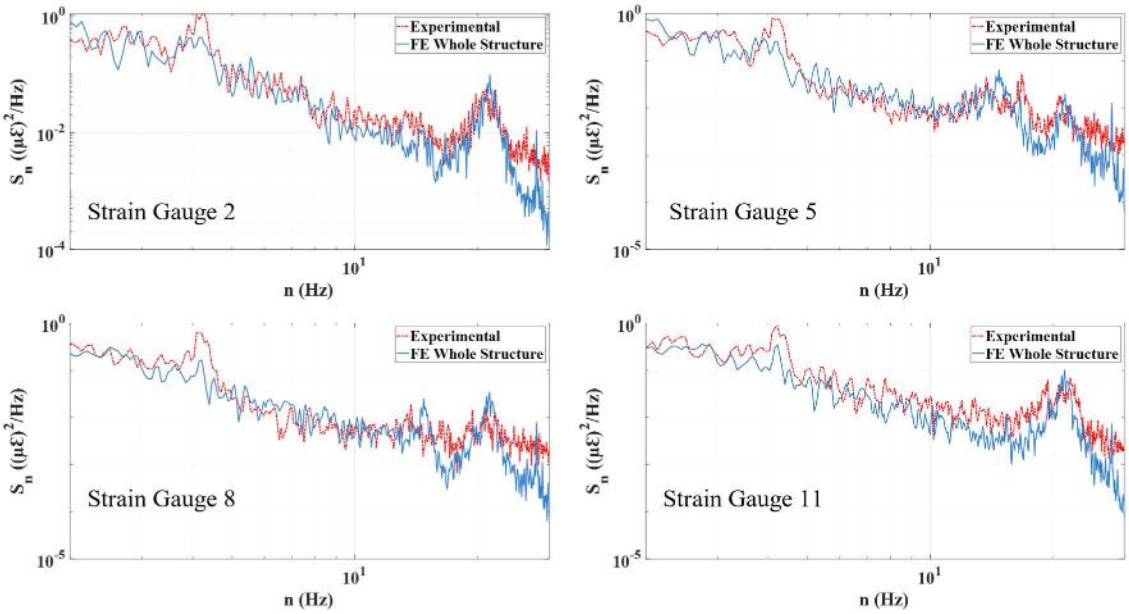

Figure 2.22. Strain PSDs of the whole-structure FE model compared to the experimental response for 22.35 m/s and 0° wind.

2.4 Numerical analysis

2.4.1 Analysis of the whole structure FE model

The calibrated FE model is used to estimate the dynamic responses under different wind loadings for model validation. The validation criterion requires achieving a difference of less than 15 percent between the root mean square (RMS) of the acceleration time history response of the whole structure FE model and the corresponding experimental response. The chosen criterion is intentionally less stringent than the calibration criterion due to the nature of their respective applications. The calibration process is performed for a specific wind speed and direction, specifically 22.35 m/s and 0°. On the other hand, the validation is conducted across a range of wind speeds and directions, where higher discrepancies between numerical and experimental results may occur. Two different wind speeds, 31.30 m/s, and 40.23 m/s, and three different wind directions of 0°, 45°, and 90° are considered. The same C_p values are used to estimate the input nodal load time histories for each wind speed.

Table 2.7 shows the validation results for 31.30 m/s and 0° wind. The comparison of RMS of acceleration time history results shows less than 10 percent difference between the numerical and the experimental response. The acceleration PSDs are plotted in Figure 2.23 for all 5 locations. The validation results still show the acceleration PSDs are captured well for higher wind speeds. As shown in Table 2.8 in the reproduced wind-tunnel test of 40.23 m/s and 0°, the acceleration response of the side panels of the numerical model shows less than a 13 percent of difference from the experimental response. The difference is higher for the central accelerometer 3 located on the midspan of the glazing, showing a difference

of 15 percent, while the level of difference for accelerometers 2 and 4 remains below 10 percent. Comparison of the responses in the frequency domain are observed in Figure 2.24.

Table 2.7. RMS of acceleration (m/s^2) time history of the validated whole structure FE model, compared with the experimental results for 31.30 m/s and 0° wind.

Accelerometer	Whole structure FE model acceleration time history RMS (m/s^2)	Experimental acceleration time history RMS (m/s^2)	Difference (%)
1	0.4489	0.4925	8.9
2	0.3186	0.3304	3.6
3	0.3400	0.3200	6.2
4	0.3240	0.3162	2.5
5	0.4798	0.5076	5.5

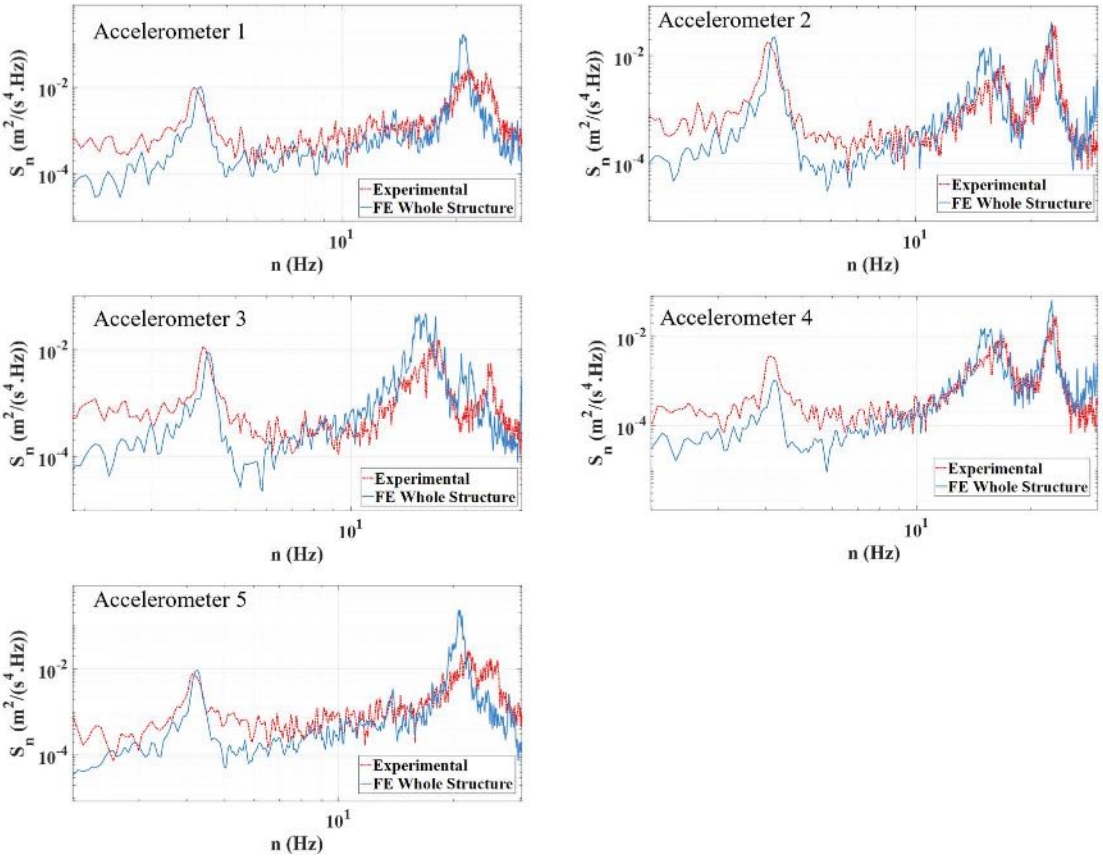

Figure 2.23. Acceleration PSDs of the whole structure FE model compared with the experimental response for 31.30 m/s and 0° wind.

Table 2.8. RMS of acceleration (m/s^2) time history of the validated whole structure FE model compared to the experimental response for 40.23 m/s and 0° wind.

Accelerometer	Whole structure FE mode acceleration time history RMS (m/s^2)	Experimental acceleration time history RMS (m/s^2)	Difference (%)
1	0.7108	0.8131	12.6
2	0.5265	0.5213	1.0
3	0.5449	0.4781	14.0
4	0.5358	0.4909	9.1
5	0.7267	0.8105	10.3

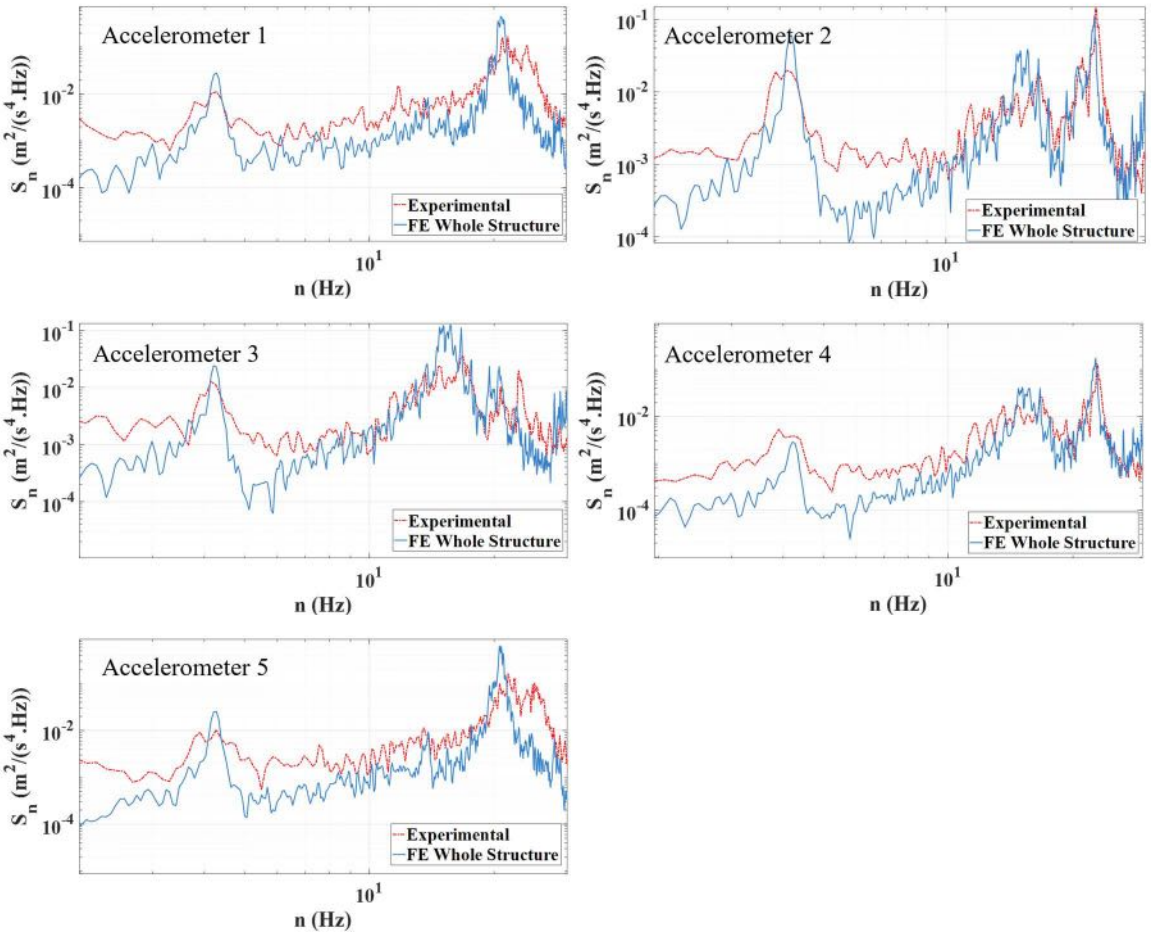

Figure 2.24. Acceleration PSDs of the whole structure FE model compared to the experimental response for 40.23 m/s and 0° wind.

Table 2.9 and Figure 2.25 show the analysis results for the 40.23 m/s wind speed and 45° direction. The dynamic response is captured by the FE model with less than 10 percent

difference. Table 2.10 and Figure 2.26 show the results for the case of 40.23 m/s and 90° wind direction. Despite the presence of additional differences, the numerical results and experimental data still exhibit a good level of agreement, as the parameters are not calibrated for the 90° wind direction.

Table 2.9. RMS of acceleration (m/s^2) time history of the validated whole structure FE model compared to the experimental response for 40.23 m/s and 45° wind.

Accelerometer	Whole structure FE mode acceleration time history RMS (m/s^2)	Experimental acceleration time history RMS (m/s^2)	Difference (%)
1	0.7101	0.7422	4.3
2	0.4415	0.4835	8.7
3	0.4106	0.4343	5.5
4	0.3962	0.4260	7.0
5	0.6617	0.6988	5.3

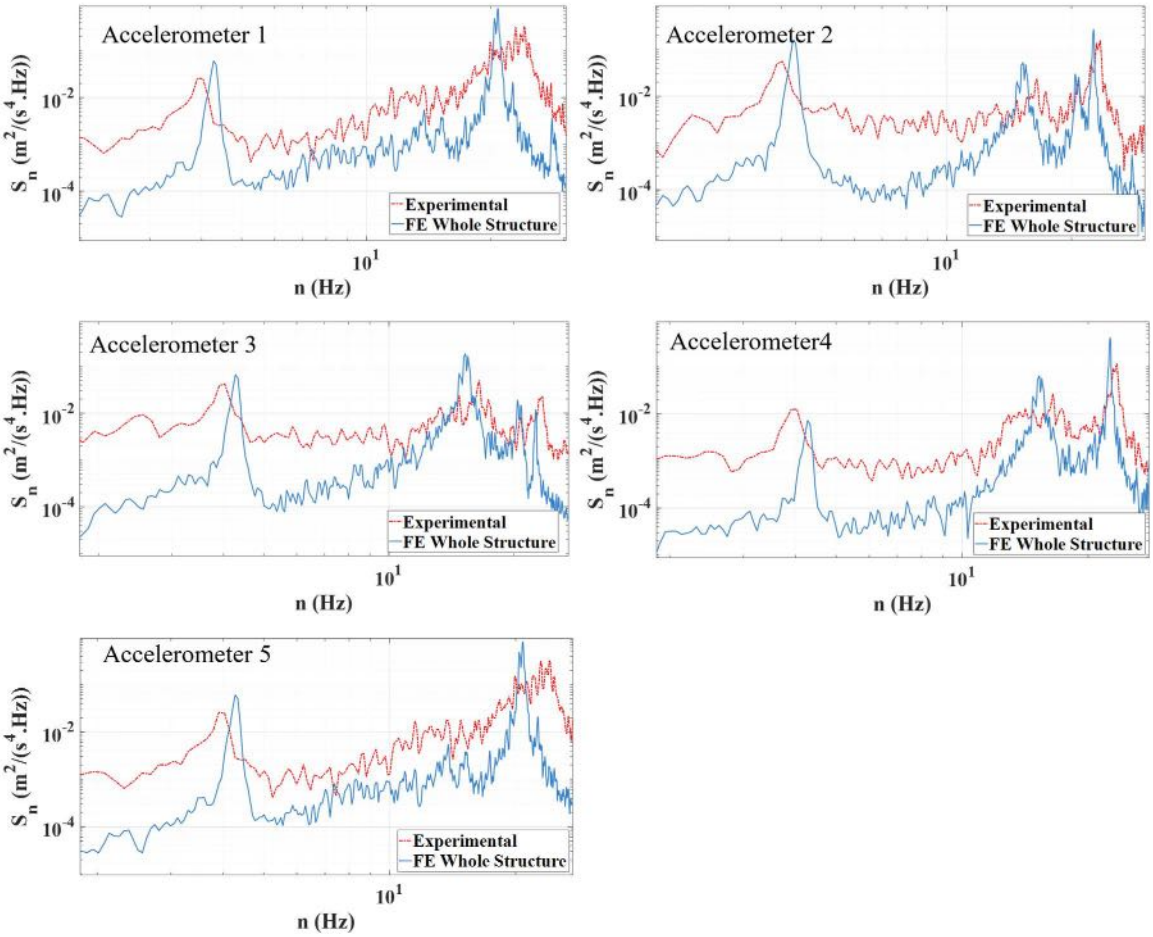

Figure 2.25. Acceleration PSDs of the whole structure FE model compared to the experimental response for 40.23 m/s and 45° wind.

Table 2.10. RMS of acceleration (m/s^2) time history of the validated whole structure FE model compared to the experimental response for 40.23 m/s and 90° wind.

Accelerometer	Whole structure FE mode acceleration time history RMS (m/s^2)	Experimental acceleration time history RMS (m/s^2)	Difference (%)
1	0.9355	1.0400	10.0
2	0.6582	0.5983	10.0
3	0.6086	0.5181	17.5
4	0.6294	0.5068	24.2
5	0.7879	0.8603	8.4

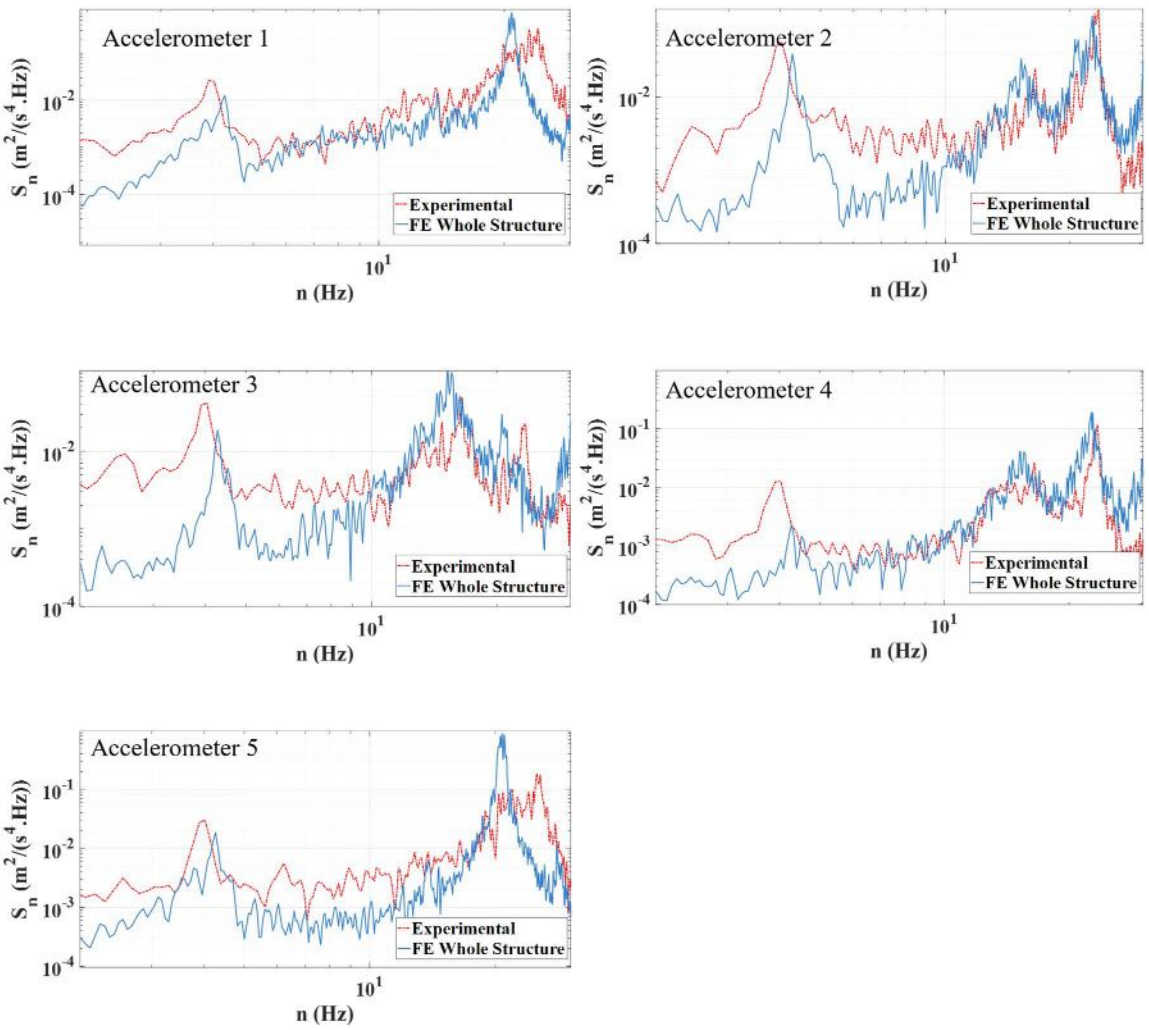

Figure 2.26. Acceleration PSDs of the whole structure FE model compared to the experimental response for 40.23 m/s and 90° wind.

2.4.2 Analysis of the façade-only FE model

The common practice in the façade industry is modeling the façade without the building structure for numerical analysis. This approach appears rational in the engineering practice because modeling the entire system including the building structure as well as the curtainwall would be prohibitively time-consuming. Instead, the connection to the building structures is typically modeled with simplified boundary conditions such as hinges or fixed ends. Then, this raises questions about how much difference would be shown in the

simulated dynamic behavior between the numerical model with and without the building structure modeled. This section addresses this issue by analyzing a 'façade-only model' in comparison with the whole structure model discussed in the previous section.

The façade-only FE model is developed by simply removing all parts except the single-skin façade curtainwall part from the calibrated/validate whole structure FE model. The boundary conditions of the façade-only model include the connections to the steel structure, at the top and the bottom, as shown in Figure 2.18 for which 6-DOF point springs are used. Figure 2.27 and Figure 2.28 compare the simulation results of the façade-only model to the experimental data obtained for 22.35 m/s and 0° wind. The results are analyzed in both time and frequency domains. The acceleration RMS results are relatively comparable for the center panel while a major difference of more than 25 percent is shown in the side panels (A1 and A5). The difference is more remarkable when the PSDs are compared. A major frequency at 4.2 Hz is clearly missing in the numerical analysis results and the PSD amplitude is overall higher in the high-frequency range. Therefore, the façade-only model does not appear to properly capture the wind-induced dynamic behavior, while it can be reproduced by the whole-structure FE model with high fidelity. We will investigate this further in the next section.

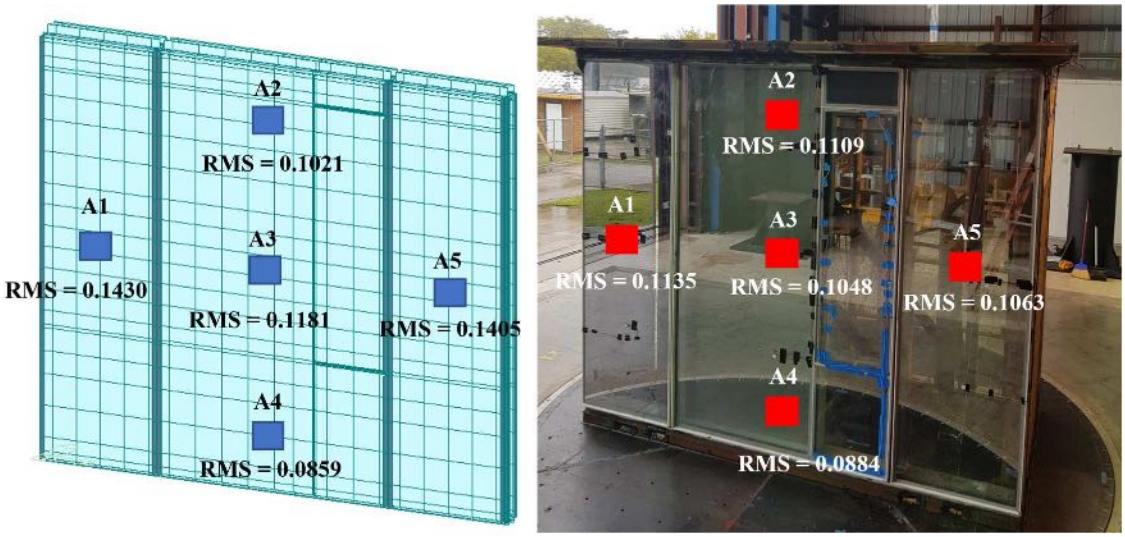

(a) (b)

Figure 2.27. RMS of acceleration (m/s^2) time history of (a) the validated façade-only FE model, compared to (b) experimental results for 22.35 m/s, and 0° wind.

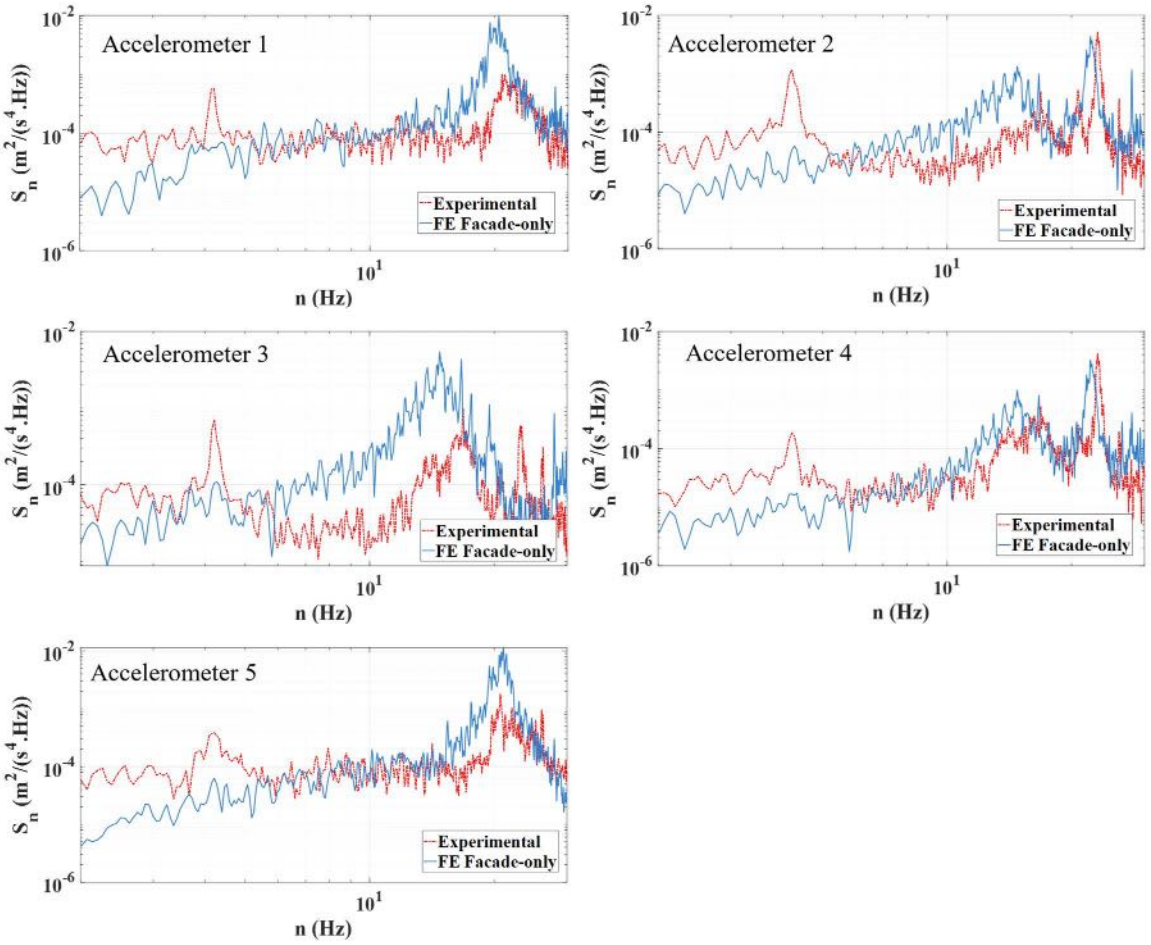

Figure 2.28. Acceleration PSDs of the façade-only FE model compared to the experimental response for 22.35 m/s and 0° wind.

2.4.3 Effect of façade-structure interaction

Eigen-analysis is conducted to investigate where this difference comes from. The eigen-analyses are conducted for both FE models (i.e., the whole structure and façade-only models). The results, i.e., natural frequencies and mode shapes, are shown in Figure 2.29. The side panels, where accelerometers 1 and 5 are located, are excited near 23 Hz. The middle panel shows a major mode of vibration near both 15 and 24 Hz, which also affects the dynamic response of the operable window that belongs to the middle panel. The façade-only FE model is completely missing the 1st natural frequency of the whole structure

system near 4 Hz. However, the other natural frequencies are similarly captured by both models. Therefore, it can be translated that the natural frequency near 4 Hz originates from the interaction between the façade and its supporting building structure, while the higher natural frequencies are from the façade itself. A system identification method is adopted to investigate if the same conclusion can be made with the experiment data. To this end, the Eigensystem Realization Algorithm-Observer Kalman filter Identification-Output Only (ERA-OKID-OO) method by Chang and Pakzad (2014), is employed to develop a stabilization diagram of the acceleration data obtained from the experiment. Figure 2.30 shows the stability diagram, where a solid vertical line of stable poles is an indicator of a true mode of vibration, i.e., near 4 Hz, 16 Hz, and 24 Hz. These major frequencies are confirmed by the eigen analysis results on the whole structure FE model. However, the solid vertical line at 4 Hz is different from the lines at 16 and 24 Hz in the sense that the stable poles are realized for a much higher model order (above 100) while the stable poles at 16 and 24 Hz are realized at a lower order (as low as 20). The indication of a weak signal near 4 Hz uncovers that the 4 Hz natural frequency originated from the contribution of the supporting structure because the sensors (accelerometers) were only mounted to the façade panels and were limited to capture the 4 Hz mode of the whole structure. On the other hand, the strong signals near 16 and 24 Hz diagnoses the other two major frequencies are contributed by the curtainwall itself.

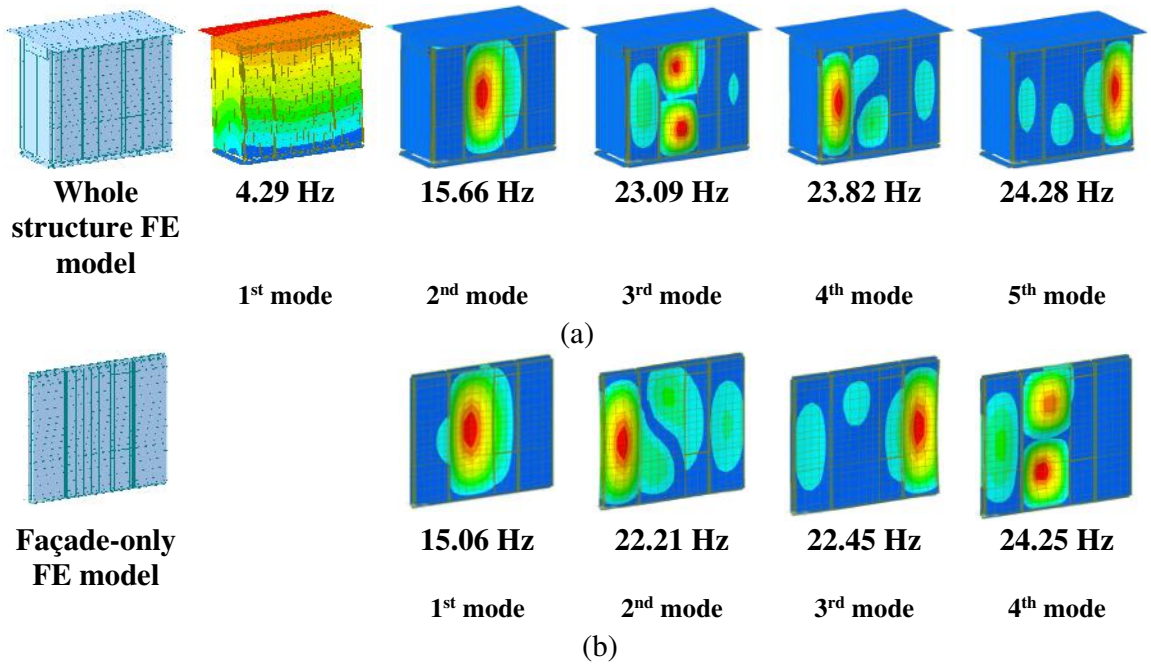

Figure 2.29. Eigen analysis results: (a) Whole structure FE model, and (b) Façade-only FE model.

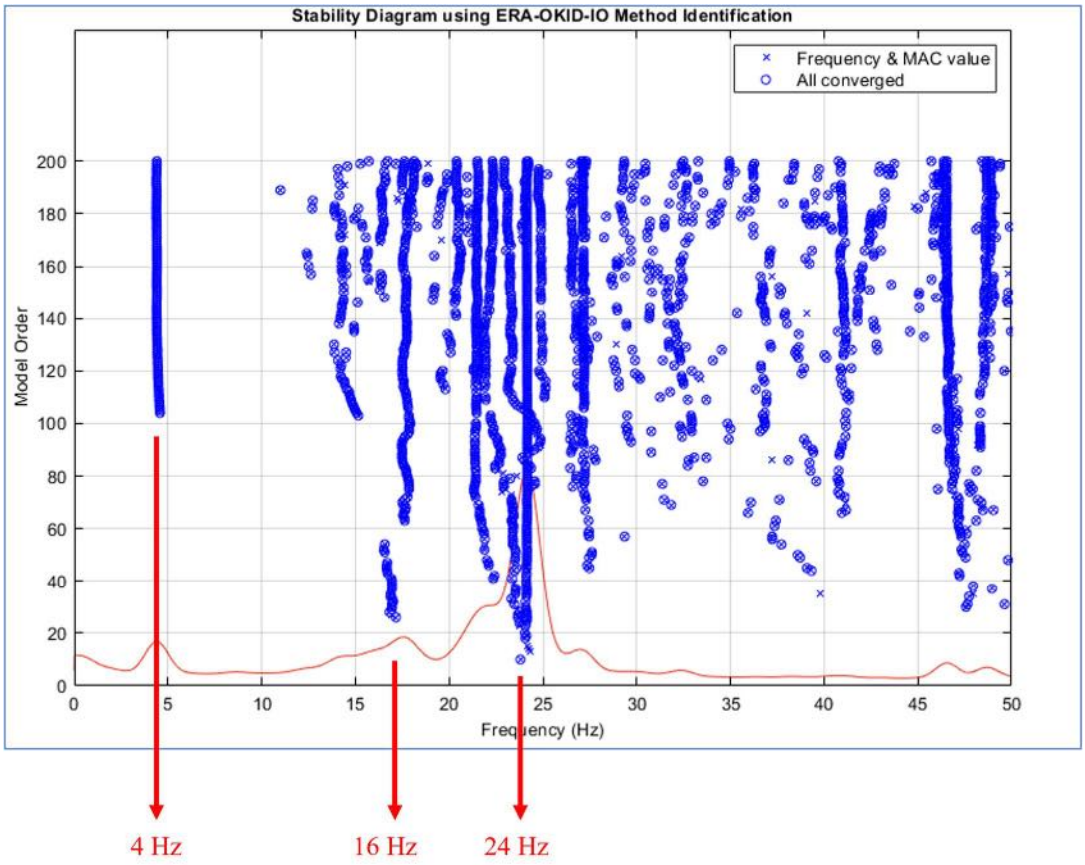

Figure 2.30. The stability diagram of the ERA-OKID-OO approach applied to the acceleration response obtained from the experiment.

The acceleration PSDs at location #3 of the two numerical models are compared to the corresponding experimental data in Figure 2.31. The façade-only FE model is overestimating the response near 16 Hz. This can be due to the fact that the façade-only FE model is generally less deformable than the whole structure FE model, where the façade is effectively interacting with a more massive building structure. The façade-only FE model is clearly missing the major lower frequency. This can be regarded as a significant oversight when designing the optimal façade performance since the dynamic effects of this wind-induced resonant response can be ignored at the design stage.

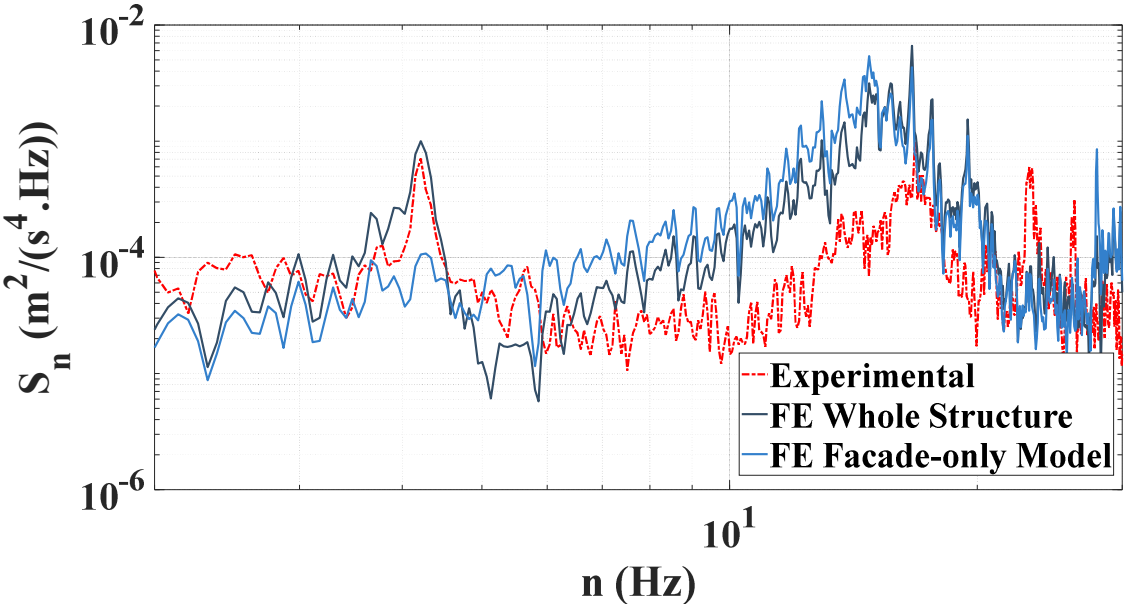

Figure 2.31. Acceleration PSD response of the whole structure FE model compared to the façade-only FE model compared to the experimental response.

Figure 2.32 compares the acceleration PSD response of the experimental and whole structure FE model at location #2 for 22.35 m/s and 0° wind, with a hypothetical FE whole structure model with a more flexible supporting structure. The material property of the supporting steel structure, the modulus of elasticity (i.e., E) is decreased to 20000 Mpa, to increase its flexibility. As observed in the figure, the 1st major frequency of the hypothetical FE model, which originates from the interaction of the façade and the supporting structure, is decreased from 4.29 Hz to 2.99 Hz. Also, can be observed in the figure that the peaks of the 2nd and 3rd major frequencies are decreased by 9.1 percent, and 8.6 percent, respectively, due to the additional flexibility of the system. Table 2.11 shows that the FE RMS of the acceleration time history decreased by 14.5 percent due to the additional flexibility of the supporting structure, compared to the original FE model. This shows that the flexibility or

rigidity of the supporting structure can meaningfully affect the dynamic response of the façade.

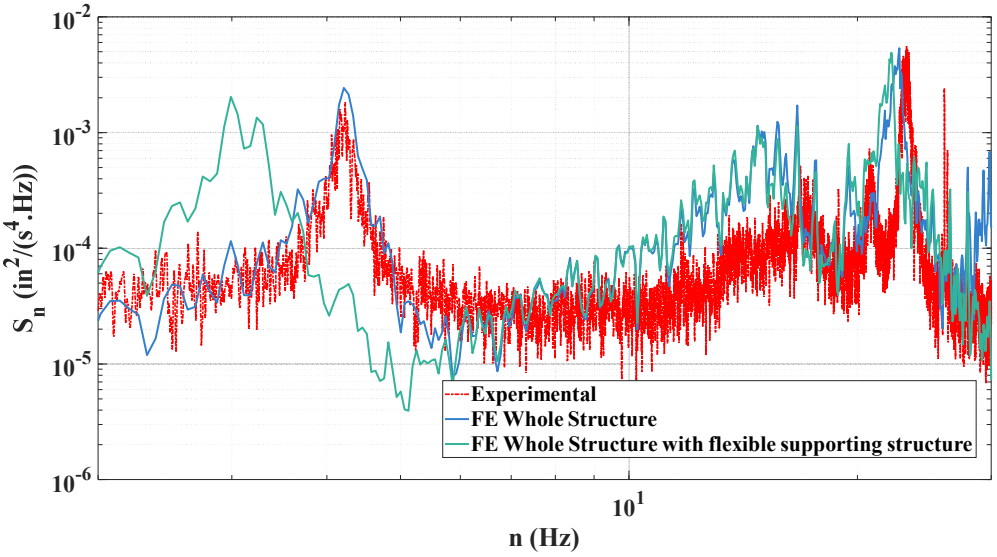

Figure 2.32. The acceleration PSD response of the whole structure FE model compared to the hypothetical FE model with flexible supporting structure compared to the experimental response.

Table 2.11. RMS of acceleration (m/s^2) time history (location #2) of the hypothetical whole structure FE model with a flexible supporting structure, compared to the original FE whole structure model and corresponding experimental results for 22.35 m/s and 0° wind.

Whole structure FE model (original)	Whole structure FE model with flexible supporting structure	Difference (%)
0.1083 m/s^2	0.0926 m/s^2	14.5

2.4.4 Effect of vertical protrusions

Vertical protrusions, such as fins, offer a combination of functional and aesthetic benefits in glass curtainwall facades, contributing to energy efficiency, visual appeal, comfort, and structural performance, while can have potential impacts on the wind-induced dynamic performance of the curtainwall system. The influence of vertical protrusions on the

dynamic response of the curtainwall system is investigated. To analyze the effect of the vertical protrusions, they are numerically modeled as beam elements, with their corresponding cross-sections, and then connected to the main mullion using 6-DOF elastic links. The assembled fins are added to the previously calibrated whole structure FE model and then subjected to 22.35 m/s and 0° wind. Figure 2.33 compares the acceleration response of the whole structure FE model with vertical protrusions with the measured response of the tested specimen.

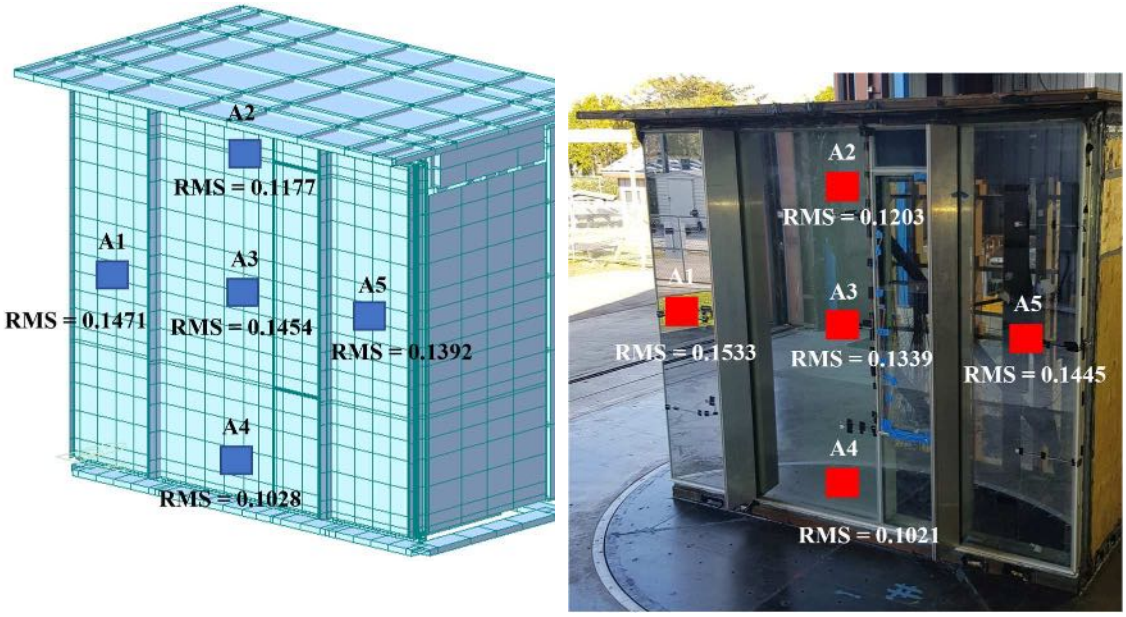

(a) (b)

Figure 2.33. RMS of acceleration (m/s^2) time history of (a) the validated whole structure FE model with vertical protrusions compared to (b) the experimental data for 22.35 m/s, and 0° wind.

An increase in acceleration is observed with the installation of vertical protrusions. For example, Table 2.12 compares the RMS of the acceleration response at location #2, whereby about 8% of the increase is observed. The numerical result obtained from the FE model with the vertical protrusions also reproduces the dynamic behavior. The model also captures the major frequencies as shown in Figure 2.34. Vertical protrusions add stiffness

to the system, which therefore increases the overall acceleration level. The comparison of the Power Spectral Density (PSD) of the acceleration response of the FE models at location #2, for both systems (with and without vertical protrusions) as illustrated in Figure 2.35, validates an increase in the stiffness of the system. Specifically, the second and third major frequencies have shown an increase from 15.66 Hz to 16.12 Hz, and from 23.09 Hz to 23.88 Hz, respectively. The first major frequency also exhibits a subtle increase from 4.29 Hz to 4.37 Hz. This can also be explained by Figure 2.36. The figure shows the experimental PSD response normalized by $\frac{U}{b}$ factor, where U is the wind speed mean measured at the curtainwall's roof height as 22 m/s, and b is the curtainwall's width equal to 3.65 m. As shown in the figure, the 1st and the 2nd normalized frequencies (i.e., 0.66, and 2.65, which are normalized values of experimental major frequencies of 4 Hz and 16 Hz, respectively) are in the increasing range of the spectrum. This implies that an increase in the frequency (stiffness) will lead to an increase in resonant dynamic effects. Higher overall acceleration levels indicate higher levels of wind-induced vibrations, which may potentially increase the system's susceptibility to water ingress scenarios.

Table 2.12. RMS of acceleration (m/s^2) time history (location #2) of the whole structure FE model without and with vertical protrusions, compared to the corresponding experimental results for 22.35 m/s and 0° wind.

The experimental model without vertical protrusions	The experimental model with vertical protrusions	Whole structure FE model without vertical protrusions	Whole structure FE model with vertical protrusions
0.1109 m/s^2	0.1203 m/s^2	0.1083 m/s^2	0.1177 m/s^2

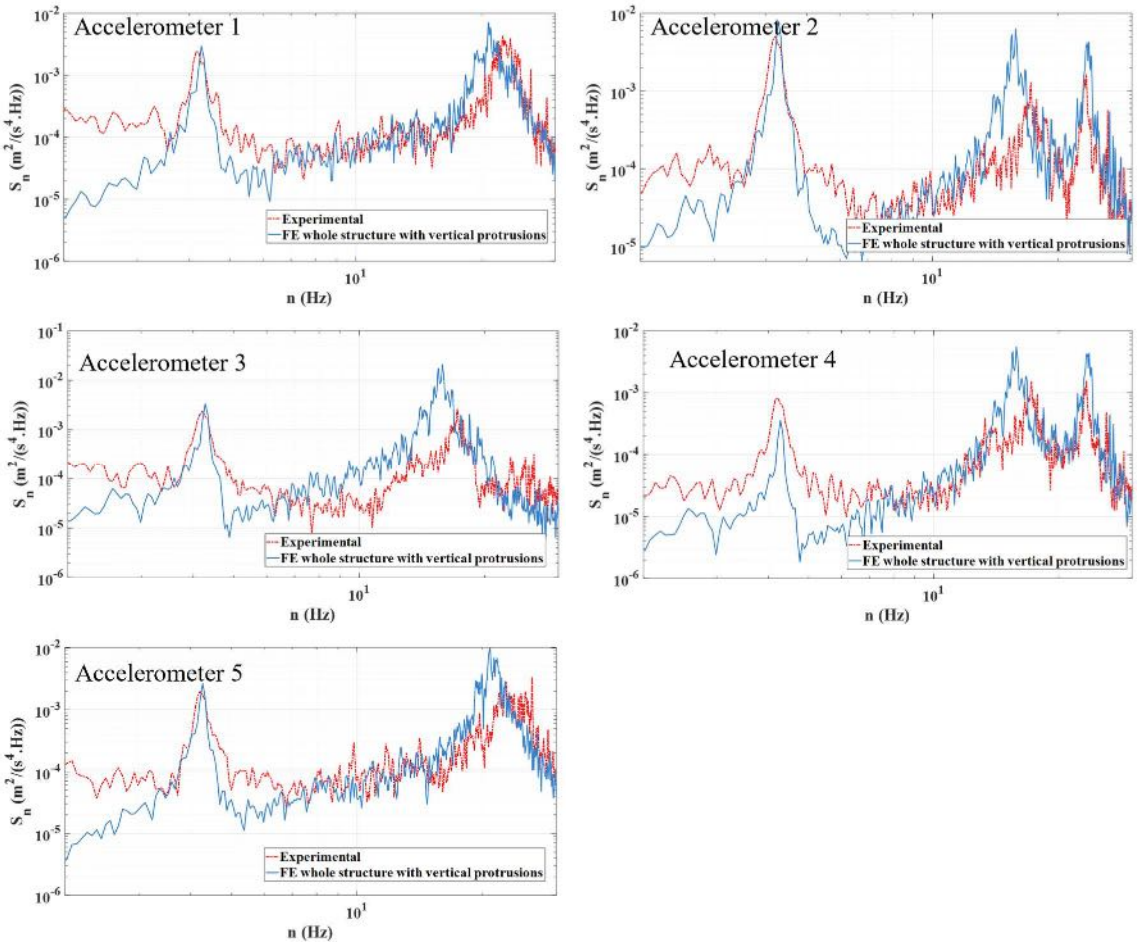

Figure 2.34. Acceleration PSDs of the whole structure model with vertical protrusions compared to the experimental response for 22.35 m/s and 0° wind.

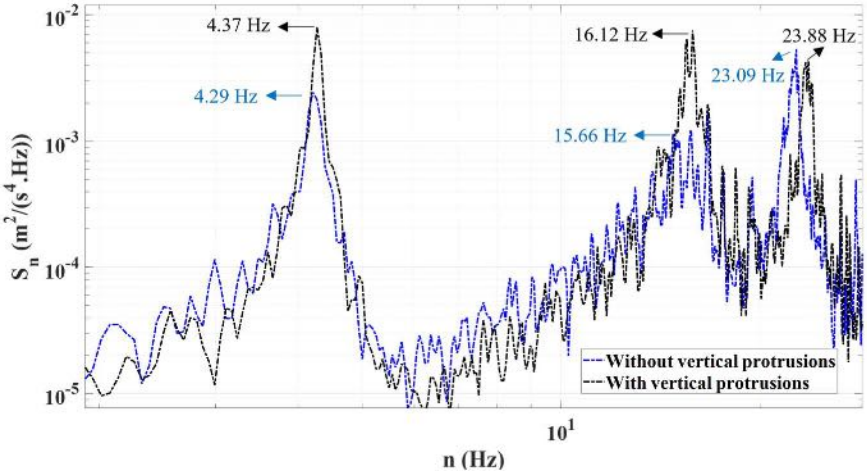

Figure 2.35. FE acceleration PSDs with and without vertical protrusions at location #2, for 22.35 m/s and 0° wind.

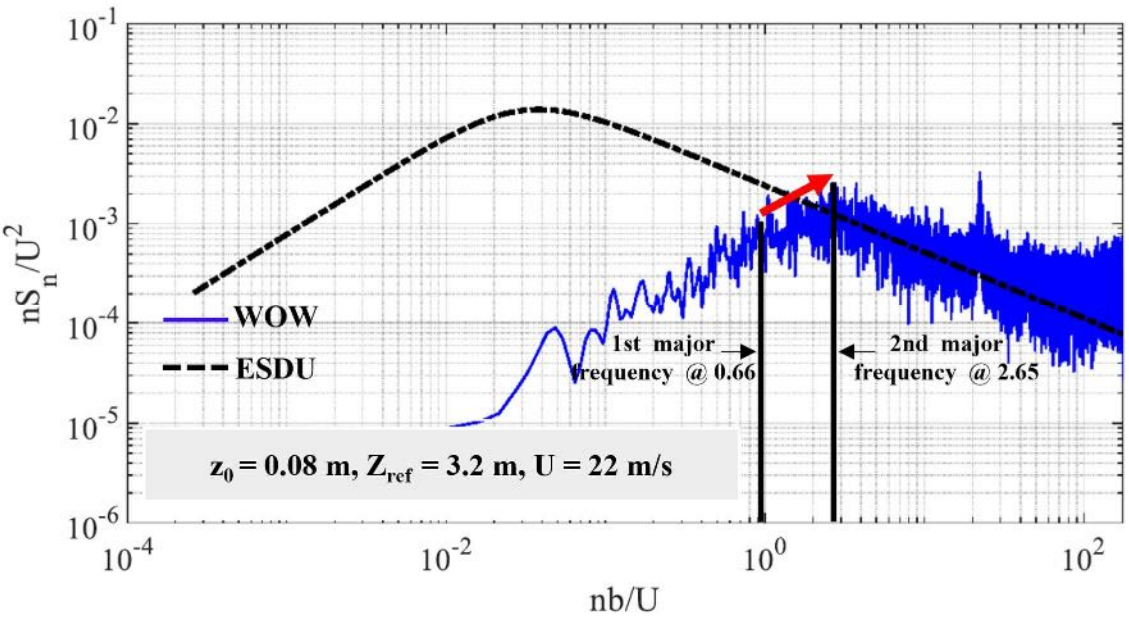

Figure 2.36. Normalized experimental power spectral density function, modified/expanded after Alawode et al. (2023)

2.5 Concluding remarks

Wind-induced dynamic performance of a single-skin curtainwall system is numerically and experimentally investigated in this study. The finite element (FE) modeling and analysis are built upon the measured dynamic response of the curtainwall from a series of full-scale wind tunnel tests conducted on a single-skin curtainwall mounted on a host building structure. The tests are carried out for wind speeds of 22.35 m/s, 31.30 m/s, and 40.23 m/s. Utilizing a turntable enables considering various wind directions for the dynamic tests. Two different FE modeling approaches are conducted. In the first approach, the whole structure including the supporting steel structure, curtainwall, and other components of the building is modeled to replicate the experimental setup. In the second approach, the façade is numerically modeled as a stand-alone system, while the corresponding boundary conditions are applied to it. The FE models are subjected to nodal time history loads based

on C_p time histories measured in the wind tunnel tests. The numerical models are calibrated to reproduce acceleration and strain responses of the actual curtainwall specimen for a 22.35 m/s and 0° wind loading. The calibrated whole structure FE model is then validated to reproduce other wind-tunnel testing cases for different wind speeds and wind directions to match the experimental dynamic response. It is observed that the calibrated FE model is validated with sufficient accuracy and can be used as a predictive tool for further studies. Analyzing the power spectral densities of the acceleration response shows that the stand-alone façade-only FE model misses the first major frequency at 4Hz, while the whole structure FE model accurately captures it. Applying a system identification method also shows that the 4 Hz frequency originated from the interaction of the façade and its supporting structure. In addition, the wind-induced response is likely overestimated by the façade-only FE model, as it does not account for the energy consumed for the deformation or excitation of the supporting structure. This result suggests that the façade would perform differently depending on the structure it is mounted to and the interaction between the façade and building should be properly modeled to realistically capture the wind-induced dynamic behavior of façade systems. Lastly, the dynamic effects of vertical protrusions on the wind-induced response of the façade are also investigated, which indicates the installation of protrusions may increase the wind-induced dynamic response of the façade due to the increase in the system's overall stiffness, which may cause a higher probability of water ingress. Based on the dynamic response of the curtainwall, major resonant frequencies are observed higher than 1 Hz. Therefore, it may be beneficial to revisit the ASCE 7 provisions regarding the analysis and design of components and claddings, as it

does not take into account wind-induced dynamic effects for structures with a frequency greater than 1 Hz.

CHAPTER 3 . NUMERICAL INVESTIGATION OF THE DYNAMIC RESPONSE OF OPERABLE WINDOW SYSTEMS TO WIND-INDUCED VIBRATIONS

3.1. Introduction

The operable window systems are enclosure components integrated into curtainwall panels in most high-rise buildings' envelope systems for openings, which are particularly prone to potential failures caused by excessive vibrations during windstorms. Wind-induced vibrations generated from extreme wind gusts are observed to be the 2nd main cause of the failure of operable window systems after wind-borne debris, due to consequential damage to their frames and connections. These failures observed as the whole window panel's falling off due to panel disengagement, can occur frequently after only a few years of the service life (FEMA 339, 1999; FEMA P-672, 2009; Horst et al., 2012; Mosqueda et al., 2007; Qin et al., 2023; Suaris & Khan, 1995). The WIV-related failure of the window system is a significant contributor to the generation of wind-borne debris too, posing a grave risk to the surrounding buildings and infrastructure. However, the research focus has been mostly given to the impact resistance of the window systems against wind-borne debris than the risk of wind-induced vibration of the operable parts. Consequently, there is a significant gap in knowledge within the wind engineering community regarding the effect of wind-induced vibrations on the dynamic performance of the curtainwall and in particular the operable window systems.

While the ASCE 7 (2016) standard specifies the necessity of dynamic analysis to estimate the wind effects on structures, it does not pose a requirement for structures with natural frequencies beyond 1 Hz to be analyzed for wind-induced dynamic effects. This criterion

can be misleading because it was originally developed with the vibration of the whole building in mind, so it may not be applicable to the building envelope components which have higher frequencies than 1 Hz. This puts a misleading impression that the curtainwall window systems and the operable window systems do not fail by wind-induced dynamic effects, making the C&C still vulnerable to wind actions. The wind tunnel test results clearly showed significant damage related to C&C including roofing systems, windows, and curtainwall systems with frequencies higher than 1 Hz. Research conducted in wind tunnels on standing seam metal roofs indicated the occurrence of a significant resonant vibration induced by the wind in the frequency range of 8 Hz to 14 Hz (Azzi et al., 2020; Habte et al., 2015). A full-scale wind tunnel test of a single-skin façade curtainwall evidenced major frequencies at around 4 Hz, 16 Hz, and 24 Hz (Vutukuru et al., 2021). Previous studies on the performance of curtainwall window mock-ups through experimental testing have been mostly conducted using static pressure tests (Bedon et al., 2018, 2019; Ilter et al., 2015; Naqash et al., 2021; Yalaz et al., 2018). Moreover, the existing procedures by established standards such as ASTM E330/E330M (2014), and ASTM E1886 (2013) to evaluate wind-induced stresses are limited to static uniform or cyclic pressure. However, these simplified methods cannot capture the inherent dynamic effects of random wind loading and the spatial and temporal variation due to turbulence, and therefore, are not able to realistically consider the wind-induced vibrations in the curtainwall window and the operable parts. For example, through a series of realistic wind tunnel tests, it was observed that the standing seam metal roof failure mode is the clip rupture, rather than the clip slippage which is frequently seen in conventional static pressure testing (Habte et al., 2015). Moreover, parts and connections of the operable

window systems such as metal hardware, specifically in the open condition, are prone to fatigue failure during wind events. However, in the façade industry, the performance of the operable window systems has been estimated using simple fatigue experiments using open-close cyclic testing.

This chapter attempts to address the existing gaps in understanding the effects of wind-induced vibrations on the dynamic performance of operable window systems, as an integral part of glass curtainwall systems. A high-fidelity finite element (FE) model is developed, calibrated, and validated based on the experimental data obtained from conducted full-scale wind tunnel tests on an operable window system integrated into a single-skin façade unitized curtainwall system. The wind tunnel tests are conducted at the Wall of Wind Experimental Facility (WOW EF) at Florida International University. The developed finite element model is subsequently used to assess the dynamic response of the operable window system due to the wind-induced vibrations, in closed and open service conditions of the window. Time history finite element analyses are carried out for various wind-loading scenarios, i.e., different wind speeds and wind directions. In the FE modeling and analysis, the whole building structure, including the supporting steel structure, curtainwall, and the integrated operable window are considered.

3.2. Wind tunnel tests

3.2.1. Experimental setup and configuration

A series of wind tunnel experiments are conducted at the Wall of Wind (WOW) Experimental Facility (EF) to systematically investigate the wind effects on the operable parts in a curtain wall system. The WOW EF is located at the Florida International

University, which is one of the Natural Hazards Engineering Research Infrastructure (NHERI) EFs designated by the National Science Foundation (NSF). This facility is unique with an open jet ABL wind tunnel comprised of a 2 × 6 array of 6-foot-tall fans, capable of generating hurricane intensity levels up to Category 5 (based on the Saffir-Simpson scale), which facilitates testing large-scale models up to wind speed of 70 m/s (156 mph). The ABL profile is produced using triangular spires located near the fans, while automated square-shaped roughness elements with various angles, roughness lengths, and scales are utilized to generate the desired turbulence intensity and roughness length (Chowdhury et al., 2017, 2018). A circular rotating table (turntable), with a diameter of 4.9 m is located 4.3 m downwind of the flow management box, enabling testing the specimen for different wind directions. Figure 3.1a shows the turntable in front of the flow management box and Figure 3.1b shows a closer view of the flow management box, including the triangular spires for producing the desired ABL.

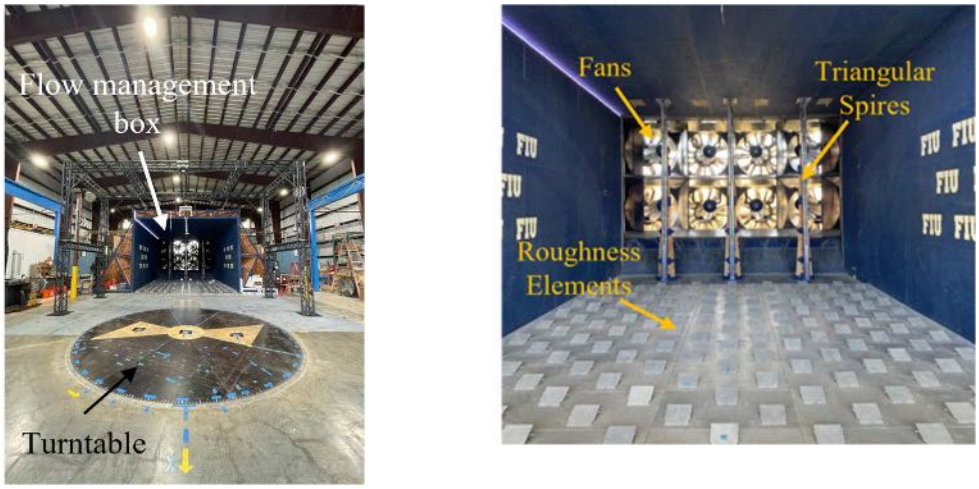

(a) (b)

Figure 3.1. (a) Inside the FIU Wall of Wind (WOW) Experimental Facility (EF), (b) The flow management box with roughness elements and spires for generating the desired ABL

The tested single-skin curtainwall model constructed for this study consists of 3 double-glazed façade units including a center panel and two side panels as shown in Figure 3.2 with an operable window component in the center. The overall dimensions of the curtainwall panels and the operable window are shown in the figure. The operable window is 1.87 m in height and 0.6 m in width in size. The curtainwall is comprised of 5 joints, which are denoted by 'J#'. The façade's glass is a double-glazing unit that is comprised of an outer monolithic and an inner laminated glass pane that is composed of a polyvinyl butyral (PVB) layer locked in between the two panes. The curtainwall is mounted to a rectangular 3.05 m (height) × 3.65 m (width) × 1.80 m (depth) supporting steel structure which is bolted to the turntable as shown in Figure 3.3.

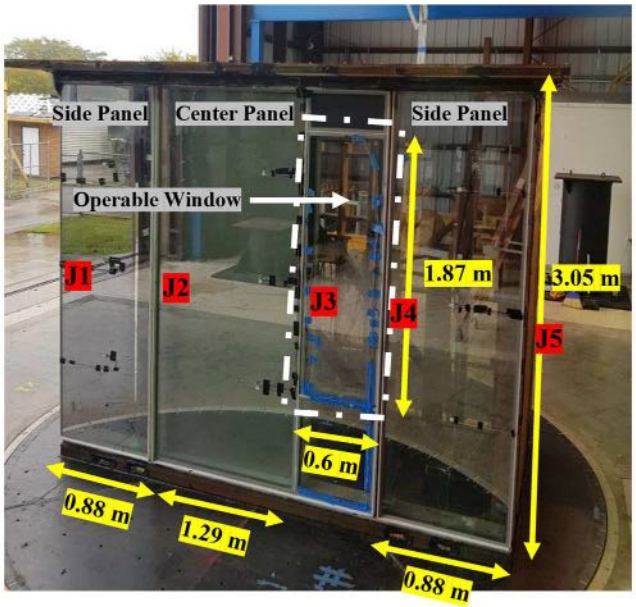

Figure 3.2. Single-skin façade curtainwall on the turntable (front view)

Figure 3.3. Supporting steel structure

The operable window system considered in this study is an extender top hung type, i.e., vertically opening or awning type (in contrast with the side hung type or casement type, which opens horizontally). Figure 3.4 indicates a detailed anatomy of the operable window system. As shown in Figure 3.4 a, there are three different layers of connections in the operable window system, which are labeled with numbers (1), (2), and (3). The connection layer (1) is the structural silicone which is the connection between the window glazing and

the sash. The structural silicone provides sufficient translational and rotational stiffness between the glazing and the sash.

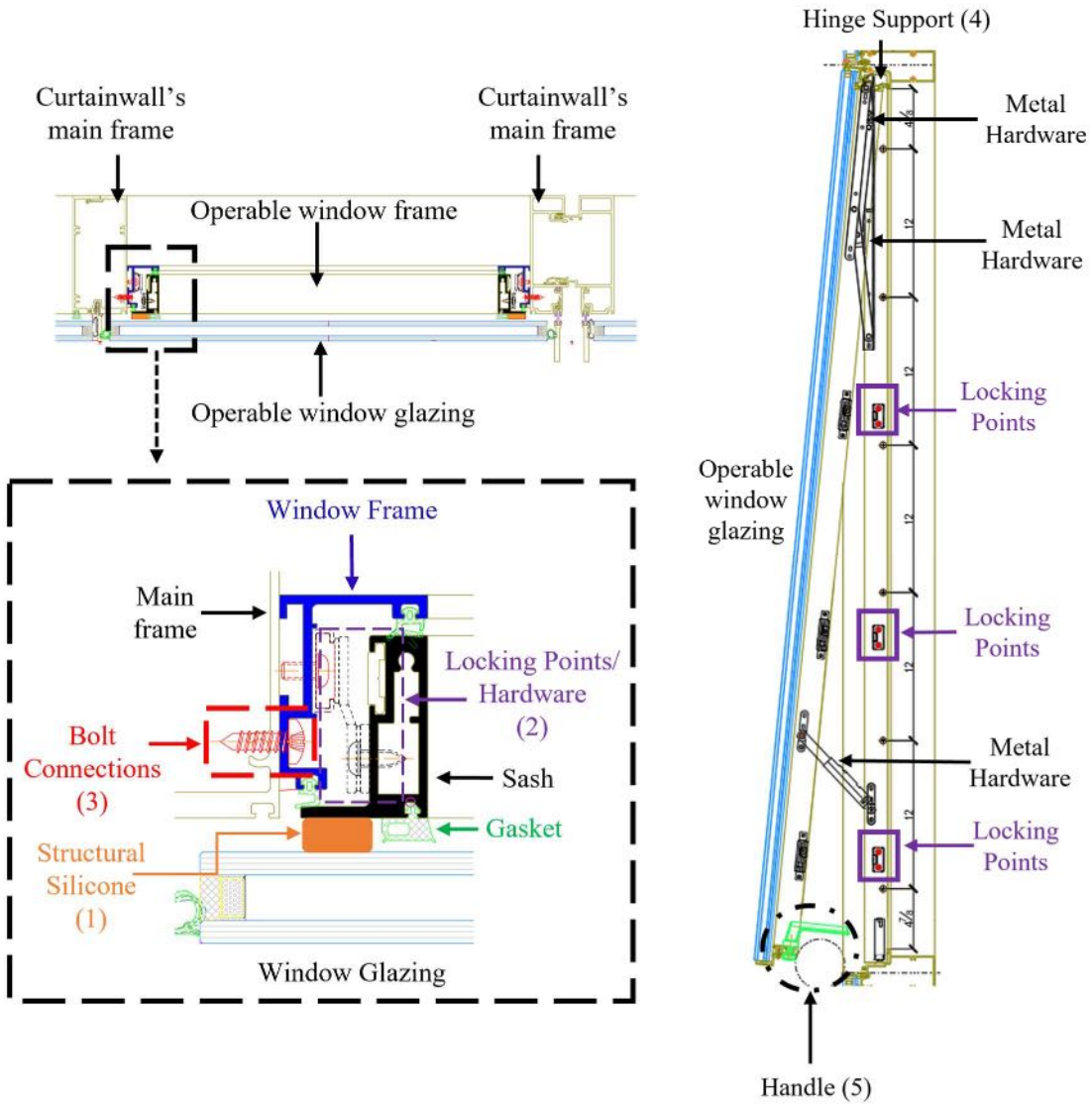

(a) (b)

Figure 3.4. Anatomy of the operable window system, connections between the window frame, sash frame, and the curtainwall: (a) horizontal cross-section, and (b) vertical cross-section.

The connection layer (2) is between the window frame and the sash. These connections are provided by a series of metal locking points and a handle lock in the closed condition of

the window as shown in the figure. However, in the open condition of the window, these locking points and the handle lock are not involved, and the connection between the window frame and the sash frame is only provided by the metal hardware and the hinge at the top as shown in Figure 3.4b. The vertical cross-section clearly shows the location of the locking points, the handle (lock), and the metal hardware along the height of the operable window system. The connection layer (3) is between the window frame and the main frame. The window frame is bolt-connected to the curtainwall's main aluminum frame, as indicated in Figure 3.4a.

3.2.2. Instrumentation

During the tests, pressures, accelerations, and strains are measured in the wind tunnel experiment. A polycarbonate panel having the same geometry as the glass window of the operable part is used in place of the original glass for the pressure testing, for which the polycarbonate glass is with drilled holes to mount the pressure taps since they cannot be drilled into the glazing side, as shown in Figure 3.5. Figure 3.6 shows the schematic and the actual layout of the pressure taps instrumented on the polycarbonate window. Accelerometers and strain gauges are installed at multiple locations of the operable window system. Three accelerometers are installed at the glass surface of the operable window system to measure the out-of-plane acceleration, while eight tri-axial strain gauges are installed at the aluminum window frame. Figure 3.7a and b show the locations where the accelerometers and strain gauges are instrumented, respectively. In the open condition testing phase, two additional accelerometers and three additional uniaxial strain gauges (along the long axis of hardware) are installed on the connection hardware to observe the dynamic response, as indicated in Figure 3.8 respectively.

Figure 3.5. Polycarbonate panels and window on the rear side

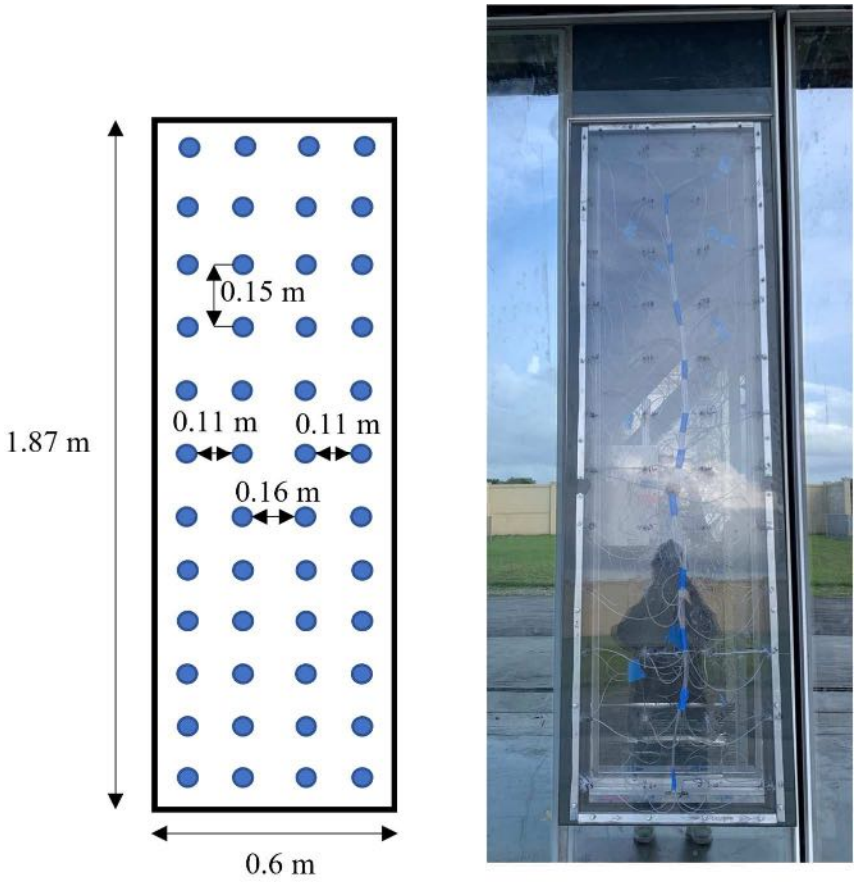

Figure 3.6. Schematic layout of the pressure taps on the polycarbonate side of the operable window system (rear side of the curtainwall)

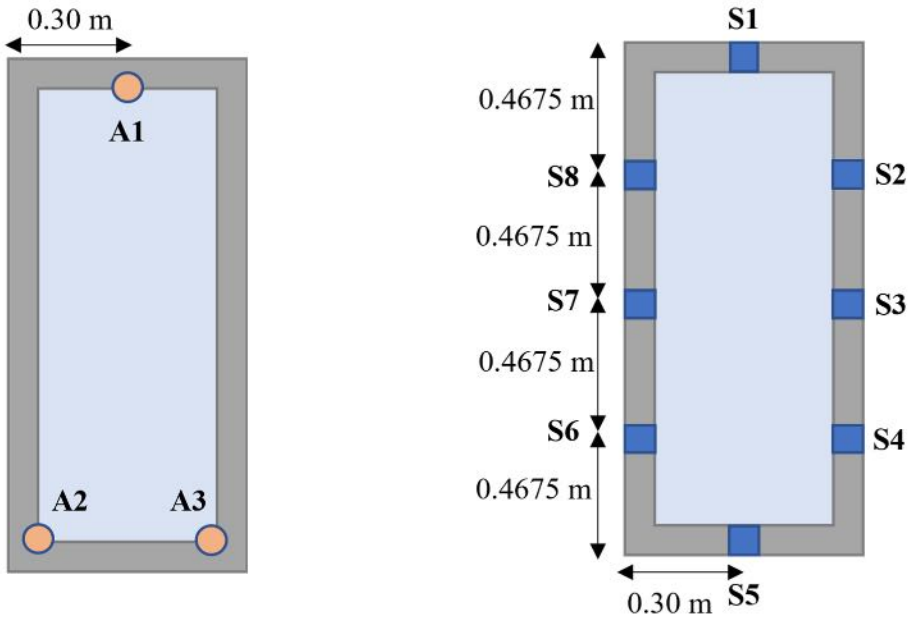

(a) (b)

Figure 3.7. Locations of the (a) accelerometers instrumented on the glass window, and (b) strain gauges instrumented on the aluminum frame of the window.

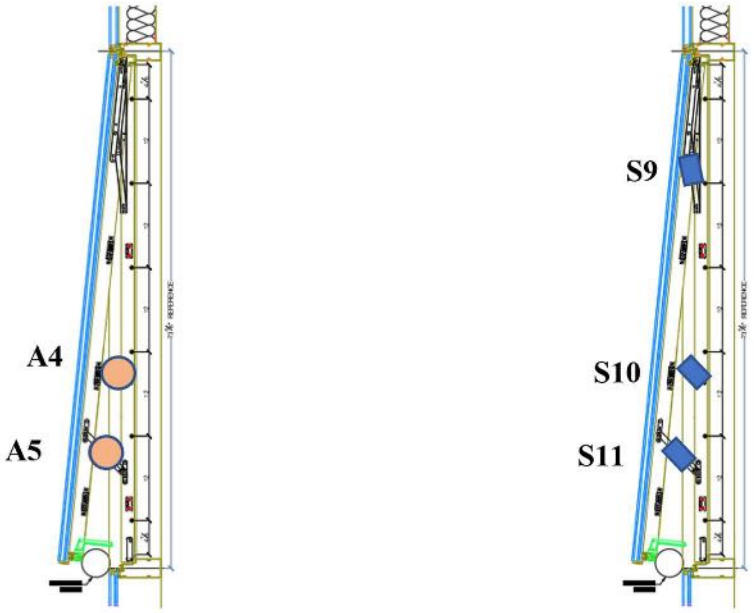

(a) (b)

Figure 3.8. Locations of the additional (a) accelerometers on the hardware connections, and (b) strain gauges on the hardware connections in the open condition.

3.2.3. Testing protocol

As described, to study the wind-induced vibrations of the awning-type operable window system, the conducted wind-tunnel tests include closed-condition and open-condition phases. In the closed-condition phase, the closed operable window system is subjected to wind speeds ranging from 35.76 m/s (80 mph) to 44.7 m/s (100 mph) with 4.5 m/s (10 mph) increments. For each wind speed, different wind directions starting from 0° (windward direction) to 315° with 45° increments are tested. The open condition phase of testing is conducted for wind speeds starting from 22.3 m/s (50 mph) to 31.3 m/s (70 mph) with 4.5 m/s (10 mph) increments. Lower wind speeds are considered for the open condition in comparison with the closed condition since the metal hardware connections are assumed to be prone to failure at higher wind speeds. For each wind speed, different wind directions ranging from 0° to 315° with 45° increments, including finer increments of 10° for critical angles (60° to 120° and 240° to 300°) are considered. Table 3.1 summarizes the test protocol for open and closed condition phases of wind-tunnel testing. Further details can be found in the study conducted by Vutukuru (2021). The definition of the wind direction is as Figure 2.7.

Table 3.1. Testing protocol

Test Phase	Wind Speed (m/s)	Wind Direction θ (degree)	Test Duration (minutes)
Open Condition	22.3 (50 mph)	0, 45, 60, 70, 80, 90, 100, 110, 120, 135, 180, 225, 240, 250, 260, 270, 280, 290, 300, 315	10
Open Condition	26.8 (60 mph)	0, 45, 60, 70, 80, 90, 100, 110, 120, 135, 180, 225, 240, 250, 260, 270, 280, 290, 300, 315	10
Open Condition	31.30 (70 mph)	0, 45, 60, 70, 80, 90, 100, 110, 120, 135, 180, 225, 240, 250, 260, 270, 280, 290, 300, 315	10
Closed Condition	35.8 (80 mph)	0 to 315 (in 45-degree increments)	10
Closed Condition	40.23 (90 mph)	0 to 315 (in 45-degree increments)	10
Closed Condition	44.7 (100 mph)	0 to 315 (in 45-degree increments)	10

3.3. Numerical modeling and calibration

In this study, a finite element (FE) model is created to replicate wind-induced vibrations observed in full-scale wind-tunnel tests at the WOW EF, with the aim of evaluating the dynamic performance of the system under different loads. The FE models for the operable window, single-skin curtainwall, and the entire structure housing the curtainwall are developed sequentially. Midas Gen FEA software (2021) is applied for finite element modeling, eigen, and time history analyses. This section provides a description of the sequential steps involved in the finite element modeling process. Additionally, it presents the procedure and results of calibrating the finite element model of the operable window system.

3.3.1. FE modeling of the operable window system

The finite element (FE) analysis of the operable window system is carried out for both the closed and open configurations of the window. Figure 3.9 shows the FE models developed for each case, which consist of glazing, aluminum sash frame, and aluminum window frame. These three components are interconnected in sequence, from connection layer (1) to connection layer (3), using structural silicone, locking points (in the closed condition), or metal hardware (in the open condition), and finally bolt connections, as depicted in Figure 3.4.

Figure 3.10 indicates the finite element (FE) modeled window frame and sash frame, along with their respective cross-section profiles. The mullion and transom elements are modeled using 12-degrees-of-freedom 2-node beam elements, based on the CAD drawings. The cross-sectional properties of the modeled window and sash frames are presented in Table 3.2.

For FE modeling the operable window system's glazing, 4-node thin plate elements are used in the software as shown in Figure 3.9. The operable window system utilizes a double-glazing unit (DGU), as depicted in Figure 2.12. The DGU consists of inner and outer glass panes separated by a gap using a thermal spacer. The inner pane is a laminated glass with three layers, comprising two layers of monolithic glass bonded with a polyvinyl butyral (PVB) interlayer. However, numerical modeling of insulated laminated glass presents complexities and challenges. To mitigate the modeling complexity of the DGU, the authors employ an innovative approach. The approach employed entails determining an equivalent monolithic glass with a thickness that represents the properties of the DGU and produces

comparable dynamic behaviors as the actual DGU. Table 2.3 displays the outcomes of this method, exhibiting both the calculated equivalent thickness and the actual thickness of the inner and outer glasses. The equivalent thickness approach comprises two phases. The first phase involves estimating the effective thickness of the laminated glass, specifically the inner glass, using the method developed by Galuppi and Royer-Carfagni (2012). The resulting effective thickness values are presented in the 6th column of Table 2.3. Afterward, the authors adopt the approach outlined in Annex C of the Eurocode prEN 16612 (2015) to back-calculate the overall effective stiffness of the DGU and its equivalent thickness. The 7th column of the table indicates the thickness ratio R used to compare the final calculated equivalent thickness with the actual thickness of the DGU. The results show that the estimated equivalent thickness is less than the actual thickness of the DGU. To accurately replicate the original DGU's dynamic behavior, the unit weight of the equivalent glass is increased to compensate for the lost mass. Ultimately, the obtained equivalent thickness values are applied to model the glazing of the operable window system using 4-node thin plate elements.

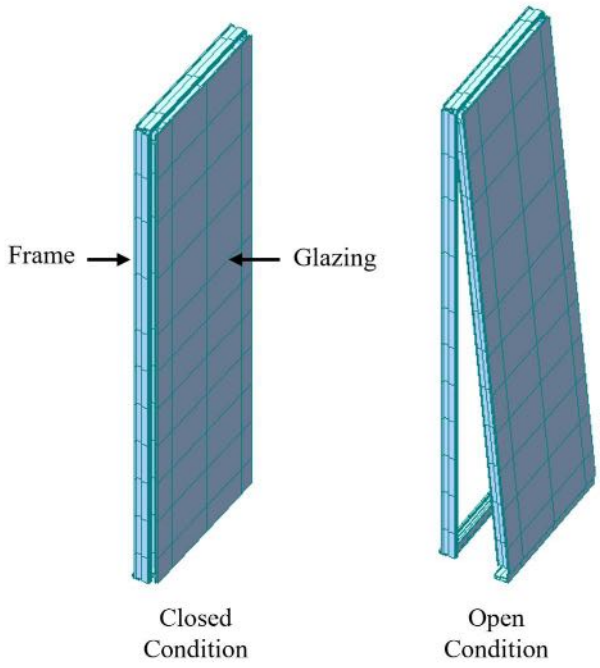

Figure 3.9. The developed FE models of the operable window system

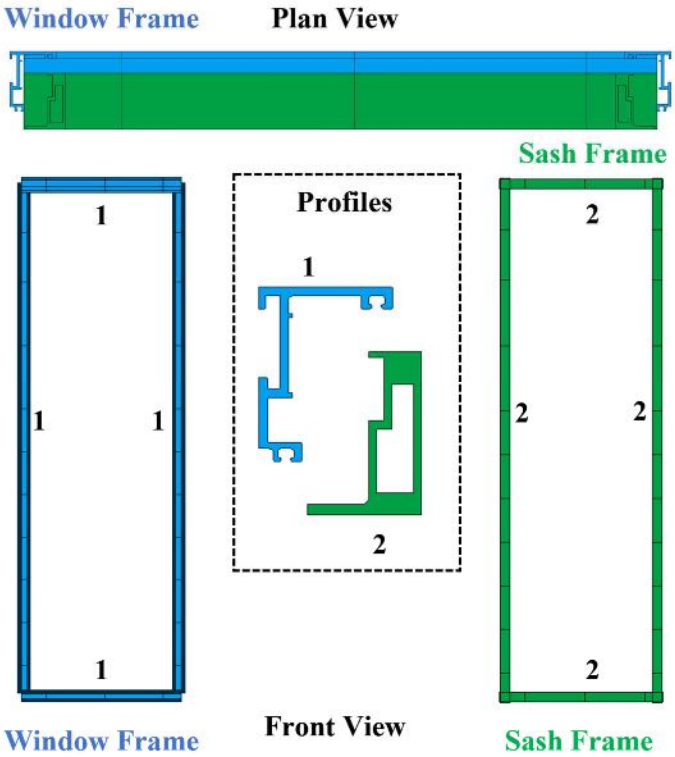

Figure 3.10. The layout of the profiles of the modeled operable window frame and the cross sections of the two framing profiles

Table 3.2. Cross-sectional properties of the operable window framing profiles

	Framing Profile	Area (mm^2)	I_{XX} (mm^4)	I_{YY} (mm^4)	I_{XY} (mm^4)
1	Window Frame	325	1.12e5	4.60e4	7.44e3
2	Sash Frame	473	1.55e5	3.10e4	3.06e4

The subsequent critical stages in the finite element (FE) modeling of the operable window system encompass the representation of the three layers of sequential connections among the glazing, sash, window frame, and curtainwall system. To simulate the connection layer (1), specifically the structural silicone that adheres the glazing of the operable window to the sash frame, elastic links are employed in the software. These elastic links possess 6 degrees of freedom (DOFs) each, encompassing translational and rotational stiffness in all local x-, y-, and z-directions. Details of the utilized elastic links can be found in the Midas Gen user manual (2020). Figure 3.11 showcases the modeled operable window system, wherein the elastic links are employed to assemble the glass and frames.

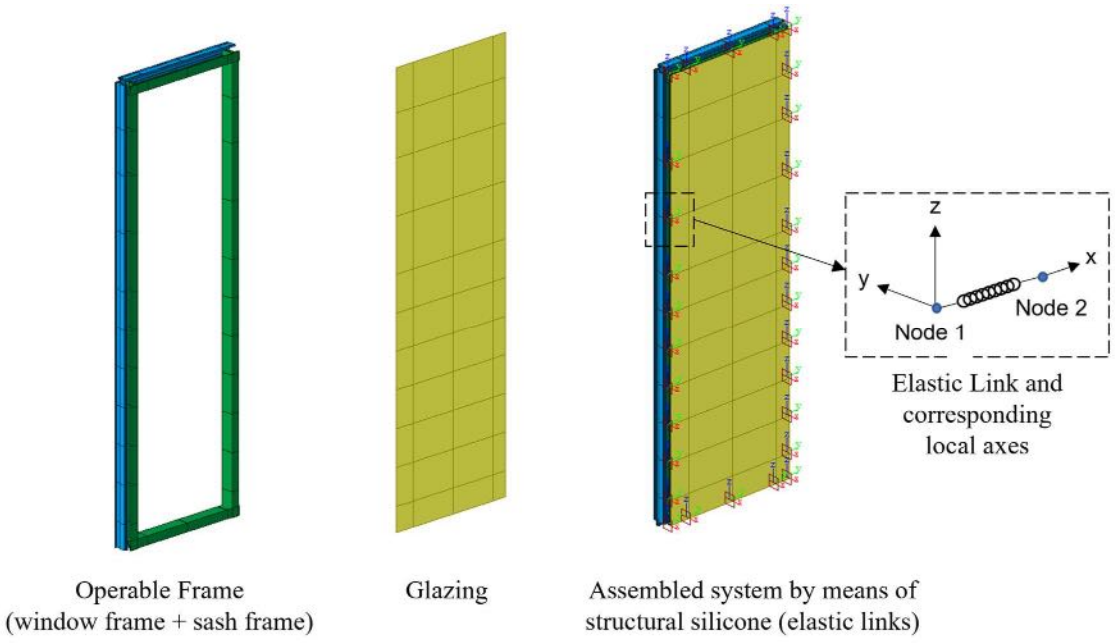

Figure 3.11. Modeled operable window system with glass and frames assembled using elastic links (shown with the local axes).

The next step in FE modeling is the inclusion of the connection layer (2), which refers to the joints between the sash frame and the window frame. These connections consist of locking points and a handle when the window is in a closed position, as depicted in Figure 3.4. However, when the window is open, the locking points and handle are not involved, and the connection between the window frame and the sash frame is facilitated by metal hardware, as shown in Figure 3.4. In the closed condition, the locking points, the handle, and hinge supports are modeled using 6-degrees-of-freedom elastic links, with assigned translational and rotational stiffness values. Similarly, for the open condition, 6-degrees-of-freedom elastic links are applied to model the metal hardware. Figure 3.12 and Figure 3.13 show the FE modeling of connection (2) of the operable window system in closed and open conditions, respectively.

The final layer of connections in the FE modeling involves connection layer (3), which pertains to the bolt connections used to attach the window frame to the main frame of the curtainwall, as shown in Figure 3.4. These connections are also modeled using 6-degrees-of-freedom elastic links with their corresponding translational and rotational stiffness values. Figure 3.14 provides a visual representation of how the bolt connections, i.e., connection (3), are modeled in the FE modeling of the operable window system.

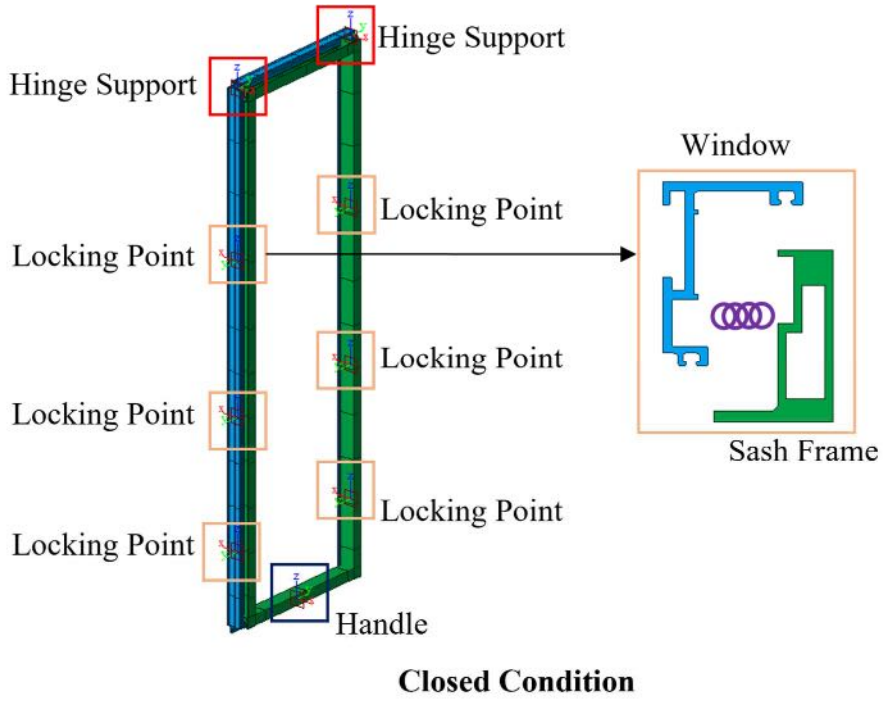

Figure 3.12. 6-degrees-of freedom elastic links applied for modeling the locking points, and handle, i.e., connection (2) in closed condition

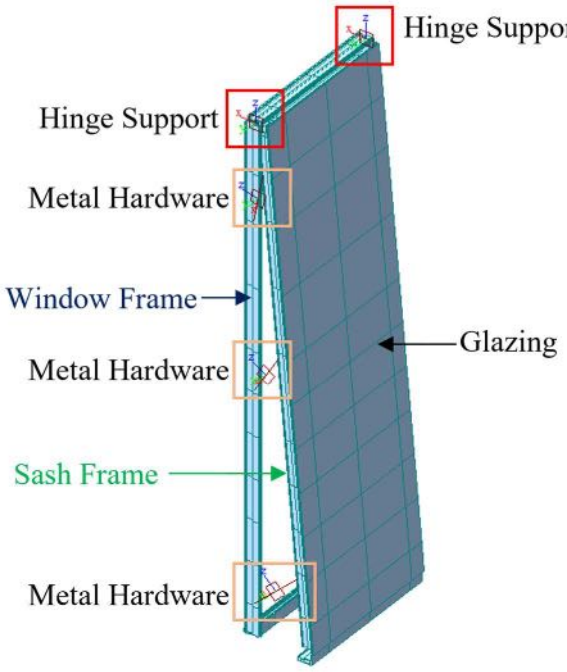

Figure 3.13. 6-degrees-of freedom elastic links used for modeling the metal hardware, i.e., connection (2) in open condition

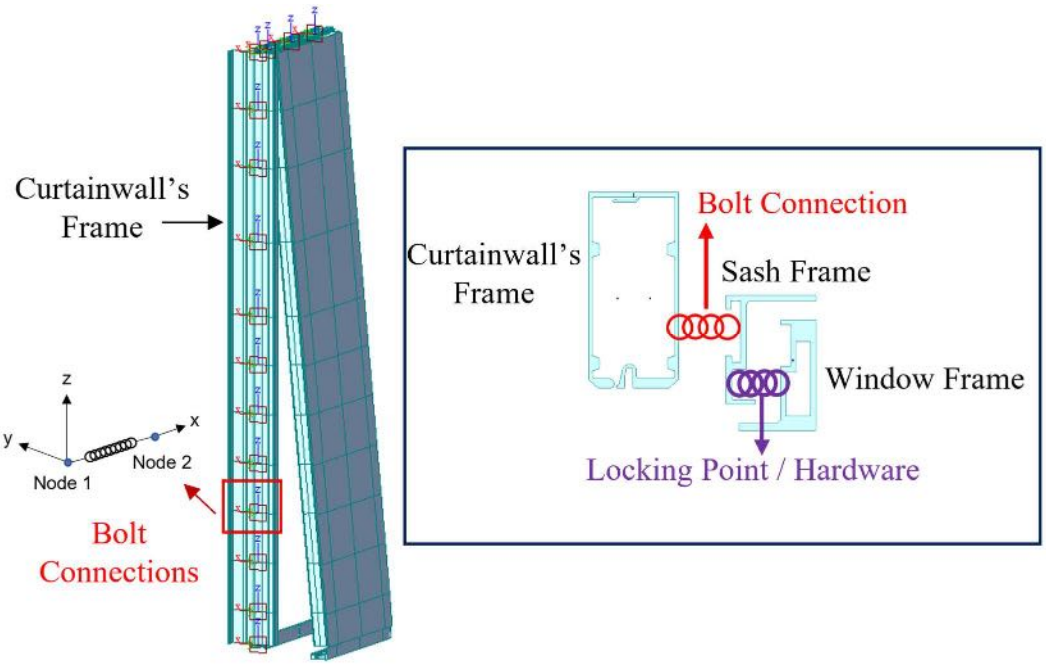

Figure 3.14. 6-degrees-of freedom elastic links utilized for modeling bolt connections (between the window frame and the curtainwall's main frame)

The operable window system is situated in the specified location on the main frame, as shown in Figure 3.15.

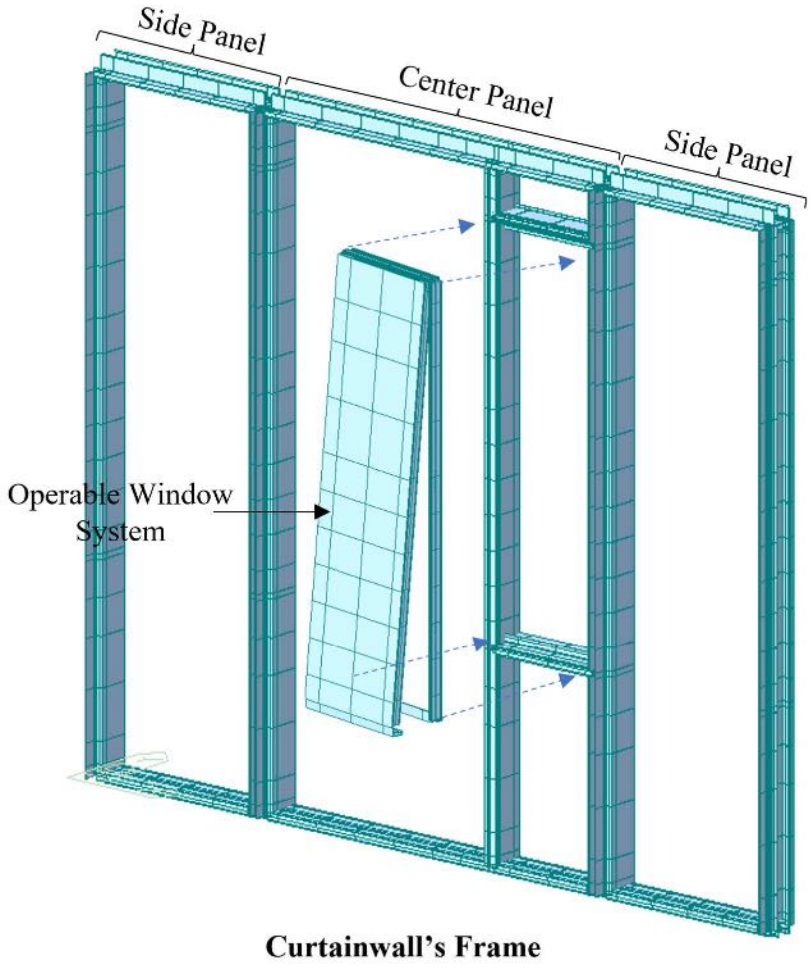

Figure 3.15. The modeled main frame (mullions and transoms) and sash frame for the operable part: (a) The frames are modeled using beam elements; (b) 3D Rendering with framing profiles.

3.3.2. Calibration (closed condition)

The pressure coefficient (C_p) time history data obtained from the experiment is converted to pressure time history data. The pressure time history data is consequently used to

produce nodal load time history by considering the corresponding tributary area of each node, which is used in Midas Gen finite element analysis (FEA) software (2021) to conduct corresponding dynamic time history analysis. Calibration involves an iterative process that adjusts the model parameters to achieve a numerical dynamic response that closely matches the experimental data. Calibration of the finite element (FE) model in the closed condition is considered achieved when the root mean square (RMS) acceleration response matches the experimental data within a 10% margin for all accelerometers, and the RMS of the strain response exhibits a difference of less than 20% compared to the experimental data for all strain gauges on the window frame. This criterion is chosen considering the limitation of the FE analysis in presenting the strain behavior at the extreme fiber, where the strain gauges are located in the experiment. In the FE analysis, the strain is measured from the beam element which cannot account for the specific placement of the strain gauges as used in the experiment. Table 3.3 summarizes the calibrated parameters in the closed condition of the operable window system.

Table 3.3. Internal parameters and their tuned values (Closed Condition of the window)

# in Figure 3.4	Model parameters	Axial stiffness (kN/m)	Shear stiffness (kN/m)	Rotational stiffness (kN·m/rad)
(1)	Structural silicone (Connection #1)	175.0	175.0	0.1
(2)	Locking connections between the sash and the window (Connection #2)	31.5	175.0	1.1
(3)	Bolt connections between the window and the curtainwall's main frame (Connection #3)	70.0	87.6	0.1
(4)	Hinge connections between the sash and the window	131.4	175.0	0.0
(5)	Handle connection	122.6	175.0	1.1

For the closed condition, the FE model is calibrated for the 40.23 m/s and 0° wind. Table 3.4 shows the acceleration response of the calibrated FE model, compared to the acceleration response of the specimen, subjected to 40.23 m/s and 0° wind, for all 3 accelerometers on the glazing of the operable window system. The results show a difference of 5.96, 1.64, and 4.23 percent between the RMS of acceleration time history response of the numerical and experimental response, for accelerometers 1, 2, and 3, respectively. Figure 3.16 shows the comparison of the acceleration response in the frequency domain, at locations #1, #2, and #3 (A1, A2, and A3 in Figure 3.7), where the power spectral density of the acceleration response of the FE model is plotted against the experimental response. It is indicated that the major frequencies in the acceleration response are captured by the calibrated FE model. The major frequency observed at 4.2 Hz, is captured by the calibrated FE model, for all the 3 accelerometers. The other major frequencies of 13.4 Hz and 16.8 Hz of the operable window system are captured by the numerical at 14.4 Hz, and 16.7 Hz, respectively.

Table 3.4. RMS of acceleration (m/s^2) time history of calibrated FE model in closed condition, compared to the experimental results for 40.23 m/s and 0° wind.

Accelerometer	Experimental acceleration time history RMS (m/s^2)	Finite element acceleration time history RMS (m/s^2)	Difference (%)
1	0.4743	0.4460	5.96
2	0.6698	0.6588	1.64
3	0.6064	0.5807	4.23

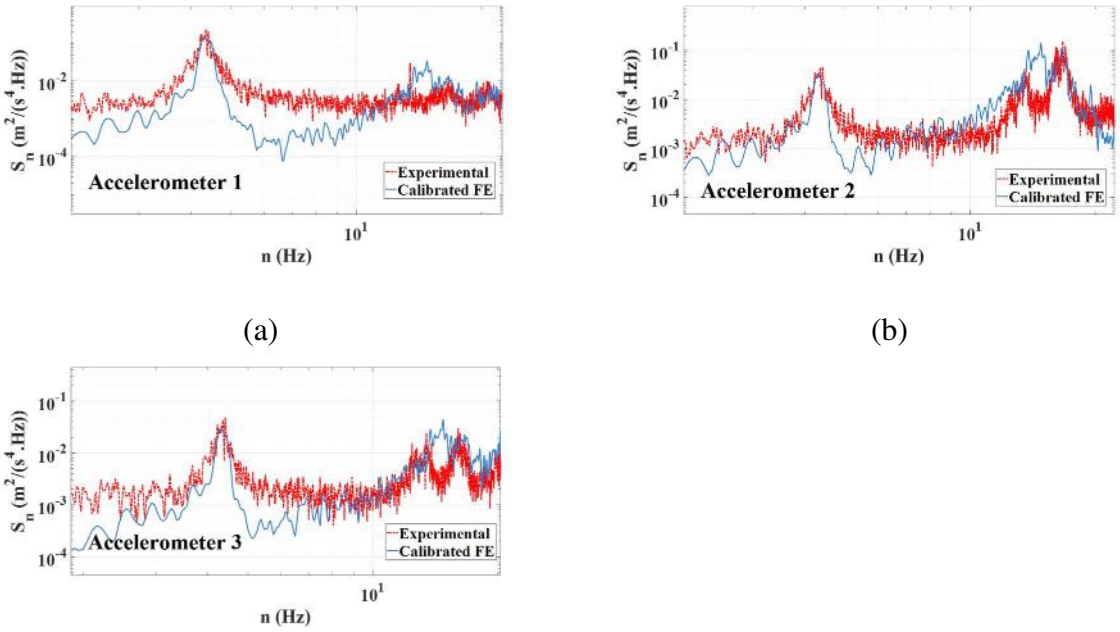

(a) (b)

(c)

Figure 3.16. The power spectral density acceleration response of the calibrated FE model in closed condition, at the accelerometer location #1 (A1), location #2 (A2), and location #3 (A3), compared to the experimental response for 40.23 m/s, and 0° wind.

In Figure 3.17, the root mean square (RMS) of the strain time history response obtained from the FE model is presented alongside the corresponding experimental data. The calibration criterion, which aims to achieve a difference of less than 20 percent, has been successfully met for all strain gauges.

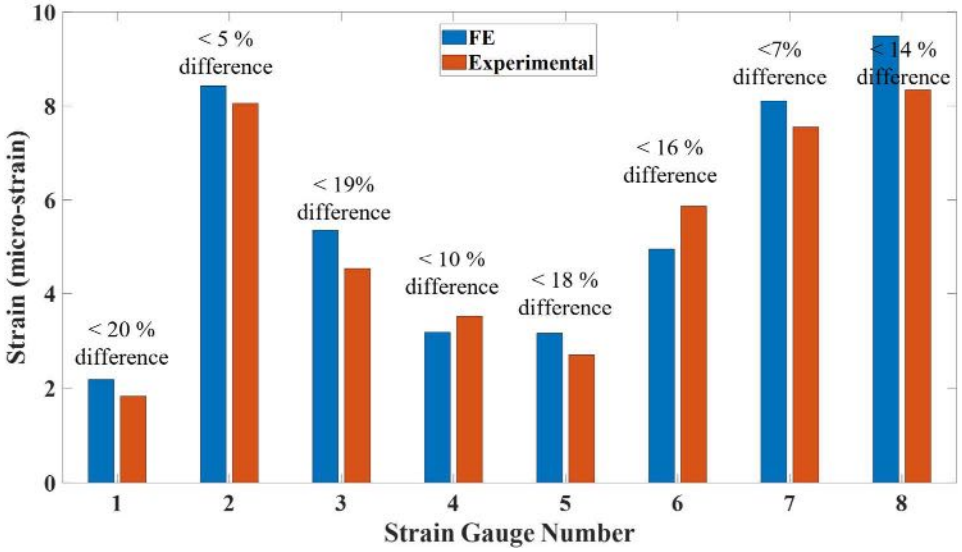

Figure 3.17. RMS of strain (micro-strain) time history of the calibrated FE model compared to experimental results for 40.23 m/s, and 0° wind.

3.3.3. Calibration (open condition)

The FE model is calibrated for 22.35 m/s wind speed and 0° wind direction in the open condition. Calibration of the finite element (FE) model in the open condition is considered successful when the RMS acceleration response matches the experimental data within a 10% margin for all accelerometers. Table 3.5 presents the internal parameters that are adjusted during this calibration process. Table 3.6 compares the acceleration response of the calibrated FE model with the experimental response of the specimen, which is subjected to 22.35 m/s wind speed and 0° wind direction, for all 3 accelerometers on the glazing of the operable window system, and the 2 additional accelerometers on the metal hardware. The results indicate that there is a difference of 6.99%, 6.91%, 8.89%, 7.39%, and 3.71% between the RMS of the acceleration time history response of the numerical and

experimental responses for accelerometers 1, 2, 3, 4, and 5, respectively. In Figure 3.18, the acceleration responses in the frequency domain at locations #1, #2, and #3 (A1, A2, and A3 in Figure 3.7) are compared, where the power spectral density of the acceleration response of the FE model is plotted against the experimental response. The comparison shows that the calibrated FE model captures the major frequencies in the acceleration response. Specifically, the calibrated FE model captures the major frequency of 4.2 Hz for all 3 accelerometers, and the other major frequencies of 13.7 Hz and 17.6 Hz of the operable window system are captured by the numerical model at 14.1 Hz and 16.7 Hz, respectively.

Table 3.5. Internal parameters and their tuned values (Open Condition of the window)

# in Figure 3.4	Model parameters	Axial stiffness (kN/m)	Shear stiffness (kN/m)	Rotational stiffness (kN·m/rad)
(1)	Structural silicone (Connection #1)	175.0	175.0	0.1
(2)	Metal hardware connections between the sash and the window (Connection #2)	85.0	85.0	0.1
(3)	Bolt connections between the window and the curtainwall's main frame (Connection #3)	70.0	87.6	1.1
(4)	Hinge connections between the sash and the window	78.8	175.0	0.0

Table 3.6. RMS of acceleration (m/s^2) time history of calibrated FE model in open condition, compared to the experimental results for 22.35 m/s and 0° wind.

Accelerometer	Experimental acceleration time history RMS (m/s^2)	Finite element acceleration time history RMS (m/s^2)	Difference (%)
1	0.1087	0.1163	6.99
2	0.2387	0.2552	6.91
3	0.2204	0.2008	8.89
4	0.2122	0.1965	7.39
5	0.1399	0.1347	3.71

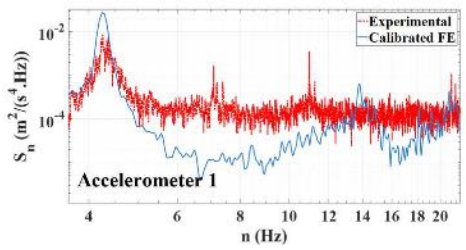

(a)

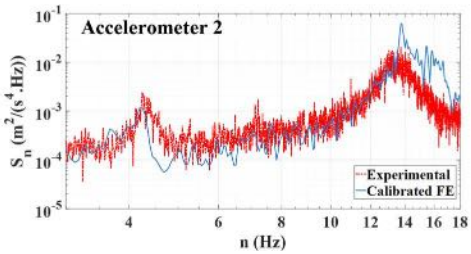

(b)

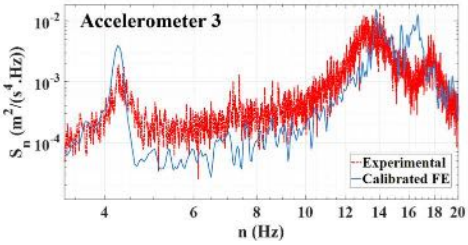

(c)

Figure 3.18. The power spectral density acceleration response of the calibrated FE model in open condition at the accelerometer location #1 (A1), location #2 (A2), and location #3 (A3), compared to the experimental response for 22.35 m/s, and 0° wind.

3.4. Numerical analysis results

3.4.1. Results of the closed condition

The calibrated finite element (FE) model, simulated in a closed condition with a wind speed of 40.23 m/s and wind direction of 0°, is employed to assess the dynamic responses of the

model. The model is subjected to varying wind loads, with wind speeds of 35.76 m/s and 44.70 m/s, and wind directions of 0°, and 90°. The same C_p values are utilized to estimate the input nodal load time histories for each specific wind direction but with different wind speeds.

Table 3.7 presents the validation findings for wind speed of 35.76 m/s and wind direction of 0°. The power spectral density (PSD) of accelerations at locations #1, #2, and #3 is depicted in Figure 3.19, illustrating a satisfactory concordance between the numerical analysis and experimental data.

The validation outcomes reveal that the acceleration responses are reasonably captured, particularly for higher wind speeds. In the reproduced wind-tunnel test at 44.70 m/s and 0°, as presented in Table 3.8, the acceleration response of the numerical model at locations #1, #2, and #3 exhibits a difference of less than 9 percent compared to the experimental response. The acceptable matching of responses in the frequency domain is evident, as observed in Figure 3.19.

Table 3.7. RMS of acceleration (m/s^2) time history of validated FE model in closed condition, compared to the experimental for 35.76 m/s and 0° wind.

Accelerometer	Experimental acceleration time history RMS (m/s^2)	Finite element acceleration time history RMS (m/s^2)	Difference (%)
1	0.3569	0.3660	2.55
2	0.3958	0.4307	8.82
3	0.3278	0.3510	7.07

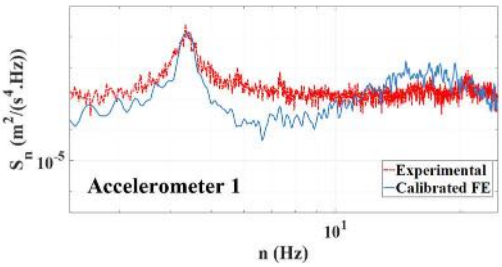

(a)

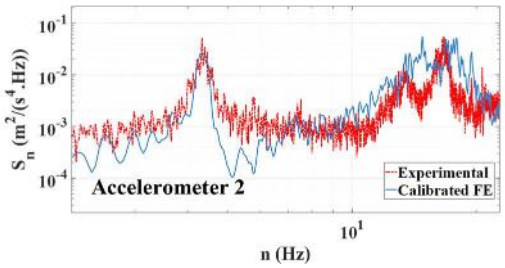

(b)

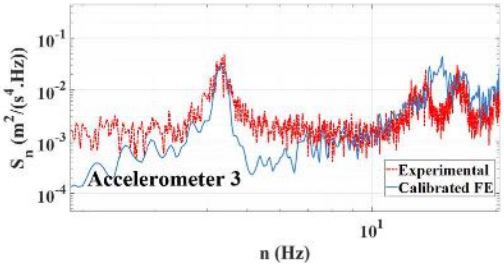

(c)

Figure 3.19. The power spectral density acceleration response of the validated FE model in closed condition at the accelerometer location #1 (A1), location #2 (A2), and location #3 (A3), compared to the experimental response for 35.76 m/s, and 0° wind.

Table 3.8. RMS of acceleration (m/s^2) time history of validated FE model in closed condition, compared to the experimental results for 44.70 m/s and 0° wind.

Accelerometer	Experimental acceleration time history RMS (m/s^2)	Finite element acceleration time history RMS (m/s^2)	Difference (%)
1	0.6933	0.6345	8.48
2	0.8267	0.7977	3.50
3	0.6922	0.7223	4.34

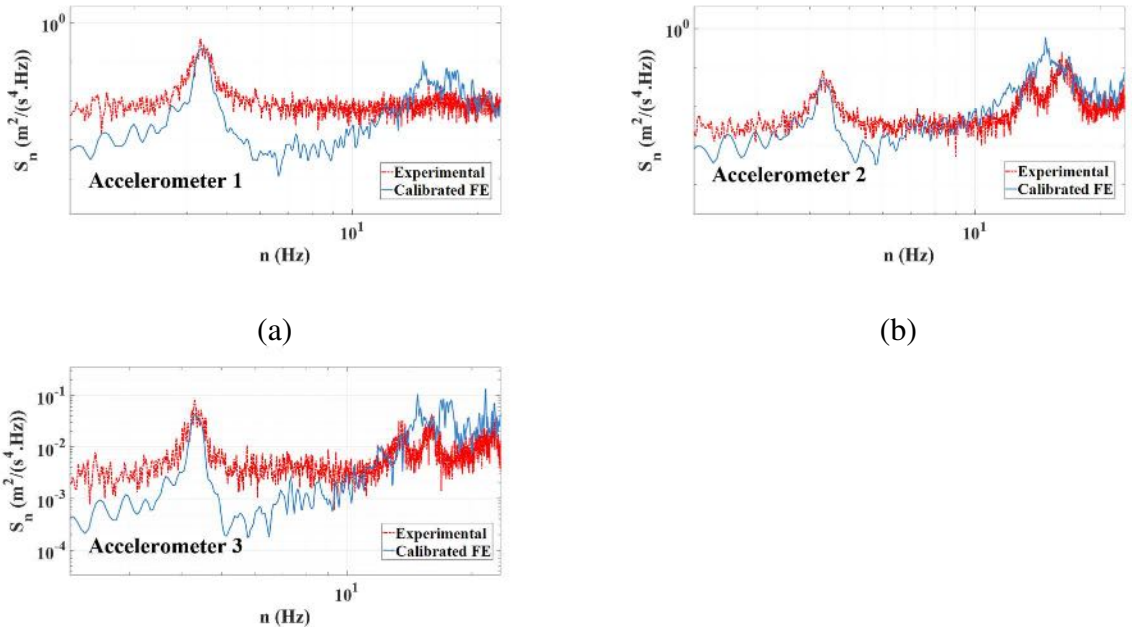

Figure 3.20. The power spectral density acceleration response of the validated FE model in closed condition at the accelerometer location #1 (A1), location #2 (A2), and location #3 (A3), compared to the experimental response for 44.70 m/s, and 0° wind.

Table 3.9 and Figure 3.21 show the analysis results for the 40.23 m/s wind speed and 90° direction. The FE analysis results show a difference of less than 15 percent for accelerometer #1, and less than 1 percent for accelerometers #2 and #3, regarding the RMS of acceleration time history. The results are acceptable for 90° wind direction regarding the fact that calibration has been conducted for 0° direction.

Table 3.9. RMS of acceleration (m/s^2) time history of validated FE model in closed condition, compared to the experimental results for 40.23 m/s and 90° wind.

Accelerometer	Experimental acceleration time history RMS (m/s^2)	Finite element acceleration time history RMS (m/s^2)	Difference (%)
1	1.0457	0.8851	14.89
2	0.9916	0.9821	0.96
3	0.9759	0.9751	0.08

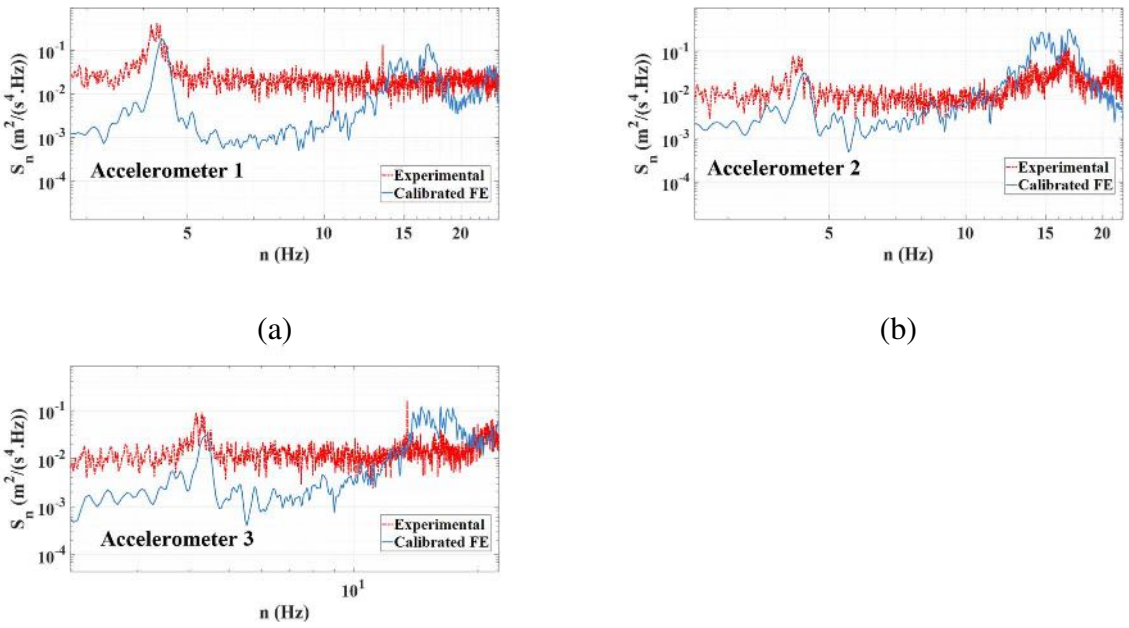

Figure 3.21. The power spectral density acceleration response of the validated FE model in closed condition at the accelerometer location #1 (A1), location #2 (A2), and location #3 (A3), compared to the experimental response for 40.23 m/s, and 90° wind.

3.4.2. Results of the open condition

The calibrated finite element (FE) model, simulated in open condition with a wind speed of 22.35 m/s and wind direction of 0°, is employed to assess the dynamic responses of the model. The model is subjected to varying wind loads, with wind speeds of 26.82 m/s and 31.29 m/s, and wind direction of 0°. The same C_p values are utilized to estimate the input nodal load time histories for each specific wind direction but with different wind speeds.

The validation results for the wind speed of 26.82 m/s and wind direction of 0° are shown in Table 3.10. Figure 3.22 displays the power spectral density (PSD) of accelerations at locations #1, #2, and #3, indicating a good agreement between the experimental data and the numerical analysis.

Table 3.11 presents the validation findings for the wind speed of 31.29 m/s and wind direction of 0°. The power spectral density (PSD) of accelerations at locations #1, #2, and #3 is depicted in Figure 3.23, illustrating a satisfactory concordance between the numerical analysis and experimental data.

Table 3.10. RMS of acceleration (m/s^2) time history of validated FE model in open condition, compared to the experimental results for 26.82 m/s and 0° wind.

Accelerometer	Experimental acceleration time history RMS (m/s^2)	Finite element acceleration time history RMS (m/s^2)	Difference (%)
1	0.1644	0.1955	18.91
2	0.3343	0.3705	10.82
3	0.3368	0.3220	1.42

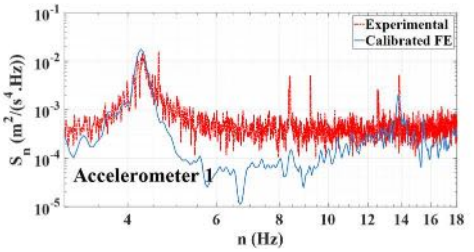

(a)

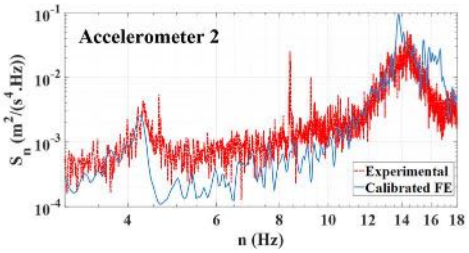

(b)

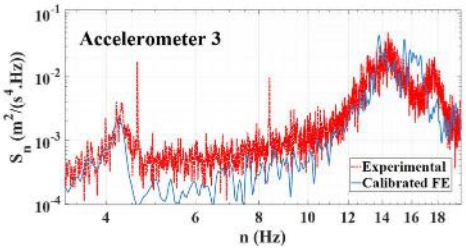

(c)

Figure 3.22. The power spectral density acceleration response of the validated FE model in open condition at the accelerometer location #1 (A1), location #2 (A2), and location #3 (A3), compared to the experimental response for 26.82 m/s, and 0° wind.

Table 3.11. RMS of acceleration (m/s^2) time history of validated FE model in open condition, compared to the experimental results for 31.29 m/s and 0° wind.

Accelerometer	Experimental acceleration time history RMS (m/s^2)	Finite element acceleration time history RMS (m/s^2)	Difference (%)
1	0.2964	0.2860	3.50
2	0.5296	0.5551	4.81
3	0.5505	0.4597	16.49

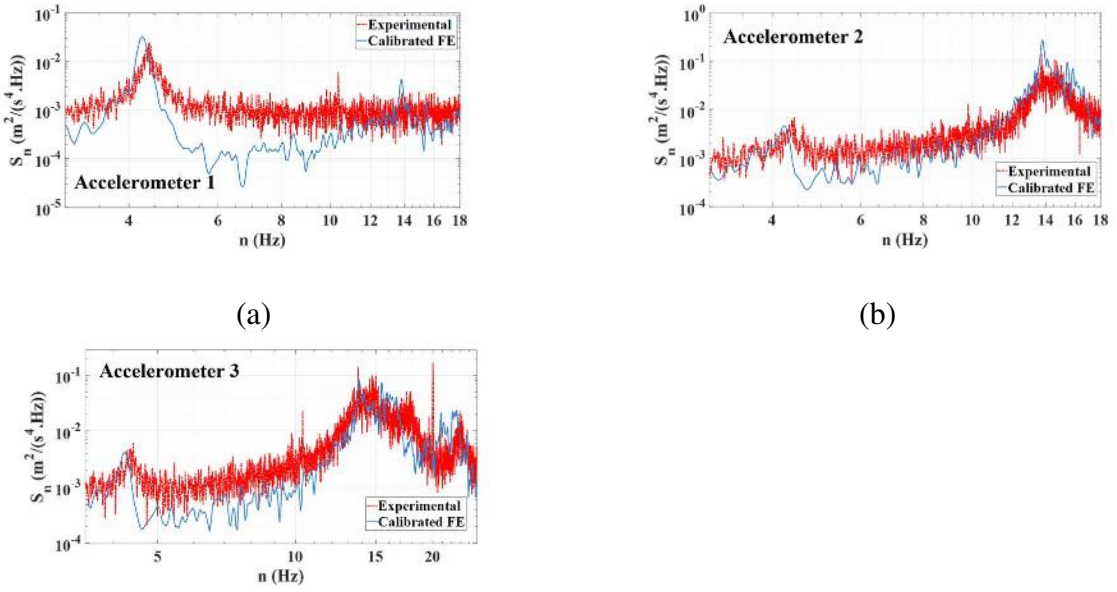

Figure 3.23. The power spectral density acceleration response of the validated FE model in open condition at the accelerometer location #2 (A2) and location #3 (A3), compared to the experimental response for 31.29 m/s, and 0° wind.

By utilizing the concept of dynamic amplification factor (DEA), façade designers can obtain essential information that aids in considering the contribution of resonant response in the design of façade elements and components. This is particularly important as current design methods primarily rely on quasi-static approaches rather than dynamic considerations.

The dynamic amplification factor is defined as Equation (3.1):

$$\mathrm{DAF} = \frac{\text{Peak Response (Resonant + Mean + Background)}}{\text{Peak Response (Mean + Background)}} \tag{3.1}$$

This can be summarized as Equation (3.2):

$$\mathrm{DAF} = \frac{\hat{F}_{B+M+R}}{\hat{F}_{M+B}} \tag{3.2}$$

The typical background and resonant parts of the response are schematically shown in Figure 3.24.

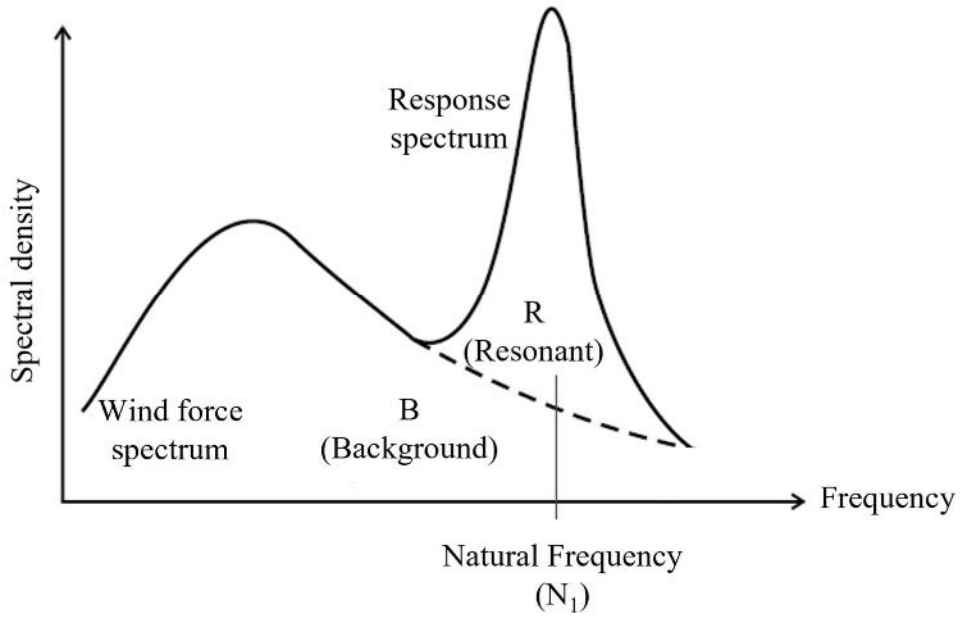

Figure 3.24. Typical background and resonant response, modified after Vutukuru (2021)

The metal hardware connections in the open condition of the operable window system are observed to be the most vulnerable component during normal to hurricane-level wind speeds, experiencing failures due to wind-induced vibrations. Hence, having an estimation of the resonant response contribution to the total wind-induced response is vital information regarding the design aspects of these connections. To this end, $\hat{F}_{B+M+R}$, the maximum peak axial force generated in each of the six hardware, including the resonance,

mean, and background response are calculated directly from FE analyses, for 22.35 m/s, 26.82 m/s, and 31.30 m/s wind speeds and 0° direction. $\hat{F}_{M+B}$, the maximum peak axial force generated in the hardware including the mean and the background response, not the resonance part, is calculated by the area averaging method. The DAF results of all the hardware connections are depicted in Table 3.12, while Figure 3.25 shows the numbering and location of the hardware connections. The results show higher DAF values for lower-elevated hardware connections, implying that these connections experience higher resonant vibrations and are the most critical in design.

Table 3.12. Dynamic Amplification factors of six metal hardware, 22.35 m/s, 26.82 m/s, and 31.30 m/s wind speeds and 0° direction

Hardware # as in Figure 3.25	DAF (22.35 m/s)	DAF (26.82 m/s)	DAF (31.30 m/s)
H1	1.01	1.16	1.21
H2	1.03	1.02	1.05
H3	1.34	1.40	1.39
H4	1.01	1.15	1.08
H5	1.02	1.04	1.06
H6	1.36	1.41	1.43

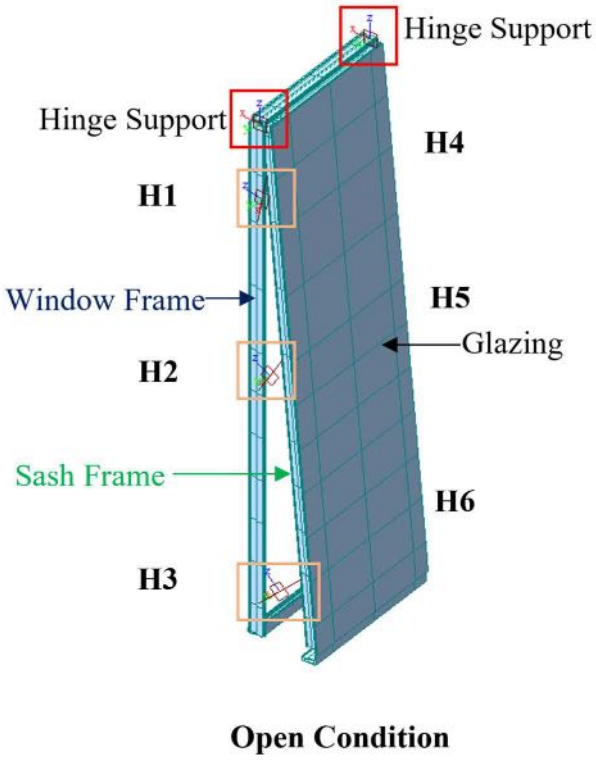

Figure 3.25. Numbering and locations of metal hardware connections

3.5. Concluding Remarks

The objective of this study is to fill the knowledge gaps in understanding the influence of wind-induced vibrations on the dynamic behavior of operable window systems in glass curtainwall structures. To achieve this, a highly accurate finite element (FE) model is developed, calibrated, and validated for closed and open conditions of the operable window, based on experimental data obtained from full-scale wind tunnel tests at the Natural Hazards Engineering Research Infrastructure (NHERI) Wall of Wind Experimental Facility (WOW EF) at Florida International University. The developed FE model is used to evaluate the dynamic response of the operable window system under different wind-

loading conditions, including varying wind speeds and wind directions, in both open and closed service conditions. Time history finite element analyses are conducted to determine the dynamic responses of the operable window system. The results demonstrate that the operable window systems and their connections may be susceptible to failure due to wind-induced resonant vibrations, which can occur at frequencies above 4 Hz, highlighting the importance of analyzing the vibration effects, which are not currently required by the ASCE 7 Standard. The PSD response of the acceleration response of the operable window system shows major frequencies near 4 Hz, 14 Hz, and 17 Hz, for closed and open conditions of the window system. These frequencies are successfully reflected by the calibrated and validated FE models. Moreover, the dynamic response of the operable window system, in the open condition indicates that lower-elevated metal hardware connections show higher dynamic amplification factor values. This means that these connections are more influenced by the resonant vibrations during normal to hurricane-level wind speeds. This implies that the bottom hardware connection is the most vulnerable to failure and should be given the utmost consideration when designing the metal hardware to withstand possible failure at any given wind speed and direction.

CHAPTER 4 . NUMERICAL STUDY ON WIND-INDUCED DYNAMIC BEHAVIOR OF A CLOSED-CAVITY DOUBLE-SKIN FAÇADE CURTAINWALL SYSTEM

4.1. Introduction

As stated by the US Department of Energy, buildings account for 41% of the overall energy usage in the United States, with heating, ventilation, and air conditioning systems responsible for 50% of this figure (Wu et al., 2016). Controlling energy consumption and minimizing environmental impact in a building, particularly in taller and larger structures like skyscrapers that consume more energy overall, primarily depends on the building envelope (Oh, 2020). Moreover, the presence of discontinuities in a building envelope, both within and between units, can lead to water infiltration. This may result in expensive interior damage due to rainwater penetration. Consequently, those involved in constructing buildings and stakeholders in the building and energy sectors place a high value on glazed building envelopes that are both watertight and energy-efficient, while also possessing aesthetic qualities.

In recent years, the use of double-skin glazed curtainwalls has become increasingly popular as they offer benefits such as improved energy efficiency, watertightness, transparency, acoustic performance, and reduced maintenance costs (Pracucci et al., 2020). Although the concept of the double-skin façade is not new, it has been gaining popularity in modern European architecture due to its environmental and solar energy benefits (Bielek et al., 2017). The combination of the growing prevalence of high-rise buildings and the widespread use of glazed facades in modern architecture has resulted in higher energy

consumption. As a result, employing double-skin facades has emerged as a significant potential solution (Saroglou et al., 2020).

A double-skin façade consists of an exterior façade, an internal skin, and an intermediate air gap (Hashemi et al., 2010), resulting in the presence of two glass walls in the DSF. The exterior facade of the DSF is referred to as the rain screen, while the internal layer is known as the air barrier. The intermediate air space is commonly referred to as the cavity. Studies indicate that double-skin curtain walls offer superior energy efficiency (Høseggen et al., 2008) and improved water resistance compared to their single-skin counterparts. The primary reason for the improved water resistance performance of DSFs is their ability to achieve pressure equalization. This is primarily due to the presence of an air gap. Double-skin curtain walls that rely on pressure equalization to resist water ingress are referred to as PER systems. The underlying principle of this mechanism is that differential pressure is the primary cause of water infiltration in curtain walls. By minimizing this pressure differential, a waterproof system can be achieved (Killip & Cheetham, 1984). In an ideal PER curtainwall, there is no pressure difference between the external pressure and the cavity pressure (Baskaran & Brown, 1992). Despite being utilized in practical applications for several years, there have been limited experimental and numerical studies conducted to establish a connection between the pressure equalization present in the facade and the structural response. Pomaranzi et al (2020) conducted a series of wind-tunnel tests on permeable double-skin facades that were attached to low-rise building samples. The results indicated that the inner layer of the permeable DSF experienced lower positive and negative peak pressures compared to a standard single-skin facade. The outer skin of the permeable DSF can impact the wind-induced pressure distribution on the inner skin,

resulting in lower design peak pressures. Despite this, codes like Eurocode do not currently account for this reduction when calculating wind loads. Conversely, a study by da Silva and Gomes (2008) found that when the porosity of the outer skin is relatively high, the reduction in design loads resulting from the altered pressure distribution of the inner skin cannot be reliably confirmed. A reduction in wind-induced pressure on the inner skin can only be achieved when the porosity level of the DSF is less than 1%.

Double-skin facades suffer from several issues such as mist and dust accumulation in the cavity, as well as relatively high maintenance costs. In order to address these drawbacks and improve thermal and acoustic insulation performance(van den Bossche et al., 2020), a "closed cavity" DSF has been developed. This type of DSF differs from traditional double-skin facades in that it has significantly lower cavity permeability, roughly one order of magnitude lower, and is supplemented with a supply of dry air into the cavity. The modified cavity features of the closed cavity DSF reduce both dust accumulation and air condensation. This type of DSF consists of an external wall (single-glazing or double-glazing), a low-permeability air cavity, and an internal wall (double-glazing or triple-glazing). This configuration is similar to the traditional DSF, referred to as the "vented cavity" in this study.

The closed cavity double-skin facade (DSF) utilizes a technique that involves sealing the glass and frame on all sides to prevent water infiltration. Pressure equalization is also employed to prevent water ingress. Compared to a PER DSF system, the closed cavity DSF has a lower level of permeability in its cavity. The permeability of a PER DSF may vary depending on the design requirements, such as load sharing and water penetration

resistance. Additionally, the air within the cavity of a PER system is vented only to the rainscreen (the external wall), whereas in the closed cavity system, venting can occur in either direction.

One of the focal points of research in double-skin curtainwall systems is the load sharing between the external and internal walls (Kala et al., 2008). The distribution of loads in permeable systems, such as PER curtainwalls, is influenced by the level of permeability in the cavity. This level is typically regulated by the size of the vents in the external wall or cavity, as well as the internal wall's leakage. According to Irwin et al. (1984), a perfectly vented cavity in a double-skin curtainwall system results in the rainscreen carrying 70% of the wind cladding load. In a pressure-equalized double-skin curtainwall, Ganguli et al. (1988) found that the external wall carries 75% of the wind loading. Most of the past and present research has focused on pressure-equalized double-skin facade (DSF) systems, with less attention given to closed cavity DSF systems due to their relative novelty. Recent studies on closed cavity DSF systems have mainly centered on energy efficiency and thermal performance, with a limited investigation into their structural behavior under wind load. Furthermore, there are currently no guidelines or studies on load distribution between the external and internal walls for closed cavity systems.

Only a limited number of studies have examined the wind-induced dynamic behavior of double-skin curtainwall systems using numerical methods. These studies have mainly concentrated on reducing wind-induced vibration affecting the façade's dynamic response or utilizing the facade as an energy absorber to mitigate the building structure's dynamic response. Azad (2016) examined the viability of a smart double-skin facade as a damping

system for mitigating wind-induced acceleration response in structures. The study utilized a finite element model of the double-skin facade to determine the ideal stiffness and damping value of the brackets, which connect the facade to the building structure. They showed that a combination of using a movable outer skin and an energy dissipation system as brackets can effectively reduce the peak wind-induced acceleration of the structure. Abdelaziz et al. (2021) utilized fluid-solid interaction (FSI) models and a data-driven optimization framework to identify the optimal orientation of an active double-skin facade, with the goal of minimizing wind-induced vibration in a tall building. Jafari and Alipour (2021) created a framework that utilizes computational fluid dynamics (CFD) simulations and statistical analysis to reduce wind-induced drag forces on tall buildings. This is achieved by optimizing the shape of rectangular and elliptical double-skin facades.

This chapter aims to fill the knowledge gap in the wind-induced performance of closed-cavity double-skin curtainwall systems. This examines the wind-induced dynamic behavior of a closed-cavity double-skin facade curtainwall model. A finite element model was developed, calibrated, and validated against wind-tunnel test results from a full-scale closed-cavity double-skin curtainwall at the NHERI Wall of Wind (WOW) Experimental Facility at Florida International University. Based on the developed closed-cavity configuration, the effect of higher permeability due to defects on the dynamic response of the façade is also investigated.

4.2. Wind tunnel tests

The wind tunnel tests were conducted at the NHERI Wall of Wind (WOW) experimental facility (EF) located at Florida International University on a full-scale model. The facility,

as depicted in Figure 4.1, consists of a set of 12 fans capable of producing hurricane-level wind speeds up to category 5, facilitating wind tunnel tests with varying wind speeds. Furthermore, the testing facility includes a rotating turntable located in front of the flow box, enabling consideration of different wind directions (Gan Chowdhury et al., 2017).

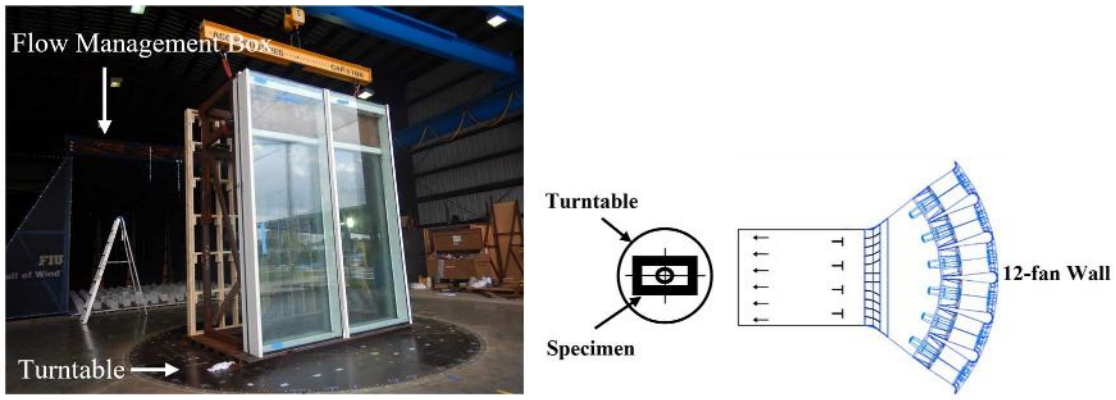

(a) (b)

Figure 4.1. FIU Wall of Wind (WOW) Experimental Facility (EF): (a) Inside the WOW EF: Flow management box and the turntable; (b) Schematic drawing of the WOW EF plan

4.2.1. Double-skin façade curtainwall configuration

The double-skin façade curtainwall at full-scale consists of two identical closed cavity DSF units, with each unit measuring 1.35 m (53”) in width and 3.63 m (143”) in height. These units are positioned and attached adjacent to each other, as illustrated in Figure 4.2a. The model of the closed cavity DSF consists of three main components: outer skin, inner skin, and the cavity located between them. The outer skin is single-glazed, while the inner skin consists of a triple-glazed unit, comprising three glass panes. The cavity between the outer and inner skin (external and internal walls) has a depth of 140 mm. The specimen has a polycarbonate side that is geometrically identical to the curtainwall and is attached to a wooden frame on the rear side, as illustrated in Figure 4.2b. Additionally, there is a flat roof with overhangs, as indicated in the figure. The constructed DSF curtainwall specimen is

upheld by a steel structure that is fixed to the turntable. This steel structure has a rectangular shape with dimensions of 3 m (width) × 1.83 m (breadth) × 3.65 m (height) as displayed in Figure 4.3.

(a) (b)

Figure 4.2. DSF model (a) The glazed side of the model (b) The polycarbonate side of the model

Figure 4.3. Supporting steel structure bolted to the turntable.

The polycarbonate side of the specimen makes it possible to install pressure taps for measuring external wind pressure. This is because drilling pressure taps into the actual glass on the glazed side of the curtainwall is not feasible. Figure 4.4 depicts the plan view of the model and a sectional view of the corner of the curtainwall unit.

This study involved testing two types of double-skin curtainwalls. The first type was an ideal closed cavity configuration, while the second type was a vented-cavity DSF with a 10 mm opening on the side of the unit, as shown in Figure 4.5. The vented-cavity configuration was used to simulate a scenario in which the cavity had a defect, resulting in higher cavity permeability.

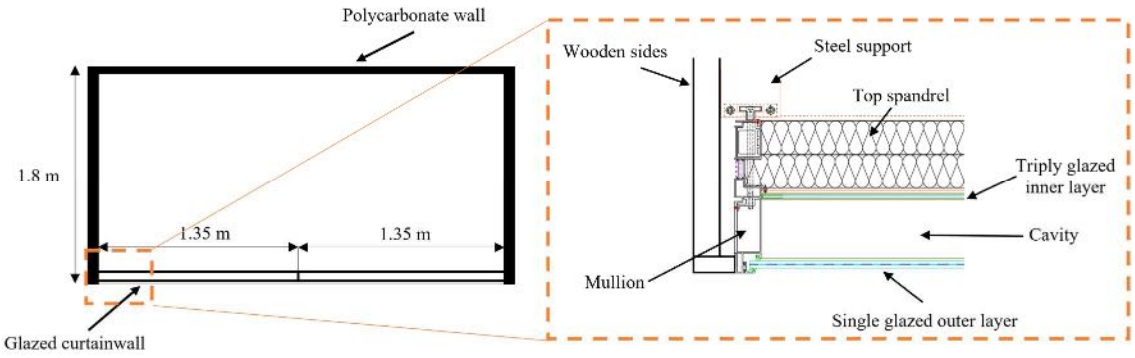

Figure 4.4. Plan view of the DSF curtainwall model

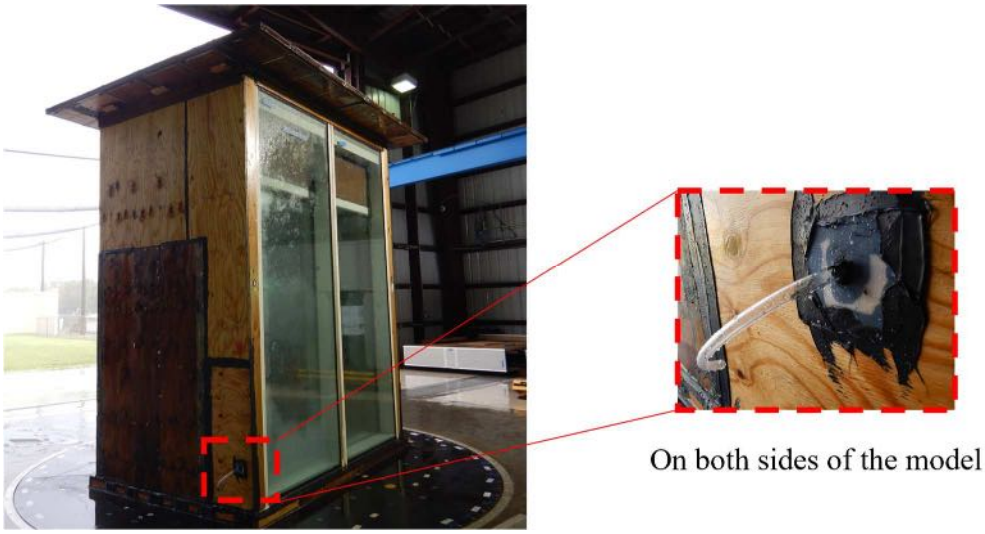

Figure 4.5. Vented-cavity DSF

4.2.2. Instrumentation and testing protocol

In all experimental tests, an atmospheric boundary layer (ABL) with an open terrain was simulated, taking into account a roughness length of 0.08 m (z_0), and the reference height for wind speeds (z_{ref}) was set to the height of the roof (i.e., 3.8 m). To record the surface pressure, 100 pressure taps were positioned on the two polycarbonate walls, while two pressure taps were installed inside the specimen building to measure the cavity pressure of the DSF unit. Figure 4.6 displays the arrangement of the pressure taps on the polycarbonate unit. During the pressure tests, the time histories of wind pressure on the outer skin (on the polycarbonate side), cavity (within the DSF units), and internal pressure (inside the steel frame) are recorded and collected. The experiments involved testing both closed and vented cavity models under various wind speeds and directions. Specifically, the tests were conducted for three wind speeds, namely 22.35 m/s (50 mph), 31.3 m/s (70 mph), and 40.23 m/s (90 mph), and at 15° intervals for wind directions ranging from 0° to 180°. Each wind direction was maintained for a duration of 2 minutes. The pressure time histories that were

recorded are presented in terms of the pressure coefficient, denoted as C_P. Equation (4.1) provides the definition of the pressure coefficient value, while Equation (4.2) outlines the definition of differential cavity pressure.

$$C_{P_{peak}} = \frac{\mathrm{P_{peak}}}{\frac{1}{2}\rho_{air}\mathrm{U_{3s}^2}} \tag{4.1}$$

$$P_{diff.cav} = P_{cav} - P_{atm} \tag{4.2}$$

Where, $\mathrm{U_{3s}}$ is the peak 3s wind speeds at the roof height of the model, ρ_{air} is the air density while $\mathrm{P_{peak}}$ is the differential peak pressure, $P_{diff.cav}$ is the differential cavity pressure, P_{cav} is the cavity pressure and P_{atm} is the atmospheric pressure. By using the tubing transfer function, any distortions resulting from the length of the tubing are corrected, after which the C_P values are computed (Irwin et al., 1979).

The dynamic tests were carried out on the glazed curtainwall side of the model and involved collecting time histories of acceleration and strain for wind speeds of 22.35 m/s (50 mph), 31.3 m/s (70 mph), and 40.23 m/s (90 mph), and for wind directions ranging from 0° to 180° at 15° intervals. Figure 4.7 and Figure 4.8 depict the placement of the accelerometers and strain gauges on both the glass and mullions of the unit. The testing protocol is outlined in Table 4.1. The wind direction is defined in Figure 2.7.

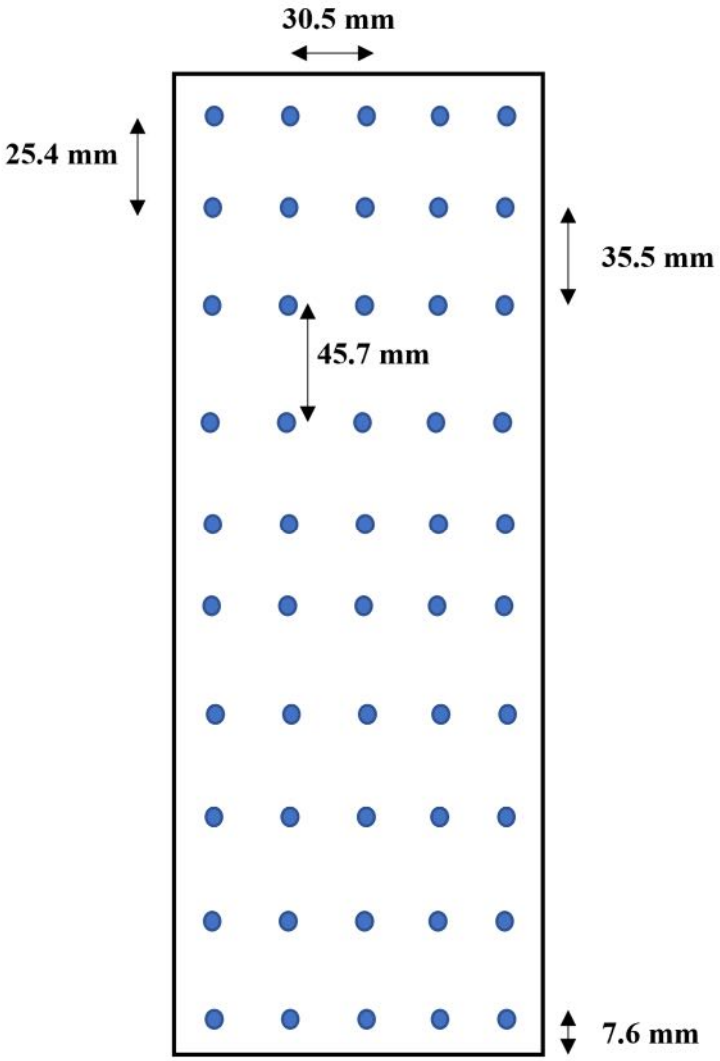

Figure 4.6. Pressure tap arrangement on one of the polycarbonate units (blue dots represent pressure tap locations)

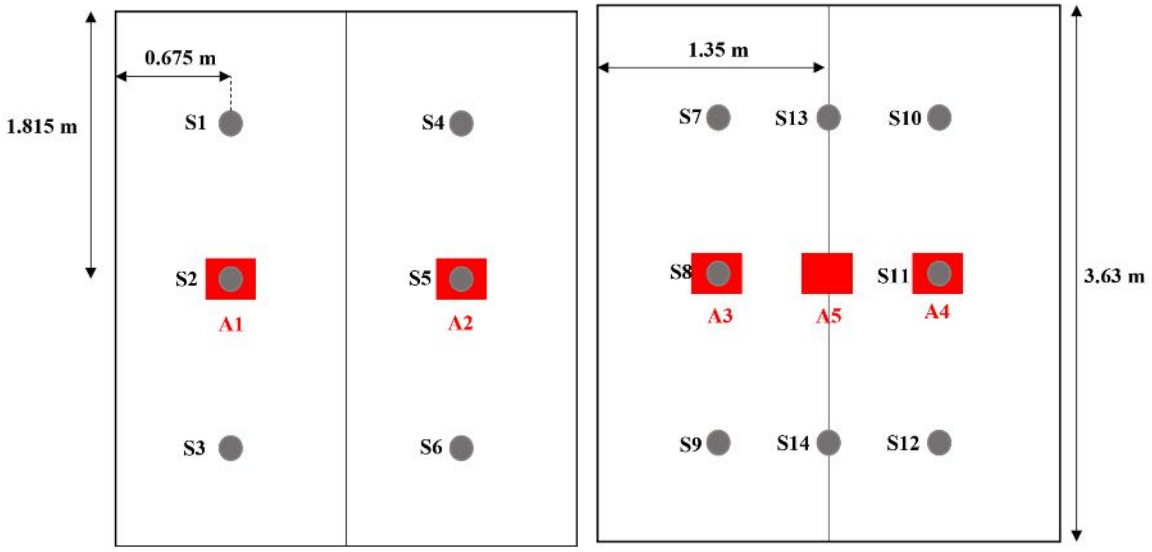

(a) (b)

Figure 4.7. The layout of accelerometers (A) and strain gauges (S) on the double-glazed glass unit (a) External wall (b) Internal wall

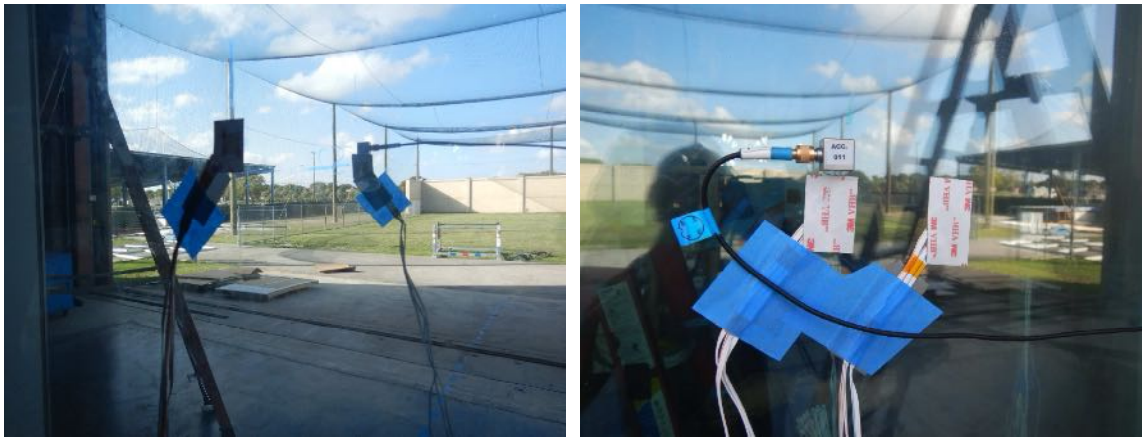

(a) (b)

Figure 4.8. Instrumentation on the double-glazed glass unit (a) Strain gauge on glass (b)Accelerometer on glass

Table 4.1. Testing protocol per configuration

Test Type	Wind Speed (m/s)	Wind Direction (degree)	Test Duration (mins.)
Pressure	22.4, 31.3 and 40.2	0 to 180 in 15 increments	2
Dynamic	22.4	0 to 180 in 15 increments	10
Dynamic	31.3	0 to 180 in 15 increments	5
Dynamic	40.2	0 to 180 in 15 increments	5

4.3.Numerical modeling and calibration

4.3.1. Finite element modeling of the double-skin façade curtainwall model

A finite element (FE) model has been created for the double-skin façade curtainwall specimen. This model will be utilized to reproduce the wind-induced dynamic behavior of the specimen during full-scale tests conducted at the WOW EF, under various wind loading scenarios. The FE model of the double-skin façade curtainwall specimen was developed using Midas Gen FEA software (2021) and is displayed in Figure 4.9. The model encompasses the entire structure of the specimen, including the double-skin façade curtainwall, supporting steel structure, polycarbonate panels, wooden frame, wooden sidewalls, and the roof. Two versions of the FE model have been created to investigate low-permeability and high-permeability cases tested in the wind-tunnel tests: the closed cavity model and the vented cavity model. This section provides significant details and characteristics of the developed FE model.

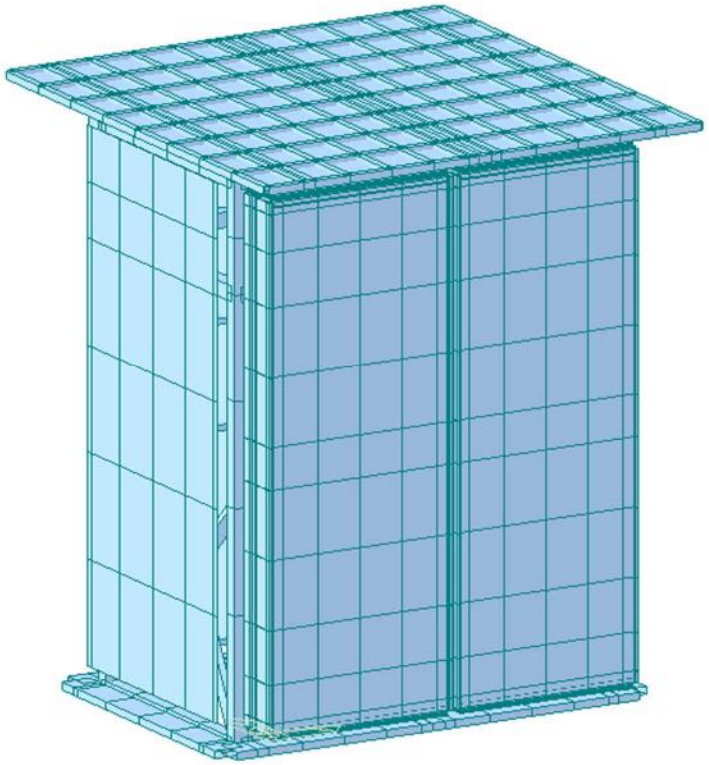

Figure 4.9. The developed finite element double-skin façade curtainwall model

4.3.1.1. FE modeling of the DSF curtainwall

Modeling the frames: The double-skin façade curtainwall framing consists of an external frame positioned between the external and internal glazing skins. This frame comprises a series of aluminum beam elements, referred to as the mullions and transoms, which are the vertical and horizontal elements, respectively. In the finite element model of the DSF curtainwall unit, 12 degrees-of-freedom (DOF) beam elements are employed to model the mullion and transom profiles. The cross-sectional properties of the profiles, including I_{XX}, I_{YY}, and I_{XY} are computed and modeled based on the CAD drawing of the actual profiles.

Modeling the connection between the frames: In each unit, the mullion and transom frames (i.e., vertical and horizontal frames) are connected by sharing a node. However, a different

approach is necessary to model the mechanical coupling between frames. To simulate the interactions between the frames of two adjacent units, where two side-by-side mullions are connected through mechanical connectors, 6 degrees-of-freedom (DOF) elastic links are employed. Each elastic link has 6 DOFs with corresponding translational and rotational stiffness values in all local x-, y-, and z-directions. Figure 4.10 illustrates how the connections between the frames of the left and right units are modeled using these elastic links.

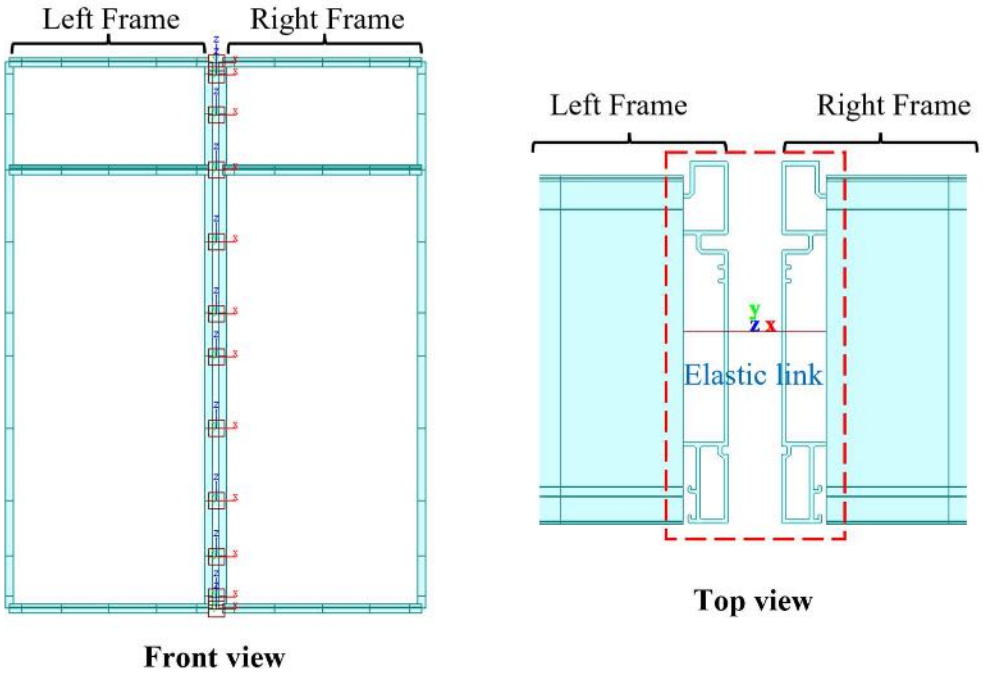

Figure 4.10. Modeling the inter-frame coupling via 6 DOF elastic links

Modeling the glass: The double-skin curtainwall consists of a single-glazing external skin and a triple-glazing internal skin, as shown in Figure 4.11. The finite-element modeling of the glass layers takes into account the actual thickness values of the glass panes, with 4-node thin plate elements used to model the external and internal skins. In order to simulate

the inter-pane cavity pressure between each pair of panes within the triple-glazing unit, 3 degrees-of-freedom (DOF) elastic links are utilized, as depicted in Figure 4.12. The stiffness values of the modeled elastic links are presented in Table 4.2.

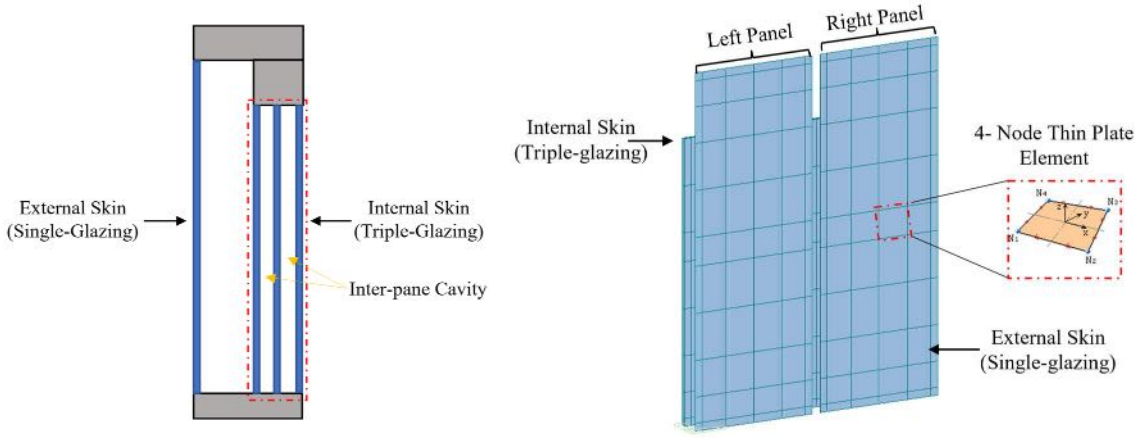

(a) (b)

Figure 4.11. Glass Modeling: (a) Schematic of the external and internal skins (b) FE modeling of the glazing via 4-node thin plate elements.

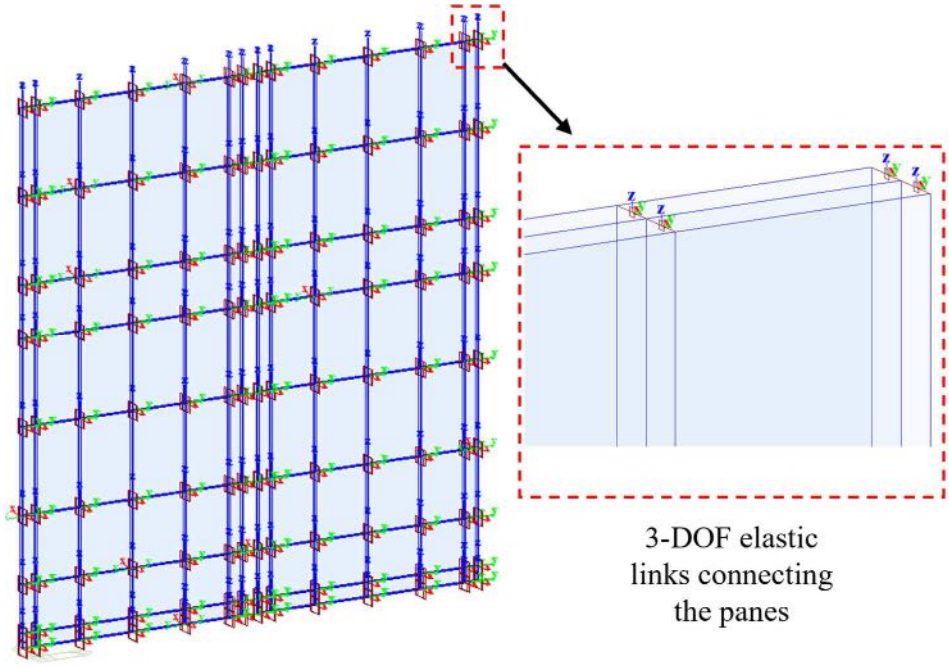

Figure 4.12. Modeling the inter-pane cavity of the internal skin triple-glazing unit via 3-DOF elastic links

Table 4.2. 3-DOF elastic links stiffness properties for modeling the inter-pane cavity

Model Parameter	Axial Stiffness (KN/m)	Shear Stiffness (KN/m)	Rotational Stiffness
3 DOF elastic link for modeling inter-pane cavity	499.98	499.98	0

Assembling the modeled frames and glasses: The attachment between the external skin glazing and the aluminum frame, as well as between the aluminum frame and the internal skin glazing, is facilitated by structural silicone. To incorporate these connections in the finite element model, 6 degrees-of-freedom (DOF) elastic links are employed to replicate the actual mechanical characteristics of the structural silicone. The assembly of the external and internal glazing skins to the aluminum frame of the DSF curtainwall is illustrated in Figure 4.13.

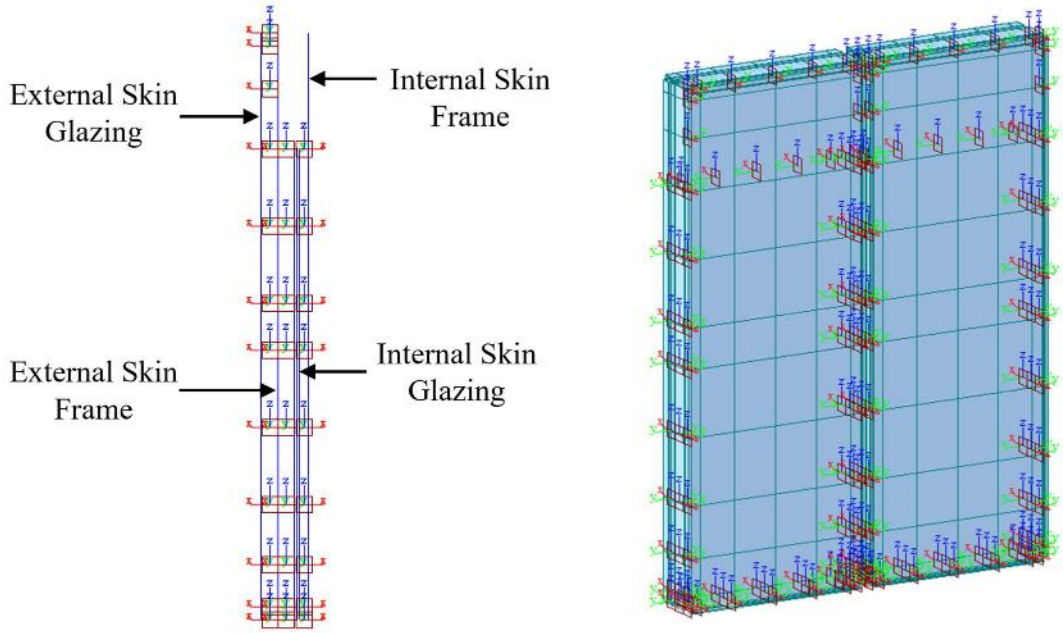

Figure 4.13. Modeling structural silicone via 6 DOF elastic links

4.3.1.2. FE modeling of the whole structure

The finite element model of the supporting steel structure is presented in Figure 4.14. The main structure is connected to a set of perimeter beams at the bottom, which are bolted to the turntable. The bolt connections to the turntable are modeled via hinge point spring supports. To model the beams and columns of the steel structure, 12 DOF beam elements are employed in the finite element model, based on the actual section properties of the beam/column elements as depicted in Figure 4.14. Table 4.3 provides the corresponding cross-sectional properties of the framing profiles. Subsequently, the developed DSF curtainwall units are mounted to the front side of the supporting steel structure, while the wooden frames and poly-carbonate panels are attached to the rear side of it, as shown in Figure 4.15. The finite element models of the side walls and the roof are then added to the structure, as indicated in the figure. The material properties used in the modeling of the whole structure finite element model are described in Table 4.4.

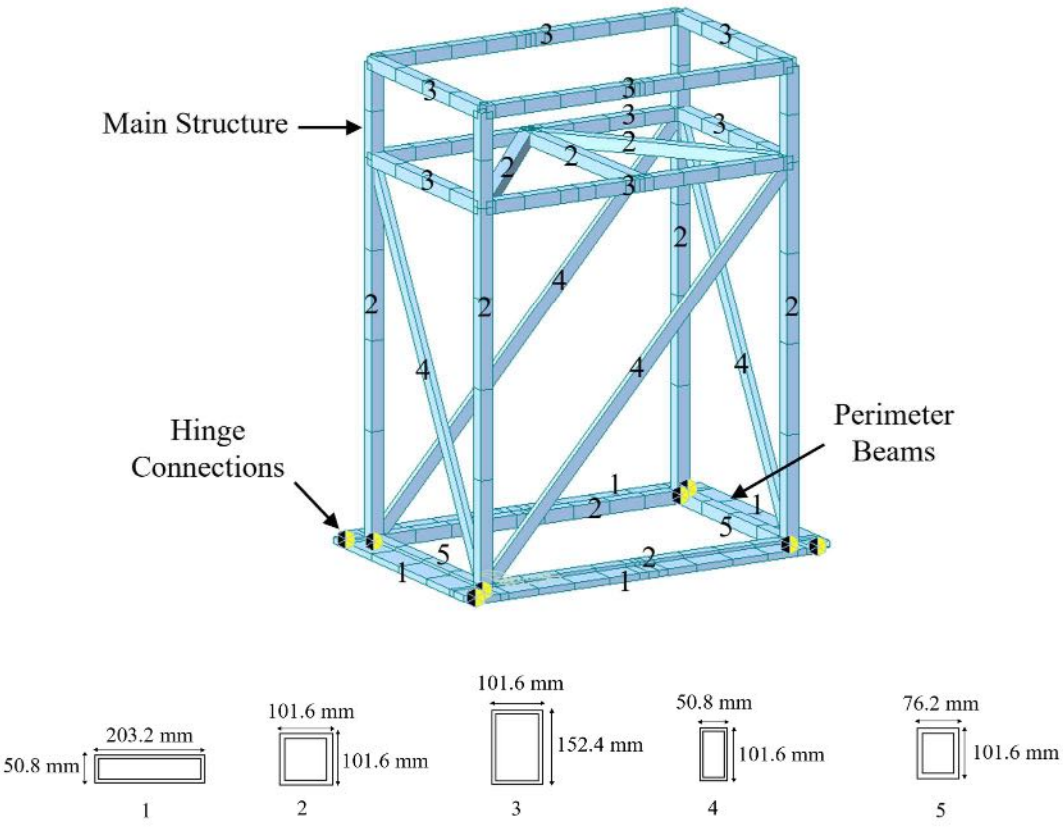

Figure 4.14. FE model of the supporting steel structure with its bolted connections to the turntable, framing layout, and the cross sections of the five framing profiles.

Table 4.3. Cross-sectional properties of the framing profiles of the supporting steel structure

Framing Profile	Area (mm^2)	I_{XX} (mm^4)	I_{YY} (mm^4)	I_{XY} (mm^4)
1	4470	1.72e6	1.89e7	5.17e6
2	3503	5.00e6	5.00e6	7.43e6
3	4470	1.36e7	7.06e6	1.40e7
4	2542	2.95e6	8.89e5	2.06e6
5	3026	3.98e6	2.45e6	4.52e6

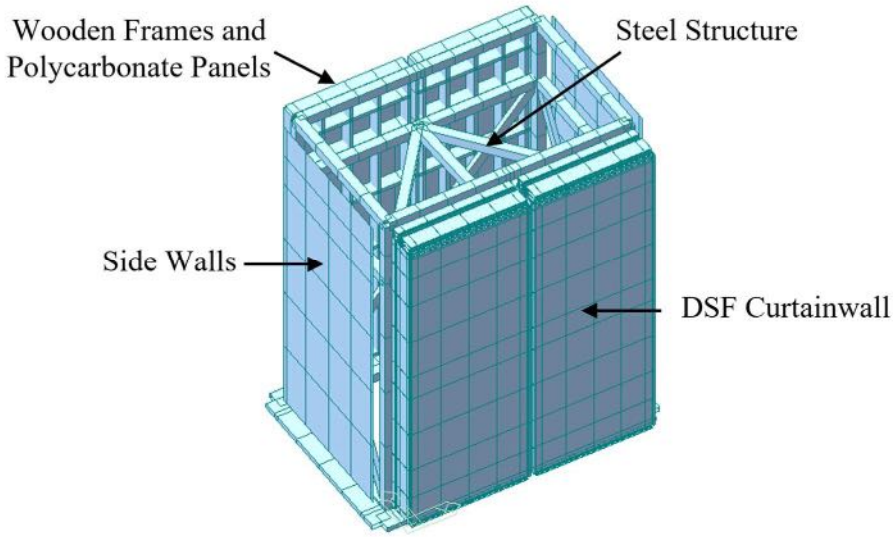

Figure 4.15. DSF curtainwall (front) and polycarbonate panel (rear) mounted to the supporting steel structure; the roof is not shown in the figure.

Table 4.4. Material properties used in the finite element model

Material	Modulus, E (MPa)	Poisson ratio, v	Density, ρ (kg/m^3)
Aluminum	70940	0.33	2768
Steel	200000	0.30	7861
Wood	4000	0.31	830
Polycarbonate	1793	0.31	1190

4.3.2. Calibration

To calibrate the model parameters of the closed-cavity DSF system, the 100-pressure time history (TH) data is collected based on C_p (pressure coefficient). For dynamic analysis with Midas Gen FEA software, nodal load time history input is required. As a result, the C_p time histories are transformed into pressure time histories utilizing Equation (2.1) and into nodal load time histories utilizing Equation (2.2), which account for each node's tributary area. However, since the pressure tap locations in the experiment do not match precisely with the node locations, interpolation is utilized to obtain time history data.

Moreover, the collected cavity pressure time history data of the left and right panels, measured by the two additional pressure taps are converted to nodal time history and applied to the FE model.

The process of calibration involves iteratively adjusting the model parameters until the numerical model can replicate a dynamic response that closely matches the experimental data. In order to deem the finite element (FE) model 'calibrated', the root mean squares (RMS) of all acceleration (RMS_{ACC}) responses must be within 10 percent of the experimental data. Table 4.5 provides a summary of the tuned parameters.

Table 4.5. Internal parameters and their tuned values

#	Model parameters	Axial stiffness (kN/m)	Shear stiffness (kN/m)	Rotational stiffness (kN·m/rad)
(1)	Curtainwall's top connection to the steel structure	17512.68	17512.68	2.00
(2)	Curtainwall's bottom connection to the steel structure	5253.80	5253.80	0.59
(3)	The steel structure supports modeled with point springs	6479.69	6479.69	0.00
(4)	Inter-mullion connection	1751.27	1751.27	0.20
(5)	External glazing silicone	227.66	227.66	0.02
(6)	Internal glazing silicone	122.58	122.58	0.01

The FE model of the closed-cavity DSF is calibrated for 22.4 m/s wind speed and 0° wind direction. Table 4.6 compares the acceleration response of the calibrated FE model with the experimental response of the specimen for all accelerometers at locations #1, #2, #3, #4, and #5, respectively. The results indicate that there is a difference of less than 10 percent between the RMS of the acceleration time history response of the numerical and

experimental responses for all the accelerometers. In Figure 4.16, the acceleration responses in the frequency domain at location #3 are compared, where the power spectral density (PSD) of the acceleration response of the FE model is plotted against the experimental response. The comparison shows that the calibrated FE model captures the major frequencies in the acceleration response. Specifically, the calibrated FE model captures the major frequency of 3.6 Hz, and the other major frequencies of 13.3 Hz, 16.4 Hz, 20.1 Hz, and 36.0 Hz of the closed-cavity DSF system are captured by the numerical model at 3.8 Hz, 13.8 Hz, 16.0 Hz, 18.6 Hz, and 35.0 Hz, respectively. Figure 4.17 demonstrates the acceleration PSD response of the other accelerometers, through a comparison between the FE model and the experimental results.

Table 4.6. RMS of acceleration (m/s^2) time history of calibrated FE model of the closed-cavity DSF, compared to the experimental results for 22.4 m/s and 0° wind.

Accelerometer	Experimental acceleration time history RMS (m/s^2)	Finite element acceleration time history RMS (m/s^2)	Difference (%)
1	0.1429	0.1523	6.17
2	0.1911	0.1819	4.81
3	0.1401	0.1304	6.92
4	0.1348	0.1408	4.45
5	0.0488	0.0527	7.99

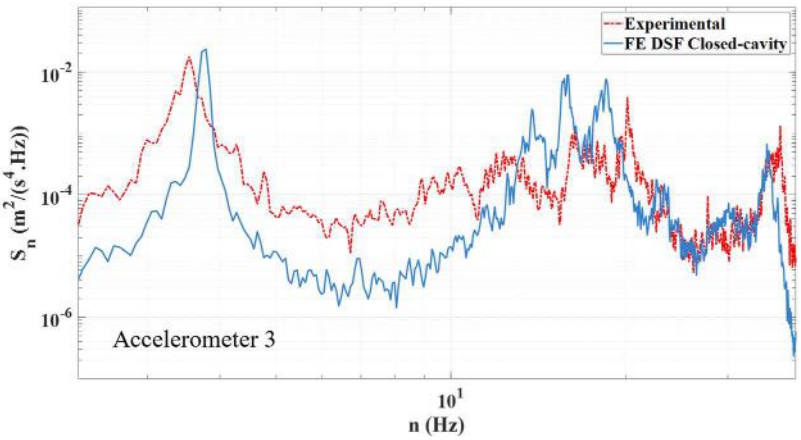

Figure 4.16. The power spectral density acceleration response of the calibrated FE model, at the accelerometer location #3 (A3) compared to the experimental response for 22.4 m/s, and 0° wind.

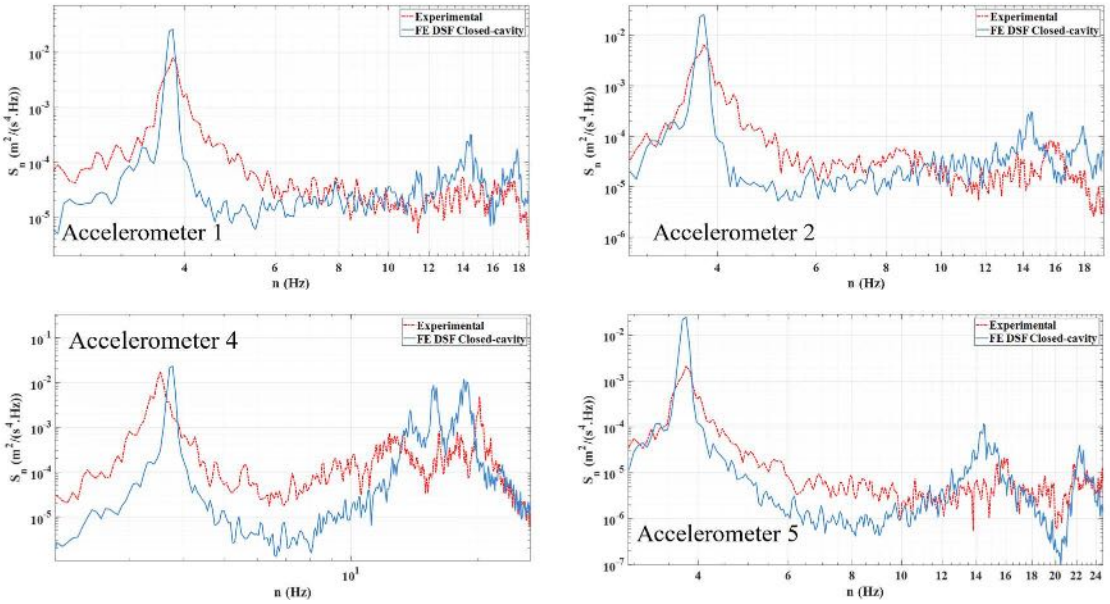

Figure 4.17. The power spectral density acceleration response of the calibrated FE model, at the accelerometer locations #1, #2, #4, and #5 compared to the experimental response for 22.4 m/s, and 0° wind.

4.4. Numerical analysis results

4.4.1. Closed-Cavity DSF

The finite element (FE) model of the closed-cavity DSF, previously calibrated, is utilized to evaluate the dynamic responses of the model. The model is subjected to different wind loads, including wind speeds of 31.3 m/s and 40.2 m/s, and wind directions of 0°, 45°, and 90°. Time history analysis is conducted by applying corresponding external, cavity, and internal pressure time histories to the FE models, which vary with each specific wind speed and wind direction.

The validation results indicate that the acceleration responses are acceptably captured for higher wind speeds. The validation results for a wind speed of 31.3 m/s and wind direction of 0° are summarized in Table 4.7. As indicated in the table, the validated FE model's RMS of acceleration response shows less than 15 percent difference compared to the experimental results. Figure 4.18 displays the power spectral density (PSD) of accelerations at location #3, demonstrating a good agreement between the numerical analysis and experimental data.

Table 4.7. RMS of acceleration (m/s^2) time history of validated FE model of the closed-cavity DSF, compared to the experimental results for 31.3 m/s and 0° wind.

Accelerometer	Experimental acceleration time history RMS (m/s^2)	Finite element acceleration time history RMS (m/s^2)	Difference (%)
1	0.2559	0.2942	14.96
2	0.2851	0.3153	10.59
3	0.3235	0.3262	0.83
4	0.3649	0.3357	8.00
5	0.1139	0.1252	9.92

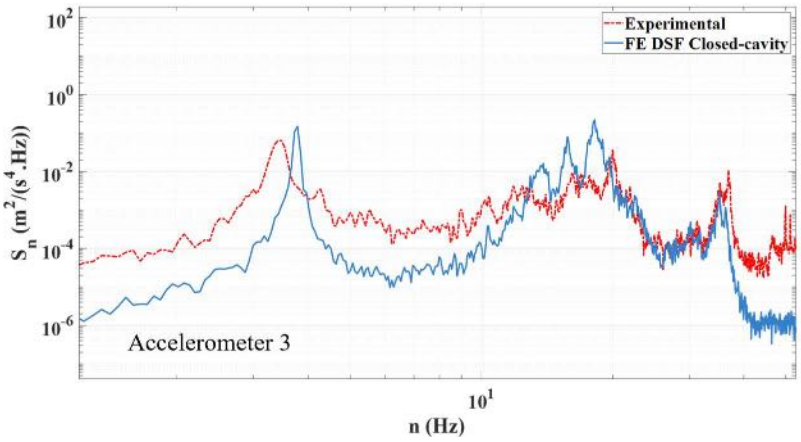

Figure 4.18. The power spectral density acceleration response of the validated FE model, at the accelerometer location #3 (A3) compared to the experimental response for 31.3 m/s, and 0° wind.

The validation results for a wind speed of 40.2 m/s and wind direction of 0° are presented in Table 4.8. The table indicates that the RMS of acceleration response from the validated FE model exhibits a difference of less than 15 percent compared to the experimental results.

Table 4.8. RMS of acceleration (m/s^2) time history of validated FE model of the closed-cavity DSF, compared to the experimental results for 40.2 m/s and 0° wind.

Accelerometer	Experimental acceleration time history RMS (m/s^2)	Finite element acceleration time history RMS (m/s^2)	Difference (%)
1	0.5033	0.5740	12.31
2	0.5018	0.5757	14.72
3	0.7394	0.7445	0.69
4	0.6999	0.7454	6.50
5	0.1934	0.2148	11.06

The validation analysis results are presented for oblique and crosswind directions. The validation findings for a wind speed of 22.4 m/s and wind direction of 45° are summarized

in Table 4.9. The table shows that the RMS of acceleration response from the validated FE model has a difference of less than 15 percent compared to the experimental results.

Table 4.9. RMS of acceleration (m/s^2) time history of validated FE model of the closed-cavity DSF, compared to the experimental results for 22.4 m/s and 45° wind.

Accelerometer	Experimental acceleration time history RMS (m/s^2)	Finite element acceleration time history RMS (m/s^2)	Difference (%)
1	0.1396	0.1369	1.93
2	0.1462	0.1656	13.26
3	0.1127	0.1135	0.70
4	0.1038	0.1190	14.64
5	0.0325	0.0367	12.92

The validation results for a wind speed of 22.4 m/s and wind direction of 90° are presented in Table 4.10. The table demonstrates that the RMS of acceleration response from the validated FE model exhibits a difference of less than 10 percent compared to the experimental result, except the results for accelerometer 3 which shows 29.01 percent difference.

Table 4.10. RMS of acceleration (m/s^2) time history of validated FE model of the closed-cavity DSF, compared to the experimental results for 22.4 m/s and 90° wind.

Accelerometer	Experimental acceleration time history RMS (m/s^2)	Finite element acceleration time history RMS (m/s^2)	Difference (%)
1	0.1374	0.1244	9.46
2	0.1346	0.1474	9.51
3	0.2006	0.1424	29.01
4	0.1505	0.1456	3.25
5	0.0426	0.0429	0.70

Figure 4.19 illustrates the impact of wind speed on the RMS of acceleration response for the external and internal glazing units of the closed-cavity DSF. The results clearly

demonstrate a significant increase in vibration levels on both the external and internal glazing units as the wind speed increases. The RMS of acceleration for the external glazing at a wind speed of 40.2 m/s is 3.52 times higher compared to the 22.4 m/s wind. The FE analysis shows a similar trend, estimating the increasing factor to be 3.76. Moreover, the results show that the RMS of acceleration for the internal glazing at a wind speed of 40.2 m/s is 5.28 times higher compared to the 22.4 m/s wind. The FE analysis validates this observation, estimating the increasing factor to be 5.71. This significant rise in wind-induced vibration of the external and internal glazing units may lead to an increased likelihood of water ingress, particularly at higher wind speeds.

The figure reveals that at a wind speed of 22.4 m/s and 0°, the external glazing experiences higher vibrations compared to the internal glazing. However, as the wind speed increases, the internal glazing exhibits higher vibration levels than the external glazing. Notably, the acceleration RMS values of the internal glazing are significantly higher than those of the external glazing in the wind load scenarios of 31.3 m/s and 40.2 m/s. Experimental measurements indicate a difference of 46.9 percent at 40.2 m/s, while the FE analysis predicts a difference of 29.7 percent. The findings suggest that the wind-induced vibration of the internal glazing unit is particularly sensitive to fluctuations in wind speed, compared to the external glazing. This emphasizes the need for effective mitigation strategies to address wind-induced vibrations on the internal glazing of the closed-cavity DSF, particularly at higher wind speeds.

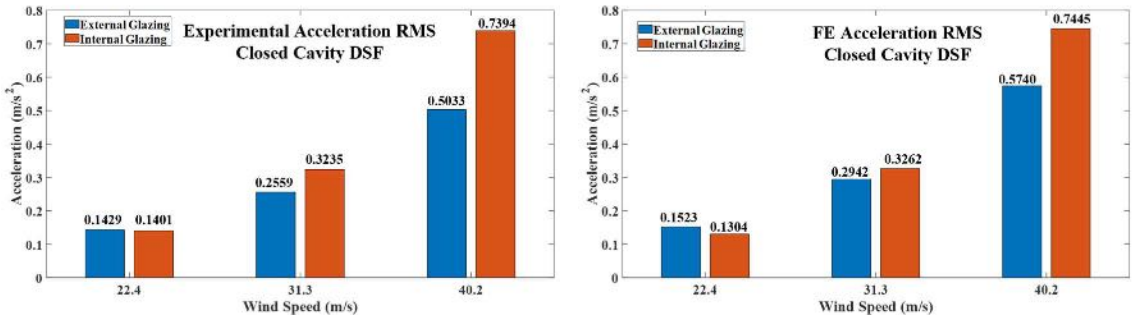

(a) (b)

Figure 4.19. Comparison of acceleration RMS of the external, and the internal glazing varying with wind speed, 0°: (a) Experimental results, and (b) FE results

Figure 4.20 demonstrates the influence of wind direction on glazing vibration for the external and internal walls of the DSF model. The results indicate that the external glazing exhibits higher acceleration RMS values than the internal glazing in windward and oblique directions. However, in the crosswind direction, the internal glazing experiences higher vibrations compared to the external glazing, with a difference of 46.0 percent according to experimental results. The FE analysis estimates a 14.5 percent higher acceleration RMS on the internal glazing compared to the external glazing for the crosswind direction.

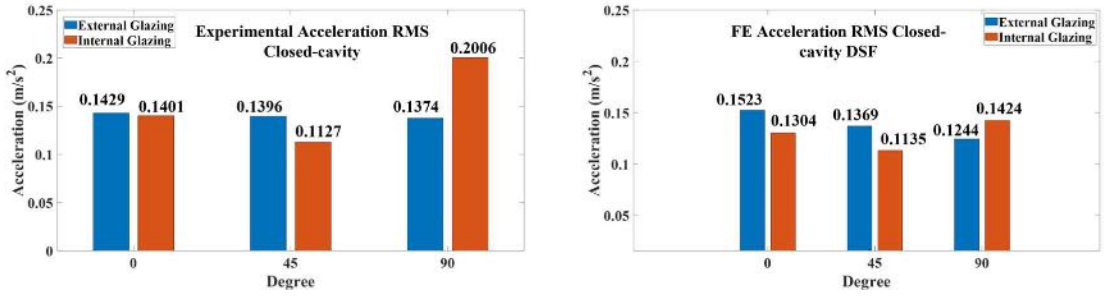

(a) (b)

Figure 4.20. Comparison of acceleration RMS of the external, and the internal glazing varying with wind direction, 22.4 m/s: (a) Experimental results, and (b) FE results

4.4.2. Closed-Cavity DSF with defects

In this section, the results of FE time history analysis are presented to validate the vented cavity DSF model, which includes defects compared to the ideal closed-cavity configuration. As mentioned earlier, the vented cavity DSF model features an opening on the side, leading to increased cavity permeability. This can simulate scenarios in which the ideal closed-cavity DSF experience higher cavity permeability due to defects. To model and validate the vented-cavity DSF models, the calibrated closed-cavity FE model is subjected to the corresponding measured internal pressure and cavity pressure time history of the vented-cavity by means of pressure taps 101, 102, 103, and 104, for the desired wind speed and wind direction. The external pressure profile is also applied to the external glazing, identical to the closed-cavity configuration. Table 4.11 provides a summary of the validation results for a wind speed of 22.4 m/s and wind direction of 0°. As shown in the table, the RMS of acceleration response from the validated FE model exhibits a difference of less than 12 percent compared to the experimental results.

Table 4.11. RMS of acceleration (m/s^2) time history of validated FE model of the vented-cavity DSF, compared to the experimental results for 22.4 m/s and 0° wind.

Accelerometer	Experimental acceleration time history RMS (m/s^2)	Finite element acceleration time history RMS (m/s^2)	Difference (%)
1	0.1349	0.1287	4.59
2	0.1324	0.1239	6.42
3	0.1463	0.1442	1.43
4	0.1448	0.1436	0.83
5	0.0468	0.0522	11.53

The validation results demonstrate that the acceleration responses are adequately captured, particularly for higher wind speeds. Table 4.12 presents validation results for a wind speed of 31.3 m/s and wind direction of 0°. As indicated in the table, the RMS of acceleration response from the validated FE model shows a difference of less than 11 percent compared to the experimental results.

Table 4.12. RMS of acceleration (m/s^2) time history of validated FE model of the vented-cavity DSF, compared to the experimental results for 31.3 m/s and 0° wind.

Accelerometer	Experimental acceleration time history RMS (m/s^2)	Finite element acceleration time history RMS (m/s^2)	Difference (%)
1	0.2633	0.2700	2.48
2	0.3080	0.2749	10.74
3	0.3697	0.3320	10.19
4	0.3806	0.3410	10.40
5	0.1222	0.1350	10.47

Figure 4.21 and Figure 4.22 depict the impact of higher cavity permeability on the vibration of external and internal glazing units, respectively. According to Figure 4.21, the RMS of acceleration for the closed-cavity DSF is 5.93 percent higher than that of the vented-cavity DSF. However, this trend reverses for higher wind speeds. As shown in the figure, the vented-cavity DSF exhibits a higher RMS of acceleration on the external glazing, compared to the closed-cavity DSF, with differences of 2.89 percent and 6.14 percent at wind speeds of 31.3 m/s and 40.2 m/s, respectively.

As shown in Figure 4.22, the vented-cavity DSF model exhibits higher vibrations on the internal glazing compared to the closed-cavity DSF model at all wind speeds considered. However, the effect of higher cavity permeability becomes more pronounced with

increasing wind speed. The RMS of acceleration for the internal glazing in the vented-cavity model shows a difference of 18.67 percent at a wind speed of 40.2 m/s compared to the closed-cavity model. This difference is measured as 4.42 percent and 14.28 percent at wind speeds of 22.4 m/s and 31.3 m/s, respectively.

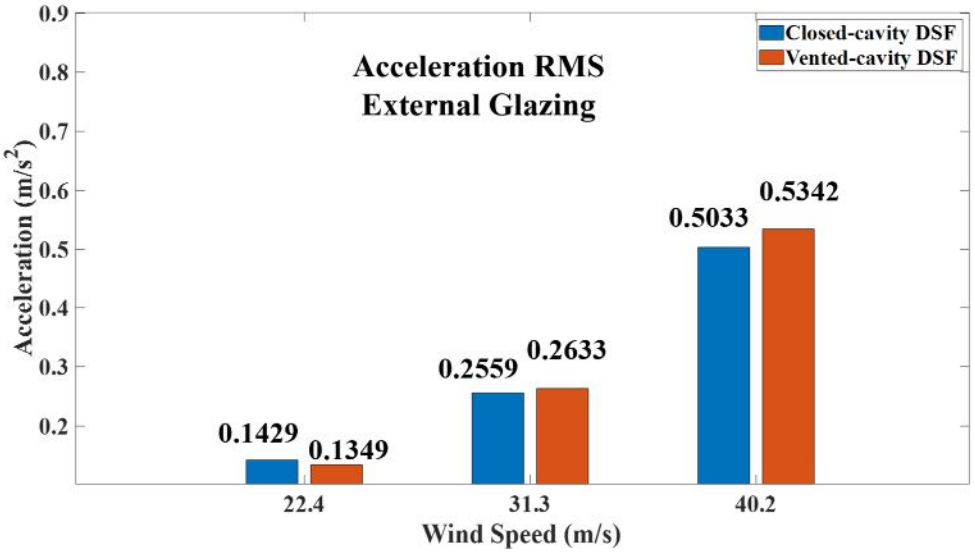

Figure 4.21. The effect of higher cavity permeability caused by defects on the acceleration response of the external glazing of the DSF, varying wind speed, 0° wind.

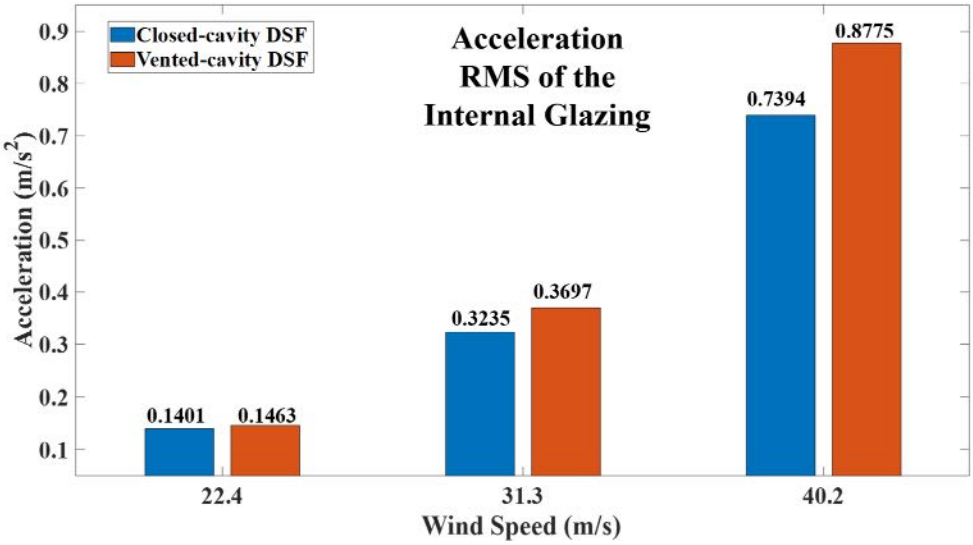

Figure 4.22. The effect of higher cavity permeability caused by defects on the acceleration response of the internal glazing of the DSF, varying wind speed, 0° wind.

The findings demonstrate that the presence of defects resulting in higher levels of cavity permeability in the DSF leads to increased vibration levels in both the external and internal glazing units. This increase is more pronounced in the vibration levels of the internal glazing compared to the external glazing. Moreover, this impact is further intensified at higher wind speeds, thereby increasing the risk of water infiltration in vented-cavity DSF systems compared to the ideal closed-cavity DSF.

4.5. Concluding Remarks

This study focuses on numerically investigating the wind-induced dynamic behavior of a closed-cavity double-skin curtainwall system. The analysis is based on the dynamic response data obtained from a series of full-scale wind tunnel tests conducted on a double-skin facade curtainwall installed on a host building structure. Wind speeds of 22.35 m/s, 31.30 m/s, and 40.23 m/s, with varying wind directions, are considered during the dynamic tests. Additionally, a vented-cavity double-skin facade (DSF) system is simulated by

incorporating a 10 mm hole on the sides of the DSF model to examine the effects of higher cavity permeability on the wind-induced response. To replicate the experimental setup, a comprehensive finite element (FE) model is developed that includes the supporting steel structure, curtainwall, and other building components. The FE models are subjected to nodal time history loads based on pressure time histories measured in the wind tunnel tests. Calibration of the numerical models is performed to accurately reproduce the acceleration responses of the actual curtainwall specimen under a wind speed of 22.35 m/s and wind direction of 0°. The calibrated FE model is then validated against other wind tunnel testing cases involving different wind speeds and wind directions, including the vented-cavity DSF model. The validation process demonstrates the sufficient accuracy of the calibrated FE model, making it a reliable predictive tool for further studies. Analysis of the power spectral densities of the acceleration response reveals that the wind-induced response of the DSF curtainwall is influenced by major frequencies at 3.7 Hz, 13.3 Hz, 16.4 Hz, 20.1 Hz, and 36.0 Hz. The results of the study show that vibration levels on the external and internal glazing of the closed-cavity DSF increase with higher wind speeds, thereby increasing the potential for water ingress during high wind speeds. Notably, the findings highlight the sensitivity of the wind-induced vibration of the internal glazing unit to fluctuations in wind speed compared to the external glazing. This emphasizes the importance of implementing effective mitigation strategies to address wind-induced vibrations on the internal glazing of the closed-cavity DSF, particularly at higher wind speeds. Furthermore, the results demonstrate the critical role of crosswind direction in the vibration levels of the internal glazing, which can significantly exceed those of the external glazing for a constant wind speed. Additionally, the findings highlight that the presence of

defects resulting in higher levels of cavity permeability in the DSF leads to increased vibration levels in both the external and internal glazing units. This increase is more pronounced in the vibration levels of the internal glazing compared to the external glazing. Moreover, this impact is further intensified at higher wind speeds, thereby increasing the risk of water infiltration in vented-cavity DSF systems compared to the ideal closed-cavity DSF.

CHAPTER 5 . CONCLUDING REMARKS

This study presents a novel comprehensive Finite-element-based investigation of the effects of wind-induced vibrations on the dynamic performance of building envelopes, considering façade-structure interaction. In this study, the wind-induced dynamic behavior of a single-skin, and a closed-cavity double-skin façade curtainwall model is investigated. Moreover, the dynamic performance of an operable window system, incorporated into the single-skin façade curtainwall is also studied. The FE modeling, calibration, validation, eigen, and time history analyses are based on experimental data obtained from a series of full-scale wind tunnel tests conducted for various wind speeds and wind directions, at the Natural Hazards Engineering Research Infrastructure (NHERI) Wall of Wind Experimental Facility (WOW EF) at Florida International University (FIU).

5.1. Summary of major findings

The summary of the most important results and findings of studying the wind-induced behavior of single-skin façade curtainwall are as follows:

- Two distinct FE modeling approaches are implemented. The first approach involves modeling the entire structure, encompassing the supporting structure, curtainwall, and other building components, while the second approach focuses on modeling the façade as an independent system. The analysis of power spectral densities of the acceleration response reveals a discrepancy between the stand-alone façade-only FE model and the whole structure FE model. Specifically, the stand-alone model fails to capture the first significant frequency at 4Hz, whereas the whole structure model accurately represents it.

- The application of a system identification method further confirms that the 4 Hz frequency is a result of the interaction between the façade and its supporting structure.
- The wind-induced response is likely overestimated by the façade-only FE model, as it does not consider the energy consumed for the deformation or excitation of the supporting structure. This finding highlights the importance of accurately modeling the interaction between the façade and the building structure to realistically capture the wind-induced dynamic behavior of façade systems. The performance of the façade can vary depending on the structure it is mounted to, emphasizing the need for comprehensive modeling that accounts for this interaction.
- The study also examines the dynamic effects of vertical protrusions on the wind-induced response of the façade. The findings suggest that the installation of protrusions can lead to an increase in the wind-induced dynamic response of the façade. This increase is attributed to the enhanced overall stiffness of the system, which may result in a higher probability of water ingress.
- Considering the dynamic response of the curtainwall, significant resonant frequencies are observed to be above 1 Hz. This finding suggests a need for reevaluation of the provisions in ASCE 7 regarding the analysis and design of components and claddings. Currently, these provisions do not consider wind-induced dynamic effects for structures with frequencies exceeding 1 Hz. Revisiting and updating these provisions would be beneficial to ensure accurate analysis and design of such structures.

The key findings and results obtained from the investigation of wind-induced behavior of an operable window system can be summarized as follows:

- The findings indicate that operable window systems and their connections can be vulnerable to failure caused by wind-induced resonant vibrations, particularly at frequencies exceeding 4 Hz. This emphasizes the need for analyzing the effects of vibration, which are currently not mandated by the ASCE 7 Standard.
- Furthermore, the dynamic behavior of the operable window system in the open position reveals that the metal hardware connections located at lower elevations exhibit elevated values of the dynamic amplification factor. This signifies that these connections are more susceptible to the effects of resonant vibrations across a range of wind speeds, from regular to hurricane-level intensities. Consequently, the bottom hardware connection emerges as the most vulnerable component in terms of potential failure. It is therefore imperative to prioritize careful consideration and attention during the design phase of the metal hardware, ensuring its ability to withstand potential failures under varying wind speeds and directions.

The following are the key findings and results derived from the analysis of wind-induced behavior of the closed-cavity double-skin façade curtainwall system:

- The examination of the power spectral densities of the acceleration response indicates that the wind-induced response of the DSF curtainwall is affected by significant frequencies at 3.7 Hz, 13.3 Hz, 16.4 Hz, 20.1 Hz, and 36.0 Hz.
- Vibration levels on both the external and internal glazing of the closed-cavity DSF increase as wind speeds rise, consequently raising the risk of water ingress in high wind conditions.
- Significantly, the findings highlight the internal glazing unit's heightened sensitivity to wind-induced vibrations in relation to variations in wind speed, as compared to the external glazing. This underscores the significance of implementing efficient mitigation strategies to address these vibrations, specifically for the internal glazing of the closed-cavity DSF, particularly at higher wind speeds.
- The crosswind direction is indicated to be critical for the vibration levels of the internal glazing, which can notably surpass those of the external glazing even when wind speed remains constant.
- The findings emphasize that the presence of defects causing higher levels of cavity permeability in the DSF results in elevated vibration levels in both the external and internal glazing units. This increase is particularly noticeable in the vibration levels of the internal glazing compared to the external glazing. Moreover, this impact becomes more severe at higher wind speeds, consequently amplifying the risk of

water infiltration in vented-cavity DSF systems compared to the ideal closed-cavity DSF.

5.2. Broader impacts and future directions

This study fills some of the existing gaps in the body of knowledge regarding the impact of wind-induced vibrations on the dynamic performance of major types and components of building envelope systems, including single-skin façade curtainwalls, double-skin façade curtainwalls, and operable window systems.

The results of this study, in conjunction with the advanced and comprehensive finite element (FE)-based models, methodologies, and analyses presented, will provide valuable insights for facade design, consulting, construction engineering, and insurance companies. These findings will deepen their understanding of the dynamic performance of curtainwall facade systems and operable windows in relation to wind-induced vibrations (WIV). This increased understanding has the potential to drive the development of innovative techniques, design methodologies, and mitigation strategies. Consequently, medium- and high-rise building facade systems can be enhanced to exhibit improved resilience and performance when subjected to extreme wind events.

The findings of this study have the potential to enhance the existing building codes and design guidelines, particularly in hurricane-prone regions of the United States, such as the State of Florida. The current building codes lack clear and robust guidelines for the design of facade components that may be susceptible to wind-induced vibrations (WIV). For example, ASCE 7-16 only establishes a general lower limit (1 Hz) for the first resonance of the system, aiming to identify critical scenarios. However, this criterion, originally

intended for the entire building, is often misinterpreted by designers, and applied to individual smaller components without considering the vibration mode or whether it can be excited by along-wind or across-wind/vortex shedding actions. Hence, it is crucial to update the building codes to promote a safe and sustainable design approach that considers all potential failures that may occur under serviceability conditions and ultimate dynamic excitations.

The validated finite element (FE)-based models and methodologies presented in this study have the potential to serve as a robust predictive tool for evaluating the susceptibility of curtainwall and operable window systems to structural failure under various wind loading scenarios in future investigations. This contribution holds significance within the realm of performance-based wind engineering concerning building envelopes. By incorporating nonlinear analysis into the current linear analysis, it becomes possible to explore the dynamic behavior of the building envelope and its constituent parts at failure limit states. This approach facilitates the evaluation of diverse failure modes in the curtainwall and operable window system caused by wind-induced vibrations, spanning from regular to hurricane-level wind speeds, through the utilization of risk modeling. Additionally, the consideration of other failure modes such as cumulative life-cycle fatigue becomes viable. The prospective computational framework enables the exploration of new design strategies by conducting systematic parametric studies on various components and elements of curtainwall and operable window systems. The adoption of risk-based design and mitigation strategies will enhance cost-effective methods aimed at bolstering resilience against the destructive impacts of wind-induced vibrations on building envelopes.

REFERENCES

Abdelaziz, K. M., Alipour, A., & Hobeck, J. D. (2021a). A smart façade system controller for optimized wind-induced vibration mitigation in tall buildings. *Journal of Wind Engineering and Industrial Aerodynamics*, *212*, 104601. https://doi.org/10.1016/j.jweia.2021.104601

Aiello, C., Caterino, N., Maddaloni, G., Bonati, A., Franco, A., & Occhiuzzi, A. (2018). Experimental and numerical investigation of cyclic response of a glass curtain wall for seismic performance assessment. *Construction and Building Materials*, *187*, 596–609.

Alawode, K. J., Vutukuru, K. S., Elawady, A., Lee, S. J., Chowdhury, A. G., & Lori, G. (2023). Wind-Induced Vibration and Wind-Driven Rain Performance of a Full-Scale Single-Skin Facade Unit with Vertical Protrusions. *Journal of Architectural Engineering*, *29*(2).

American Society of Civil Engineers (ASCE). (2016). *Minimum Design Loads for Building and Other Structures*.

ASTM E330 / E330M-14. (2014). *Standard Test Method for Structural Performance of Exterior Windows, Doors, Skylights and Curtain Walls by Uniform Static Air Pressure Difference*.

ASTM E1592. (2017). *Standard Test Method for Structural Performance of Sheet Metal Roof and Siding Systems by Uniform Static Air Pressure Difference*.

ASTM E1886-13a. (2013). *Standard Test Method for Performance of Exterior Windows, Curtain Walls, Doors, Impact Protective Systems Impacted by Missile(s) and Exposed to Cyclic Pressure Differentials*.

Azad, A. (2016). *Application of Smart Façade System in Reduction of Structural Response During Wind Loads*.

Azzi, Z., Habte, F., Vutukuru, K. S., Chowdhury, A. G., & Moravej, M. (2020). Effects of roof geometric details on aerodynamic performance of standing seam metal roofs. *Engineering Structures*, *225*.

Baskaran, B. A., & Brown, W. C. (1992). Performance of Pressure Equalized Rainscreen Walls under Cyclic Loading. *Journal of Thermal Insulation and Building Envelopes*, *16*(2), 183–193.

Bedon, C., & Amadio, C. (2018). Glass facades under seismic events and explosions: a novel distributed-TMD design concept for building protection. *Glass Structures and Engineering*, *3*, 257–274.

Bedon, C., Honfi, D., Machalická, K. V., Eliášová, M., Vokáč, M., Kozłowski, M., Wüest, T., Santos, F., & Portal, N. W. (2019). Structural characterisation of adaptive facades in Europe - Part II: Validity of conventional experimental testing methods and key issues. In *Journal of Building Engineering* (Vol. 25). Elsevier Ltd. https://doi.org/10.1016/j.jobe.2019.100797

Bedon, C., Zhang, X., Santos, F., Honfi, D., Kozłowski, M., Arrigoni, M., Figuli, L., & Lange, D. (2018). Performance of structural glass facades under extreme loads – Design methods, existing research, current issues and trends. In *Construction and Building Materials* (Vol. 163, pp. 921–937). Elsevier Ltd. https://doi.org/10.1016/j.conbuildmat.2017.12.153

Behr, R. A. (1998). Seismic Performance of Architectural Glass in Mid-Rise Curtain Wall. *ASCE Journal of Architectural Engineering*, *4*(3), 94–98. https://doi.org/10.1061/(ASCE)1076-0431(1998)4:3(94)

Bielek, B., Szabó, D., Palko, M., & Rychtáriková, M. (2017). Optimisation of Design of Air Inlets in Air Distribution Channels of a Double-Skin Transparent Façade. *Slovak Journal of Civil Engineering*, *25*(4), 1–11. https://doi.org/10.1515/sjce-2017-0017

Casagrande, L., Bonati, A., Auricchio, F., & Occhiuzzi, A. (2017). Dissipating effect of glazed curtain wall stick system installed on high-rise mega-braced frame-core buildings under nonlinear seismic excitation. *6th ECCOMAS Thematic Conference on Computational Methods in Structural Dynamics and Earthquake Engineering*, 3711–3727.

Caterino, N., Zoppo, M. del, Maddaloni, G., Bonati, A., Cavanna, G., & Occhiuzzi, A. (2017). Seismic assessment and finite element modelling of glazed curtain walls. *Structural Engineering and Mechanics*, *61*(1), 77–90. https://doi.org/10.12989/sem.2017.61.1.077

Chang, M., & Pakzad, S. N. (2014). Observer Kalman Filter Identification for Output-Only Systems Using Interactive Structural Modal Identification Toolsuite. *Journal of Bridge Engineering*, *19*(5).

Chowdhury, A. G., Vutukuru, K. S., & Moravej, M. (2018, December). Full- and Large-Scale Experimentation Using the Wall of Wind to Mitigate Wind Loading and Rain Impacts on Buildings and Infrastructure Systems. *Proceedings of the 11th Structural Engineering Convention (Sec18)*.

Chowdhury, A. G., Zisis, I., Irwin, P., Bitsuamlak, G., Pinelli, J., Hajra, B., & Moravej, M. (2017). Large-Scale Experimentation Using the 12-Fan Wall of Wind to Assess and Mitigate Hurricane Wind and Rain Impacts on Buildings and Infrastructure Systems. *Journal of Structural Engineering*, *143*(7).

Estephan, J., Chowdhury, A. G., & Irwin, P. (2022). A new experimental-numerical approach to estimate peak wind loads on roof-mounted photovoltaic systems by incorporating inflow turbulence and dynamic effects. *Engineering Structures*, *252*(1).

Eurocode prEN 16612. (2015). *Glass in building - Determination of the load resistance of glass panes by calculation and testing*.

FEMA. (2006). *Mitigation Assessment Team Report on Hurricane Katrina in the Gulf Coast: Building Performance Observations, Recommendations, and Technical Guidance [Full Report]*.

FEMA 339. (1999). *Building Performance Assessment Report: Hurricane Georges in Puerto Rico, Observations, Recommendations, and Technical Guidance*.

FEMA 488. (2005). *Hurricane Charley in Florida: Observations, Recommendations, and Technical Guidance*.

FEMA P-672. (2009). *Local Officials Guide for Coastal Construction*.

Galli, U. (2012). *Seismic behaviour of curtain wall facades: a comparison between experimental mock up test and finite element method analysis* [Master's Thesis]. Politecnico Milano.

Galuppi, L., & Royer-Carfagni, G. F. (2012). Effective thickness of laminated glass beams: New expression via a variational approach. *Engineering Structures*, *38*, 53–67.

Gan Chowdhury, A., Zisis, I., Irwin, P., Bitsuamlak, G., Pinelli, J.-P., Hajra, B., & Moravej, M. (2017). Large-Scale Experimentation Using the 12-Fan Wall of Wind to Assess and Mitigate Hurricane Wind and Rain Impacts on Buildings and Infrastructure Systems. *Journal of Structural Engineering*, *143*(7), 04017053. https://doi.org/10.1061/(asce)st.1943-541x.0001785

Gorenc, B., & Beg, D. (2016). Curtain wall façade system under lateral actions with regard to limit states. *Steel Construction*, *9*(1), 37–45.

Grayson, M., Pang, W., & Schiff, S. (2012). Three-dimensional probabilistic wind-borne debris trajectory model for building envelope impact risk assessment. *Journal of Wind Engineering and Industrial Aerodynamics*, *102*, 22–35. https://doi.org/10.1016/j.jweia.2012.01.002

Habte, F., Mooneghi, M. A., Chowdhury, A. G., & Irwin, P. (2015). Full-scale testing to evaluate the performance of standing seam metal roofs under simulated wind loading. *Engineering Structures*, *105*, 231–248.

Hashemi, N., Fayaz, R., & Sarshar, M. (2010). Thermal behaviour of a ventilated double skin facade in hot arid climate. *Energy and Buildings*, *42*(10), 1823–1832. https://doi.org/10.1016/j.enbuild.2010.05.019

Horst, M., Howard, D. K., & Leistikow, R. (2012). Separating Junk Science from Sound Engineering Principles during Forensic Assessments of Hurricane Damage. *Advances in Hurricane Engineering*, 165–176. https://doi.org/10.1061/9780784412626.016

Høseggen, R., Wachenfeldt, B. J., & Hanssen, S. O. (2008). Building simulation as an assisting tool in decision making. Case study: With or without a double-skin façade? *Energy and Buildings*, *40*(5), 821–827. https://doi.org/10.1016/j.enbuild.2007.05.015

Ilter, E., Tavil, A., & Celik, O. C. (2015). Full-scale performance testing and evaluation of unitized curtain walls. *Journal of Facade Design and Engineering*, *3*(1), 39–47. https://doi.org/10.3233/FDE-150028

Irwin, P., Cooper, K. R., & Girard, R. (1979). Correction of distortion effects caused by tubing systems in measurements of fluctuating pressures. *Journal of Wind Engineering and Industrial Aerodynamics*, *5*(1–2), 93–107.

Jafari, M., & Alipour, A. (2021). Aerodynamic shape optimization of rectangular and elliptical double-skin façades to mitigate wind-induced effects on tall buildings. *Journal of Wind Engineering and Industrial Aerodynamics*, *213*. https://doi.org/10.1016/j.jweia.2021.104586

Jain, A. (2015). Hurricane Wind-Generated Debris Impact Damage to the Glazing of a High-Rise Building. *Forensic Engineering 2015*, 361–370. https://doi.org/10.1061/9780784479711.035

Kala, S., Stathopoulos, T., & Suresh Kumar, K. (2008). Wind loads on rainscreen walls: Boundary-layer wind tunnel experiments. *Journal of Wind Engineering and Industrial Aerodynamics*, *96*(6–7), 1058–1073. https://doi.org/10.1016/j.jweia.2007.06.028

Killip, I. R., & Cheetham, D. W. (1984). The prevention of rain penetration through external walls and joints by means of pressure equalization. *Building and Environment*, *19*(2), 81–91. https://doi.org/10.1016/0360-1323(84)90033-7

Lu, W., Wang, Y., Chen, H., Jiang, L., Duan, Q., Li, M., Wang, Q., & Sun, J. (2018). Investigation of the thermal response and breakage mechanism of point-supported glass facade under wind load. *Construction and Building Materials*, *186*, 635–643. https://doi.org/10.1016/j.conbuildmat.2018.07.114

Marques da Silva, F., & Glória Gomes, M. (2008). Gap inner pressures in multi-storey double skin facades. *Energy and Buildings*, *40*(8), 1553–1559. https://doi.org/10.1016/j.enbuild.2008.02.014

Mazzucchelli, E. S., Luccini, A., Stefanazzi, A., & Tattoni, S. (2017). Analysis and control of façade claddings structural issues. *TEMA: Technologies, Engineering, Materials, Architecture*, *3*(1).

Memari, A. M., Simmons, N., & Solnosky, R. L. (2021). Developing FEM Procedures for Four-Sided Structural Sealant Glazing Curtain Wall Systems with Reentrant Corners. *Buildings*, *11*(12).

Michael Grayson, J., Pang, W., & Schiff, S. (2013). Building envelope failure assessment framework for residential communities subjected to hurricanes. *Engineering Structures*, *51*, 245–258. https://doi.org/10.1016/j.engstruct.2013.01.027

MIDAS Information Technology Co., Ltd. (2020). *Midas Gen Manuals and Tutorials*.

MIDAS Information Technology Co., Ltd. (2021). *Midas Gen Software*.

Minor, J. E. (1994). Windborne debris and the building envelope. *Journal of Wind Engineering and Industrial Aerodynamics*, *53*(1–2), 207–227. https://doi.org/10.1016/0167-6105(94)90027-2

Momtaz, A. A., Abdollahian, M. A., & Farshidianfar, A. (2017). Study of wind-induced vibrations in tall buildings with tuned mass dampers taking into account vortices effects. *International Journal of Advanced Structural Engineering*, *9*(4), 385–395. https://doi.org/10.1007/s40091-017-0174-9

Moravej, M., Chowdhury, A., Irwin, P., Zisis, I., & Bitsuamlak, G. (2015, June). Dynamic Effects of Wind Loading on Photovoltaic Systems. *14th International Conference on Wind Engineering*.

Mosqueda, G., Porter, K. A., O'Connor, J., & McAnany, P. (2007). Damage to Engineered Buildings and Bridges in the Wake of Hurricane Katrina. *Forensic Engineering (2007)*, 1–11. https://doi.org/10.1061/40943(250)4

Nakagami, Y. (2003). *Probabilistic Dynamics of Wind Excitation on Glass Facade* [Doctoral Dissertation]. Technical University of Darmstadt.

Naqash, M. T., Formisano, A., & Noroozinejad Farsangi, E. (2021). Structural assessment of glass used in façade industry. *Structures*, *33*, 4817–4827. https://doi.org/10.1016/j.istruc.2021.07.059

National Science Board. (2007). *HURRICANE WARNING: The Critical Need for a National Hurricane Research Initiative*.

NCEI. (2022). *U.S. Billion-Dollar Weather and Climate Disasters (2022)*.

NOAA. (2021). *Office of Coastal Management, National Oceanic and Atmospheric Administration, Hurricane Costs. https://coast.noaa.gov/states/fast-facts/hurricane-costs.html*.

Oh, S. H. (2020). Curtain wall facades on the new generation of supertall buildings present and future directions. *International Journal of High-Rise Buildings*, *9*(2), 113–155. https://doi.org/10.21022/IJHRB.2020.9.2.113

Pan, F., Cai, C. S., & Zhang, W. (2013). Wind-Induced Internal Pressures of Buildings with Multiple Openings. *Journal of Engineering Mechanics*, *139*(3), 376–385. https://doi.org/10.1061/(ASCE)EM.1943-7889.0000464

Pariafsai, F. (2016). A review of design considerations in glass buildings. *Frontiers of Architectural Research*, *5*(2), 171–193. https://doi.org/10.1016/j.foar.2016.01.006

Pomaranzi, G., Daniotti, N., Schito, P., Rosa, L., & Zasso, A. (2020). Experimental assessment of the effects of a porous double skin façade system on cladding loads. *Journal of Wind Engineering and Industrial Aerodynamics*, *196*. https://doi.org/10.1016/j.jweia.2019.104019

Pracucci, A., Magnani, S., & Casadei, O. (2020). The integration of vacuum insulated glass in unitized façade for the development of innovative lightweight and highly insulating energy efficient building envelope—the results of eensulate façade system design. *Designs*, *4*(4), 1–15. https://doi.org/10.3390/designs4040040

Qin, H., Mason, M., & Stewart, M. G. (2023). Fragility assessment for new and deteriorated portal framed industrial buildings subjected to tropical cyclone winds. *Structural Safety*, *100*, 102287. https://doi.org/10.1016/j.strusafe.2022.102287

Qu, J., Song, J., Qin, J., Song, Z., Zhang, W., Shi, Y., Zhang, T., Zhang, H., Zhang, R., He, Z., & Xue, X. (2014). Transparent thermal insulation coatings for energy efficient glass windows and curtain walls. *Energy and Buildings*, *77*, 1–10. https://doi.org/10.1016/j.enbuild.2014.03.032

Rizzo, F., Franco, A., Bonati, A., Maddaloni, G., Caterino, N., & Occhiuzzi, A. (2021). Predictive analyses for aerodynamic investigation of curtain walls. *Structures*, *29*, 1059–1077.

Sanders, R. M., & Hargrove, C. A. (2012). Preventing and Treating Failure in Glazed Curtain Wall Systems. *Journal of Architectural Engineering*, *29*(2).

Saroglou, T., Theodosiou, T., Givoni, B., & Meir, I. A. (2020). Studies on the optimum double-skin curtain wall design for high-rise buildings in the Mediterranean climate. *Energy and Buildings*, *208*. https://doi.org/10.1016/j.enbuild.2019.109641

Suaris, W., & Khan, M. S. (1995). Residential Construction Failures Caused by Hurricane Andrew. *Journal of Performance of Constructed Facilities*, *9*(1), 24–33. https://doi.org/10.1061/(ASCE)0887-3828(1995)9:1(24)

van den Bossche, N., van den Brande, K., de Bleecker, H., & Lori, G. (2020). Validation of a coupled pressure-equalization-thermal-mechanical model to study double-skin

facades. *E3S Web of Conferences*, *172*. https://doi.org/10.1051/e3sconf/202017224001

Vutukuru, K. S. (2021). *Full-scale Experiment Modeling to Study Wind-induced Vibrations, Wind-driven Rain and Their Effects on Curtainwall Window Systems*. FIU Electronic Theses and Dissertations.

Vutukuru, K. S., Alawode, K. J., Bakhtiari, A., Elawady, A., Lee, S. J., Chowdhury, A. G., & Lori, G. (2021, June). Full-scale experimental testing to investigate wind-induced vibrations on curtain wall systems. *Proceedings of International Structural Engineering and Construction*.

Wu, M. H., Ng, T. S., & Skitmore, M. R. (2016). Sustainable building envelope design by considering energy cost and occupant satisfaction. *Energy for Sustainable Development*, *31*, 118–129. https://doi.org/10.1016/j.esd.2015.12.003

Yalaz, E. T., Tavil, A. U., & Celik, O. C. (2018). Lifetime performance evaluation of stick and panel curtain wall systems by full-scale testing. *Construction and Building Materials*, *170*, 254–271. https://doi.org/10.1016/J.CONBUILDMAT.2018.03.061

VITA

ALI BAKHTIARI

2007-2012	B.S., Civil Engineering Sharif University of Technology Tehran, Iran
2013-2016	M.S., Civil Engineering/Structures Sharif University of Technology Tehran, Iran
2018-2022	M.S., Civil Engineering Florida International University Miami, Florida
2018 -2023	Doctoral Candidate Florida International University Miami, Florida
	Research Assistant Florida International University Miami, Florida
	Teaching Assistant Florida International University Miami, Florida
2022	UGS Doctoral Evidence Acquisition Fellow Florida International University Miami, Florida
2022 -2023	UGS Dissertation Year Fellow Florida International University Miami, Florida

PUBLICATIONS AND PRESENTATIONS

Bakhtiari, A., & Lee, S. J. (2019). Predictive Computer Program for Proactive Demolition Planning (No. ABC-UTC-2013-C3-FIU02). Accelerated Bridge Construction University Transportation Center (ABC-UTC).

Vutukuru, K. S., Alawode, K., Bakhtiari, A., ELAWADY, A., Lee, S. J., CHOWHDURY, A. G., & LORI, G. (2021). Full-Scale Experimental Testing to Investigate Wind-Induced Vibrations on Curtain Wall Systems. Proceedings of International Structural Engineering and Construction, 8, 1.

Alawode, K. J., Vutukuru, K. S., Bakhtiari, A., Elawady, A., Lee, S. J., Chowdhury, A. G., & Lori, G. (2022) High-Wind Performance of a Full-Scale Single Skin Curtain wall Unit with Vertical Protrusions. *14 thAmericas Conference on Wind Engineering*

Bakhtiari, A., & Lee, S. J. (2019). Enhanced Demolition Planning via Computer Simulation. *International Accelerated Bridge Construction Conference*

Bakhtiari, A., Alawode, K. J., Vutukuru, K. S., Lee, S. J., Elawady, A., Chowdhury, A. G., & Lori, G. (2022) A Numerical Study on the Wind-induced Dynamic Response of a Single-skin Curtainwall System. *14 thAmericas Conference on Wind Engineering*